

Spin Current Amplification by a Geometrical Ratchet Effect

Ranjdar M. Abdullah

Doctor of Philosophy

University of York

Electronics

April 2015

Abstract

A lateral spin-valve (LSV) is a structure to achieve non-local spin accumulation in future spintronic devices. Although numerous studies have been performed and have demonstrated highly efficient and reliable non-local accumulation, the use of a LSV is still hampered by the small magnitude of spin-current signals. Therefore, this study focused on the amplification of the pure spin-current signals by controlling the geometry of the non-magnetic nanowire in the LSV for the first time.

A two-dimensional model was developed based on a diffusion equation and was used for a series of Cu nanowires with different shapes implemented at their centre to identify their geometrical ratchet effect (GRE) upon the spin-polarised electron transport. Asymmetric shapes, such as obtuse- and right-angle triangles, were found to induce the GRE, leading to the spin-current amplification in both time-dependent and steady states. The geometries have then been optimised for the maximum amplification.

Before the experimental validation of the GRE, Py and Cu bars and conventional Py/Cu/Py LSVs were fabricated and characterised to optimise the fabrication and transport-measurement processes. The spin-current amplification was then investigated in LSVs with right-angle triangles maintaining the same base (100 nm) but varying their height ($0 \leq h \leq 60$ nm). The non-local signals were measured by a direct current (DC)-reversal technique. The spin-current signals were measured to be significantly amplified by a factor of more than 7 for $h = 60$ nm as compared with the conventional LSV ($h = 0$ nm). These results were compared with the steady-state calculations using measured device dimensions, showing a good qualitative agreement. The measurements were also carried out with a DC setup, which revealed the junction spin polarisation ($\sim 1\%$ in this study) allowed both up- and down-spin currents with similar amplitudes to flow. Further improvement in the junction spin polarisation should increase the GRE, leading to future device implementation.

Contents

Abstract	ii
List of Tables	vi
List of Figures	ix
Acknowledgements	xi
Declaration	xii
1 Introduction	1
2 Theoretical Background	6
2.1 Fundamentals of spintronics	6
2.2 Giant magnetoresistance (GMR) effect	10
2.3 Spin injection, accumulation and detection	13
2.4 Lateral spin-valves	17
2.5 Spin relaxation mechanisms in metals	20
2.5.1 Dyakonov-Perel mechanism	20
2.5.2 Elliot-Yafet scattering	21
2.5.3 Magnetic impurity scattering	22
2.6 Spintronic devices	23
2.6.1 Spin-valve read heads	23
2.6.2 Magnetic random access memory (MRAM)	25
2.6.3 Spin-polarised field effect transistor (Spin FET)	27
3 Computational Modelling of Modulated Lateral Spin-Valves	29
3.1 Introduction	29
3.2 FreeFem++	30
3.3 Model development	33

3.4	Assumptions and limitations of the model	35
3.5	Validation of the model	36
3.6	Results and discussion	39
3.6.1	Symmetrical shapes	39
3.6.2	Asymmetrical shapes	42
3.7	Steady-state diffusion equation	48
4	Device Fabrication	53
4.1	Introduction	53
4.2	Device designs	54
4.3	Fabrication processes	57
4.3.1	LSV devices	58
4.3.1.1	Spin coating of resist	58
4.3.1.2	EBL exposure (first layer)	61
4.3.1.3	Resist development	62
4.3.1.4	Metallisation	62
4.3.1.5	Lift-off	62
4.3.1.6	Second layer patterning	63
4.3.2	External electrical contacts	64
4.3.2.1	Photolithography	64
4.3.2.2	Metallisation	65
4.4	Wire bonding	66
5	Characterisation Techniques	69
5.1	Transport measurement setup	69
5.2	Noise and errors in electrical measurements	70
5.2.1	Thermal noise (Johnson noise)	72
5.2.2	Flicker noise	73
5.2.3	Shot noise	74
5.2.4	Thermoelectric voltage	75
5.2.5	Lead resistance errors	76
5.3	DC reversal measurement technique	77

5.4	Scanning electron microscope	82
6	Optimisation of the Fabrication and Measurement Processes	85
6.1	Ladder devices	85
6.2	Cu/Cu LSV devices	90
6.3	Py/Cu LSV devices with a straight NM wire	91
6.3.1	Local resistance test	92
6.3.2	Non-local spin transport measurements	95
6.3.2.1	Non-local spin-valve signals	96
6.3.2.2	Spin diffusion length	99
7	Non-local Spin-Current Amplification	102
7.1	Samples and dimensions	103
7.2	Measurement geometries	105
7.3	Spin-current amplification measurements	106
7.4	Comparison between measured and calculated values	110
7.5	Spin-current amplification in a conventional DC measurement	111
8	Summary, Conclusions and Future Work	114
8.1	Summary and conclusions	114
8.2	Future work	117
	Appendix	118
A	FreeFem++ simulation code	119
B	LabVIEW code for the “DC reversal” technique	122
	List of Symbols	126
	List of Abbreviations	129
	References	143

List of Tables

2.1	Spin polarisation values of various ferromagnets.	9
3.1	Parameters used in the calculations.	37
4.1	Dimensions of the devices fabricated.	56
4.2	Comparison of wire bonding methods.	67
4.3	Optimised wire bonding parameters.	68
6.1	Comparison of spin diffusion lengths and injected spin efficiency	100
7.1	Average values of l , w_{Py} , w_{Cu} and A_J for all the measured samples.	105

List of Figures

2.1	Schematic diagram of two-channel model.	7
2.2	Schematic diagrams of spin-resolved DOS.	8
2.3	Schematic showing of tunnelling magnetoresistance.	10
2.4	Schematic showing of CIP and CPP giant magnetoresistance.	11
2.5	Schematic diagrams of electron flow in a trilayer configurations.	12
2.6	Schematic setup of a FM/NM interface for spin injection.	14
2.7	Electrochemical potentials in FM/NM interface.	16
2.8	Electrochemical potentials in a FM1/NM/FM2 structure.	17
2.9	Lateral structure and its electrochemical potentials.	18
2.10	Schematic illustration of the non-local measurement in a LSV.	19
2.11	Schematic view of the Dyakonov-Perel spin relaxation mechanism.	21
2.12	Schematic view of the Elliot-Yafet spin relaxation mechanism.	22
2.13	Schematic views of the spin-valve structure and the data storage.	25
2.14	Schematic structure of MRAM.	26
2.15	Schematic diagrams of STT-based magnetisation switching.	27
2.16	Schematic diagrams of Datta-Das spin FET.	28
3.1	Typical simulation flow in the 2D FreeFem++ simulator.	32
3.2	Schematic diagrams of the 2D geometries used for the simulations.	34
3.3	A 2D straight NM nanowire with its mesh types and calculations.	38
3.4	Snapshots of the electron distributions for the electrons flowing	40
3.5	Time dependences of voltages calculated for the symmetric shapes.	41
3.6	Snapshots of the electron distributions for the right-angle wire.	43
3.7	Comparison of the potential differences for the obtuse-angle wire.	44
3.8	Comparison of the potential differences for the right-angle wire.	45

3.9	Corresponding peak values of the potential differences.	46
3.10	Peak values of the potential differences with different b and h . . .	47
3.11	The potential differences for $n = 2$ for the obtuse-angle wire. . . .	49
3.12	The potential differences for $n = 2$ for the right-angle wire.	50
3.13	Steady-states calculations for the right-angle wire.	52
4.1	Schematic diagrams of a ladder and a conventional LSV devices .	55
4.2	Schematic diagram of the LSV with the triangles.	56
4.3	Device layout on the 16 mm square substrate containing 9 chips. .	57
4.4	Schematic diagrams of the EBL patterning processes.	59
4.5	Schematic diagrams of the EBL exposure onto two types of resist	60
4.6	Photograph of the JEOL JBX-6300FS EBL system	61
4.7	SEM image of the LSV with the triangles after the second EBL . .	64
4.8	Schematic mask design drawn by L-Edit.	65
4.9	Optical microscope image of completed electrical contacts.	66
4.10	Photograph of a mounted sample after wire bonding.	67
5.1	Photograph and block diagram of the measurement setup	71
5.2	Illustration of thermoelectric voltages induced in a circuit	76
5.3	Schematic diagram of the two-terminal resistance measurement .	77
5.4	Schematic diagram of a four-terminal resistance measurement . .	78
5.5	Instrumentation setup for the “DC reversal” technique.	79
5.6	Test signal for the “DC reversal” measurements.	80
5.7	Front panel of the “DC reversal” LabView programme.	81
5.8	Photograph and schematic diagram of the SEM.	82
5.9	Schematic diagram of electron-sample interactions	83
5.10	SEM sample holder with a spring clip.	84
6.1	SEM images illustrating the ladder devices	86
6.2	Schematic diagram of the measurement configuration.	88
6.3	Voltage responses against applied currents for the Cu and Py bars	89
6.4	SEM image of a typical Cu/Cu LSV device	91
6.5	SEM images of the Py/Cu LSV device and its magnified junctions	93

6.6	Schematic diagrams of four-terminal configurations	94
6.7	Typical local resistances measured for a LSV with the dimension .	95
6.8	Diagram of the NLSV measurement and an SEM image of a LSV.	97
6.9	NLSV signals measured for the three devices	98
6.10	$\Delta V/I$ signals dependent on l	101
7.1	SEM image of a LSV with a pair of triangular ratchets.	104
7.2	“LtoR” and “RtoL” non-local probe configurations.	106
7.3	Non-local signals for the LSVs with $h = 0, 20, 37$ and 60 nm. . . .	107
7.4	Non-local signals obtained with the “RtoL” configuration.	108
7.5	Triangular height dependence of the non-local signals.	110
7.6	SEM image of the measured LSV with ratchets.	112
7.7	NLSV signals measured using the “DC reversal” technique.	113
7.8	NLSV signals measured using the DC setup.	113

Acknowledgements

In the course of researching, preparing for and writing up this thesis a number of people have helped me and as I bring the work to its conclusion I would very much like to extend them my gratitude for all their help and support.

To start with, for allowing me to be part of his work group, his untiring discussions on the topic, his careful mentoring and constant advice and support, I would like to offer my fullest appreciation to my supervisor, Professor Atsumi Hirohata. I was honoured to be working with him and can truly say that without his encouragement and help, I would have been unable to complete this work.

For allowing me to use his facilities to undertake most of my measurements, as well as for his helpful discussions, advice and support, I would also like to extend my gratitude to Professor Kevin O'Grady. Thank you also to Professor Mohamed El-Gomati for offering helpful suggestions and support, and to Professor Sara Thompson, the University of York Head of Physics, for letting me use one of her laboratories for my work on non-local spin values.

Particular thanks to the group I worked with, who was constantly supportive as well as great fun to work with; there are too many of you to name but I would like to thank Dr Andrew and Mr Benedict for supporting and their co-authoring in my work.

My thanks to the KRG-HCDP Scholarship Program/Ministry of Higher Education and Scientific Research/Kurdistan Regional Government which provided sponsorship for this work, and thanks to the Electronics Department at the University of York which provided funding for me to go to workshops and conferences. I would also like to thank the University of York for supporting me with a hardship fund during my year of writing up.

I am particularly grateful to the University of York Department of Electronics staff as well as those in the York-JEOL Nanaocentre. These people provided help and support in the course of my work; special thanks to Mr. Paul Breslin, Mr. Ian Wright, Mr. Owen Francis, Mr. Johathan Cremer, Mr. Steve Murphy, Mrs. Camilla Danese and Miss. Helen Fagan.

Thank you also to my friends, for your encouragement and friendship and for making the period of my PhD a particularly happy one; in particular thanks to Dr. Sherif Bakush, Dr. Hamid Al-Garni, Mr. Tariq Alhuwaymel, Mr. Peshwaz Abdul, Mr. Hayman Abdoul, Mr. Bestoon Hussien and Mr. Dana Sabir.

Finally I must thank my family, my parents, sisters and brothers-in-law for their love, faith and support.

I am hugely grateful for all of your kindness.

Declaration

I declare that the work presented in this thesis is based purely on my own research, unless otherwise stated. References and acknowledgments to other researchers have been given as appropriate. This work has not been submitted for a degree in either this or any other university. Some of the research presented in this thesis has resulted in the following publications:

- R. M. Abdullah, A. J. Vick, B. A. Murphy, and A. Hirohata, “Spin-current signal amplification by a geometrical ratchet”, *Journal of Physics D: Applied Physics* **47**(48), 482001 (2014).
- R. M. Abdullah, A. J. Vick, B. A. Murphy, and A. Hirohata, “Optimisation of geometrical ratchets for spin-current amplification”, *Journal of Applied Physics* **117**, 17C737 (2015).

Chapter 1

Introduction

Today, the human society deals increasing amount of information and hence depends on information communication technology (ICT). Such increase has been maintained by the advancement of semiconductor and integrated circuit (IC) technologies. Due to such advancement in recent years, more computing power has been required to manage further increase of information available in the society in various forms. Conventionally an electric charge of an electron has been used to store and carry data in the ICT infrastructures, which have been relied on Moore's law [1]. This law was proposed in 1965 by predicting the number of transistors per IC chip (and the associated processing power of the chip) to increase by $\sim 200\%$ every two years.

However, the succession of Moore's law has recently been found to be hindered by the fundamental laws of physics due to the miniaturisation of the semiconductor devices. According to quantum mechanics, further reduction in the insulator thickness (< 2 nm) for a gate in a metal oxide semiconductor field effect transistor (MOSFET) is expected to induce a tunneling current. The quantum mechanics also predicts that the electrical current cannot be confined in a narrower path (< 10 nm). The current paths generate Joule heating, which increase the power consumption of the devices and causes thermal noise in the devices. The current operation frequency of a MOSFET (\sim GHz) generates elec-

tromagnetic wave with wavelength of $\sim 0.1 \mu\text{m}$, which is difficult to be shielded and induces cross-talks between the devices.

One of the potential candidates to overcome these problems is spintronics [2–4]. Unlike common electronic devices, spintronic devices utilise electron spins, allowing one electron to carry one data bit ideally. Such a spin-polarised current can therefore reduce the power consumption. Such a spin-polarised current has already been used to demonstrate magnetoresistive effects (see Sections 2.1 and 2.2 for details) implemented in magnetic memories. However, the spin-polarised current consists of both charge and spin flow and hence suffers from the physical limitation as discussed above. On the other hand, a pure spin current, which has no net charge current can avoid these obstacles related to the device miniaturisation, especially the Joule heating.

A number of different methods to generate a pure spin current have been proposed and investigated, from both theoretical and experimental perspectives. One method is to utilise large spin-orbit interactions to scatter electron spins to separate up- and down-spins in a material (*e.g.*, Pt), which is known as spin Hall effect (SHE) [5–10]. The other method is to induce a spin-polarised electron by external oscillating fields, which is known as spin pumping method [11–13]. Recently, temperature gradient has been demonstrated to produce a pure spin current through the spin Seebeck effect (SSE) [14, 15].

A pure spin current can also be generated in a lateral spin-valve (LSV) structure by employing non-local geometry (see Section 2.4) [16, 17]. This geometry uses local spin imbalance at the Fermi level in a non-magnet (NM) to induce a pair of up- and down-spin electron flow in the opposite directions. The electrical spin injection in metallic LSVs has initially been demonstrated by Johnson and Silsbee [18] for permalloy (Py) ferromagnetic electrodes deposited on a bulk Aluminium. Further detailed studies have been carried out by Jedema *et al.* [16] in the nanoscale LSVs patterned by electron beam lithography [9, 19–22].

However the main disadvantage of the utilisation of the pure spin currents is their generation efficiency in a NM material. For the non-local geometry method, the generated pure spin current is typically three orders of magnitude lower than the electrically injected spin-polarised electrical current with both charge and spin currents [16]. The pure spin currents in these structures are still less than adequate amplitude to be employed in applications [23,24], rendering spin-current amplification crucial.

The aim of this study is therefore to amplify the pure spin current. I have especially focused on the amplification of the pure spin-current signals by implementing new geometrical ratchets for the first time. The conventional NM straight nanowire in the LSV was replaced by one with pair(s) of additional triangular or square wings with symmetric and asymmetric shapes. For the asymmetric geometries, geometrical ratchet effect (GRE) upon the pure spin current was found to achieve spin-current amplification. The details of this study are described as below:

In chapter 2, theoretical background on spin-polarised electron transport is reviewed. Namely, three key theories are described: (i) Mott's two-current model to explain magnetoresistance effects, (ii) the mechanism of spin injection, accumulation and detection in the LSV structure and (iii) spin relaxation in a non-magnetic metal. This chapter is concluded with associated spintronic device applications, including read heads for hard disk drives, magnetic random access memory and spin-polarised field effect transistor.

Chapter 3 presents a computational model developed for the optimisation of the GRE upon the amplification of a pure spin current in a LSV device. The model is based on a two-dimensional time-dependent spin diffusion equation. A finite element method is used to solve the equation in a non-magnetic Cu nanowire with a series of geometries. The calculated results are discussed with respect to their shapes and their number of pairs phenomenologically. Finally, a steady-state spin-diffusion process is calculated and compared with the time-

dependent cases, revealing the fact that the spin-current amplification is present even at a steady state. An example of the simulation code using FreeFem++ software is presented in Appendix A.

Chapter 4 describes the facilities and techniques used to fabricate the LSV devices studied in this thesis. A flow chart of the nanofabrication steps is provided, including wafer cleaning, spin coating, lithography, development, metallisation, lift-off and wire bonding. The designs of the devices are also shown.

Chapter 5 explains the measurement and techniques used for the transport studies and device characterisation in this work. Typical sources of noise for non-local voltage measurements are discussed. To reduce the noise, simple techniques, such as averaging, filtering and shielding, are discussed depending on the types of the noise. In this study, a relatively new measurement method, which is known as a “*direct current (DC) reversal*” technique, is employed to reduce the noise. An associated LabView programme for this technique has been developed with the standard commands for programmable instruments (SCPI) programming language as shown in Appendix B. The principle operation of a scanning electron microscope, which is used to assess the device dimensions, is also given at the end of this chapter.

Chapter 6 deals the optimisation of the fabrication and measurement processes. Transport measurements are performed on Py and Cu bars and conventional Py/Cu/Py LSV devices. Critical parameters, such as electrical resistivity, spin diffusion length and spin injection/detection efficiency, are measured at room temperature. The obtained parameters are compared with the literature values and are feedback to optimise the these processes.

Chapter 7 provides the first experimental results on the non-local spin-current amplification in a LSV with right-angle triangles. The GRE is studied by measuring the non-local resistance using the “*DC reversal*” technique with varying the height of the triangles and maintaining their base. Clear switching

in the resistance is observed for all the LSV devices depending on the magnetisation directions of the two Py wires as expected. The LSV device are also measured using a DC setup. The difference in the resistance between parallel and antiparallel magnetisation directions is found to increase with increasing the height of the triangles up to 60 nm. These results are compared with additional calculations using measured device dimensions. These results agree with each other quantitatively by considering the spin injection/detection efficiency and the resulting junction spin polarisation.

Chapter 8 concludes this study with the summary of the computational and experimental results. Several future directions are also proposed at the end.

Chapter 2

Theoretical Background

Spintronics is an emerging research field that investigates broad physical phenomena ranging from static to dynamic behaviours. In this chapter, the basic understanding of spin transport in a lateral spin-valve structure is predominantly described. First the fundamentals of spintronics discussing general electronic transport in metals are introduced depending on the spin degrees of freedom. Quantum mechanical magnetoresistance effects are then reviewed. The theory of electrical injection, accumulation and detection in a trilayered structure is discussed afterwards. This theory is further extended to the lateral spin-valve structure using electrochemical potentials to describe the generation of pure spin currents. Major spin relaxation mechanisms in a non-magnetic metal are then overviewed. This chapter is concluded with a summary of spintronic devices using these spin transport mechanisms.

2.1 Fundamentals of spintronics

It was from the beginning of the twentieth century that people started acknowledging the physics underlying the rapid development in electronics based on spin-related phenomena. It was noted by Stern and Gerlach in 1922 that an in-

homogeneous magnetic field caused deflection of a single beam of Silver atoms into two [25]. This indicated that the electrons possess an inherent angular momentum, which was similar to charge spinning. This intrinsic feature was subsequently called “spin” of an electron. It was possible to quantise the spin into two distinct states by their z -component of the spin-angular momentum. These states were known as “up-spin” and “down-spin”, the angular momenta of which were defined as $S_z = +\hbar/2$ and $-\hbar/2$, respectively [26].

Later, Nevill Francis Mott proposed the theory of electron spins and subsequently presented the famous “two-current” model in 1936 [27], which was regarded as the beginning of the development of spintronics. According to this model, the resistances for the up- and down-spins were independently defined (see Fig. 2.1). This model considered the spin-flip scattering to be negligible in comparison to the other types of scattering processes, such as electron-electron and electron-phonon scattering.

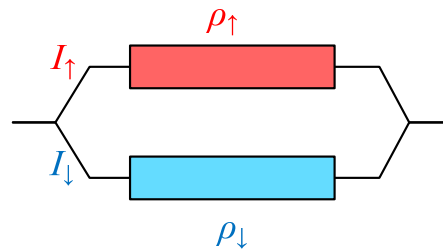


Figure 2.1: Schematic diagram for spin-dependent conduction via independent up- and down-spin channels.

The up- and down-spins can be generated using a ferromagnetic (FM) material [28,29]. The elementary ferromagnetic transition ($3d$) metals, Fe, Co, Ni and their alloys, are vital for such spin generation. In these metals, there is imbalance between up- and down-spins at the Fermi energy level (E_F) [see Fig. 2.2(b)]. The spin imbalance is induced by the spin-split density of states (DOS) of $3d$ bands at E_F due to the exchange interactions between electron spins [25,30,31]. The imbalanced bands overall generate a spontaneous mag-

netic moment in the ferromagnetic materials which can be expressed as follows:

$$\mathbf{M} = \mu_B (n_\uparrow - n_\downarrow). \quad (2.1.1)$$

Here, \mathbf{M} is the net magnetic moment per unit volume, μ_B represents the Bohr magneton and n_\uparrow (n_\downarrow) is the number of up-(down-)spin electrons.

At the Fermi level, there are equal numbers of 4s electrons for both spins, which play a key role in conduction [see Fig. 2.2(b)]. This is because the 4s electrons have greater mobility as compared with the 3d electrons. These 4s electrons become spin-polarised via the s - d interaction and carry the intrinsic spin imbalance at E_F [27]. The spin-imbalanced DOS at E_F leads to heavily spin-dependent scattering. At the point where the spin-flip scattering events can be ignored, the electron conduction takes place simultaneously through the two spin channels whose conductivities are differentiated. This leads to spin polarisation (P) as follows:

$$P \equiv \frac{N_\uparrow - N_\downarrow}{N_\uparrow + N_\downarrow}, \quad (2.1.2)$$

where N_\uparrow (N_\downarrow) refers to the density of state of the up-(down-)spin electrons at E_F , corresponding to a spin orientation that is antiparallel (parallel) to the overall magnetic moment [4].

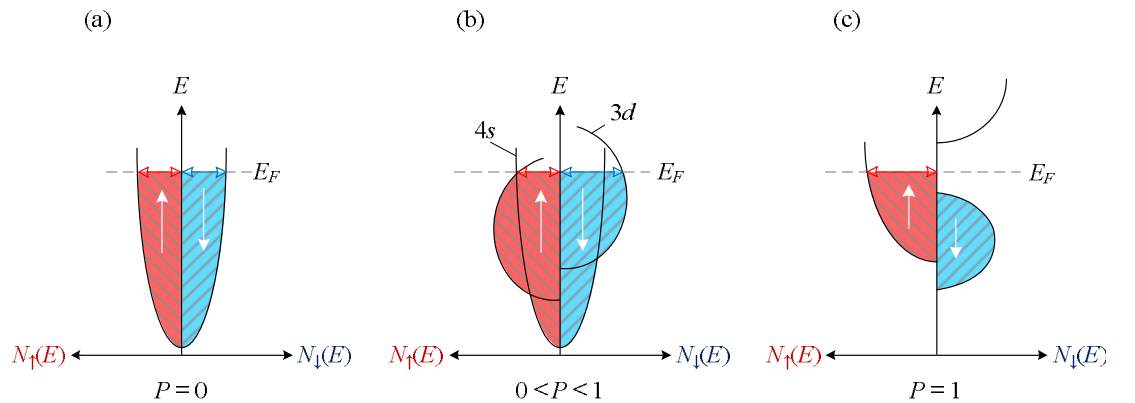


Figure 2.2: Schematic diagrams of spin-resolved DOS for (a) a non-magnetic metal, (b) a ferromagnetic transition metal and (c) a half-metallic ferromagnet.

Two distinctive situations for the spin polarisations are also shown in Figs. 2.2(a) and (c). When the Fermi level is equally filled with both spin states, there is no net spin polarisation, resulting the material to be a non-magnet (NM) [see Fig. 2.2(a)]. On the other hand, if there is only one spin state available at the Fermi level, there is 100% spin polarisation, resulting the material to be known as a half-metallic ferromagnet [see Fig. 2.2(c)] [32]. Table 2.1 presents a list of P for different ferromagnetic materials.

Table 2.1: Spin polarisation values of various ferromagnets.

Materials	Spin polarisation	References
Fe	40%-55%	[33–35]
Co	35%-52%	[33–35]
Ni	23%-46.5%	[33–35]
Ni ₈₀ Fe ₂₀	25%-37%	[34, 35]
CrO ₂	90%-100%	[34–37]
NiMnSb	58%, 100% (theory)	[34, 35, 38]
Ni ₂ MnIn	34%	[34, 35, 38]

In early experiments in spintronics, tunnelling measurements had a critical role. Meservey and Tedrow carried out a series of experiments using ferromagnet/insulator/superconductor (FM/I/S) structures [39–41], in which the spin polarisation of a tunnelling current remains spin-polarised in the S layer. Julliere successfully measured tunnelling magnetoresistance (TMR) in FM1/I/FM2 junctions in 1975 [42]. Figure 2.3 presents tunnelling conductances for the parallel ($\uparrow\uparrow$) and antiparallel ($\uparrow\downarrow$) magnetisation configurations of the two ferromagnetic layers (FM1 and FM2). Julliere's model has been used to calculate a TMR ratio as follows.

$$\text{TMR} = \frac{R_{\uparrow\downarrow} - R_{\uparrow\uparrow}}{R_{\uparrow\uparrow}} = \frac{G_{\uparrow\uparrow} - G_{\uparrow\downarrow}}{G_{\uparrow\downarrow}}, \quad (2.1.3)$$

where resistance R and conductance G ($= 1/R$) depend on the parallel ($\uparrow\uparrow$) and antiparallel ($\uparrow\downarrow$) configurations of FM1 and FM2.

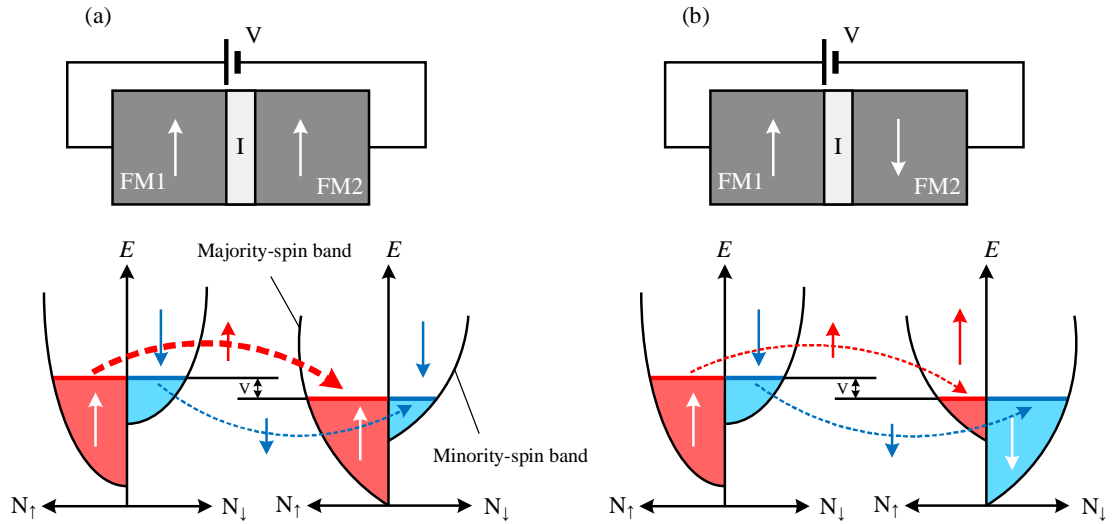


Figure 2.3: Schematic diagrams of spin-polarised electron tunnelling across a FM1/I/FM2 junction in (a) parallel and (b) antiparallel configurations. The bottom schematics show the corresponding spin DOS of the ferromagnets. Dashed lines show spin-conserved tunnelling.

2.2 Giant magnetoresistance (GMR) effect

Peter Grunberg and Albert Fert were awarded with the Nobel Prize in Physics in 2007 for their discovery of giant magnetoresistance (GMR) [23,43]. The GMR effect is based on a quantum mechanical magnetoresistive phenomena in a structure of FM1/NM/FM2. One can detect a considerable change in electrical resistance depending on a parallel or antiparallel configuration of the magnetisations in the FM layers as similarly observed in a TMR junction. For the antiparallel configuration, the net resistance is high and the net resistance is low for the parallel configuration. Based on the GMR effect, IBM has developed a read head [44] and has increased the annual growth rate of the areal density of hard disk drives (HDD) up to 60-100% (see Section 2.6.1) [45,46].

Two magnetic configurations for the GMR phenomena are shown in Fig. 2.4(a). With typical layer thicknesses (Fe: 12 nm and Cr: 1 nm [23]), the FM layers form antiparallel (AP) coupling without an external magnetic field, ow-

ing to the antiferromagnetic exchange coupling. However, in the presence of an external field, magnetisations in the FM layers are aligned in parallel (P) [43]. These two configurations can be detected by applying a sensing current in two directions as shown in Fig. 2.4(b). A flow of the current can be either in the plane (CIP) [23, 43] or perpendicular to the plane (CPP) [47]. The GMR effect arises from the spin-dependent scattering at the FM/NM interfaces for the both cases.

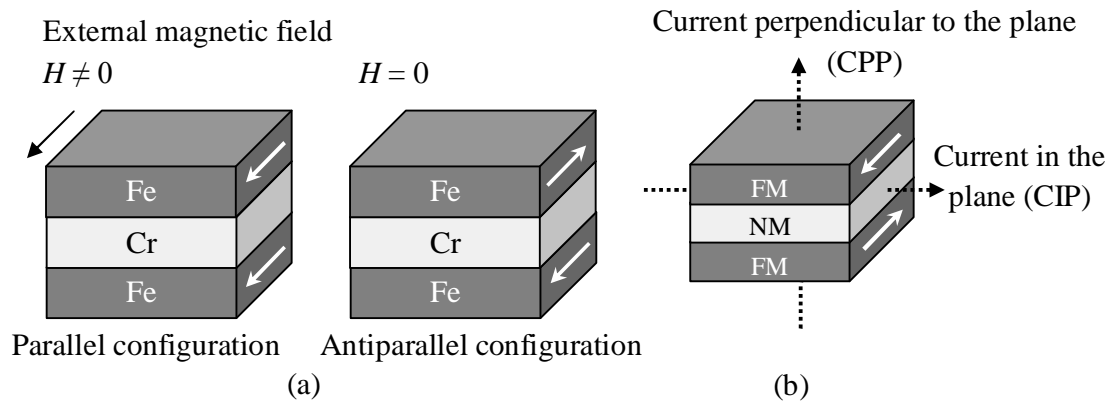


Figure 2.4: (a) Trilayer consisting of FM Iron (Fe) and NM Chromium (Cr) with the parallel (left) and antiparallel (right) configurations. The FM layers are shown in grey and the NM layers are shown in white. The directions of the FM magnetisations are indicated by white arrows. (b) Basic setup for the GMR experiment. The directions of the sensing currents for the CPP- and CIP-GMR measurements are shown by dashed arrows.

A simple resistance model based on the Mott two-current model [48] provides qualitative explanation of the GMR effect (see Fig. 2.5). The conduction electrons in metals are assumed to be divided into two distinct up- and down-spin channels. These channels demonstrate different resistivities for the two types of spin-polarised electrons. A low resistance channel is formed by an electron in parallel to the majority spins as shown in Fig. 2.5(a). On the other hand, strong scattering occurs for an electron with its spin to be antiparallel to the spin polarisation of the majority electrons, forming a high resistance channel [see Fig. 2.5(b)]. According to the Mott model discussed in Section 2.1, these two channels are formed by the difference in the up- and down-spin DOS in a

FM metal at E_F [27]. For the P configuration these two channels are formed independently and only one of them are scattered, while they are both scattered at one of the FM/NM interfaces for the AP configuration. Therefore the AP configuration shows higher resistance than the P configuration.

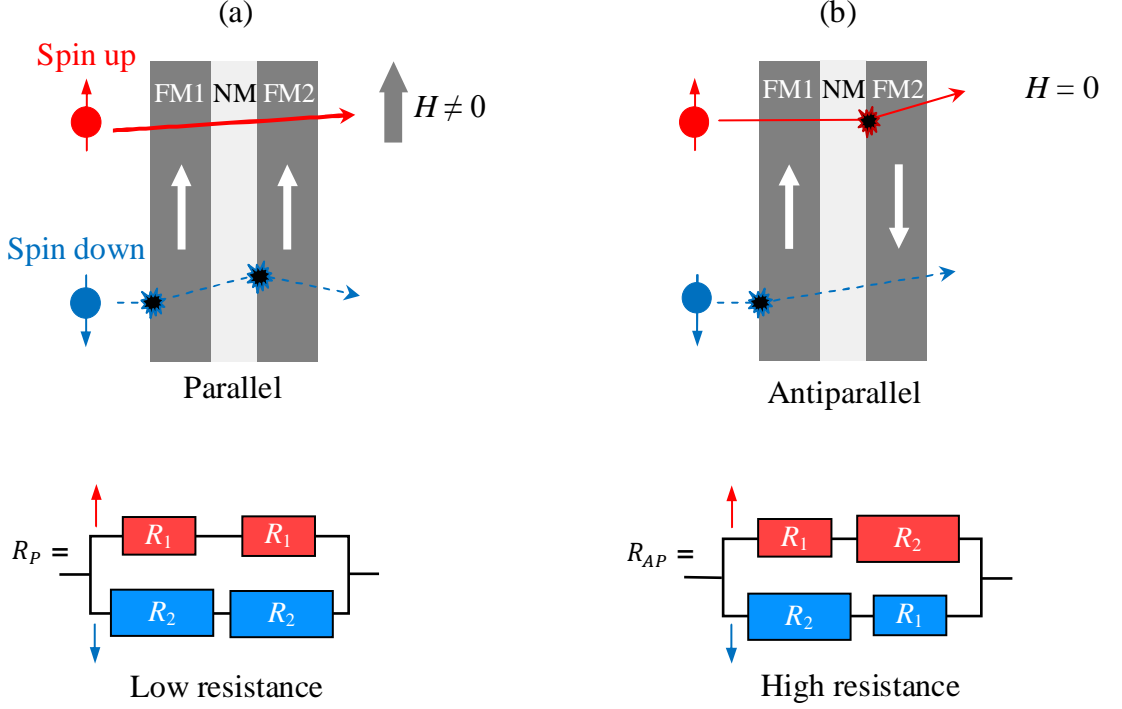


Figure 2.5: Schematic diagrams of electron flow in a trilayer for the (a) parallel and (b) antiparallel configurations. The magnetisation directions are indicated by the wide white arrows, which are opposite of the majority spin at E_F . The solid and dashed arrows are the flow paths for the up- and down-spin electrons, respectively. Bottom panels represent the corresponding resistance according to the two-current model.

As illustrated in Fig. 2.5, the resistances for the parallel and antiparallel configurations are expressed as follows [49].

$$R_P = \frac{2R_1R_2}{R_1 + R_2}, \quad (2.2.1)$$

$$R_{AP} = \frac{R_1 + R_2}{2}, \quad (2.2.2)$$

where $R_1(= R_{\uparrow\uparrow} = R_{\downarrow\downarrow})$ and $R_2(= R_{\uparrow\downarrow} = R_{\downarrow\uparrow})$ are the resistances for the P (1)

and AP (2) channels, respectively. Accordingly a GMR ratio can be defined by

$$\text{GMR} = \frac{\Delta R}{R_P} = \frac{R_{AP} - R_P}{R_P} = \frac{(R_1 - R_2)^2}{4R_1R_2}. \quad (2.2.3)$$

The description given above can be applied to the CPP configuration. In this case, the spin polarisation of the travelling electrons is maintained within the critical length. This distance is defined as the spin diffusion length (λ_s) [4]. It is worth mentioning that the GMR mechanism in the case of the CIP configuration is different and is defined by the mean free path [4]. It has been proven through experimental studies that a GMR ratio in the CIP configuration is much smaller than that in the CPP configuration [47,50] (typically two orders of magnitude in a GMR ratio at RT [51]). From the application point of view, this fact makes the CPP configuration to be more efficient as compared to the CIP configuration.

2.3 Spin injection, accumulation and detection

In order to illustrate the spin-dependent transport across a transparent FM/NM interface, the elementary concepts as discussed in the previous sections, *i.e.*, spin DOS and the two-current model, have been employed [52]. Based on the Boltzmann theory, detailed theoretical modelling of multiple transparent FM/NM interfaces has been developed by Valet and Fert [53]. They have modelled the spin-dependent scattering and spin accumulation in the CPP-GMR multilayer. Results obtained from experiments can be quantitatively analysed using this standard model. A schematic setup of typical electrical spin injection is shown in Fig. 2.6. When a FM metal is attached to a NM metal, a current density (J) is driven perpendicular to the FM/NM interface by applying an electric field (E).

As a consequence of the spin-dependent conductivities in the FM electrode, *i.e.*, $\sigma_{\uparrow}^{\text{FM}} \neq \sigma_{\downarrow}^{\text{FM}}$, a current in FM becomes spin-polarised, *i.e.*, $J_{\uparrow}^{\text{FM}} \neq J_{\downarrow}^{\text{FM}}$. On the other hand, the corresponding conductivities in the NM electrode is the same ($\sigma_{\uparrow}^{\text{NM}} = \sigma_{\downarrow}^{\text{NM}}$) since there is no spin-imbalance in the DOS. This harms the

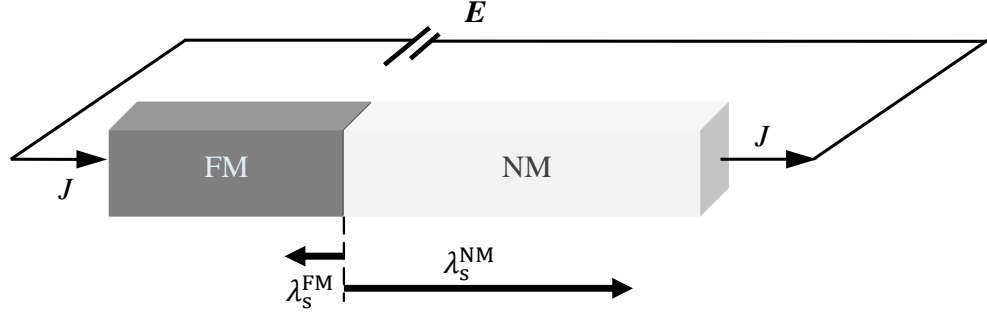


Figure 2.6: Schematic setup of a FM electrode in contact with a NM electrode for spin injection. λ_s^{FM} and λ_s^{NM} refer to spin diffusion lengths in the FM and NM layers, respectively.

conservation of a spin-polarised current density across the interface ($\nabla \cdot \vec{J} = 0$) and consequently an equilibrium state is lost near the FM/NM interface. This results in the accumulation of imbalanced electron spins in the NM layer in the vicinity of the interface. In NM, this spin-accumulated region is extended up to the thickness of λ_s^{NM} (NM spin diffusion length) from the interface. This induces a split in the spin DOS at E_F for the up- and down-spin carriers by

$$\nabla \vec{J}_{\uparrow\downarrow} = -\nabla \vec{J}_{\downarrow\uparrow}. \quad (2.3.1)$$

This results in the introduction of a net spin-polarised current into the NM layer within λ_s^{NM} . Although the diffusion length in the FM layer is short, *e.g.*, $\lambda_s^{\text{NiFe}} \approx 5$ nm at room temperature (RT) [54,55], the diffusion length can be large in NM, *e.g.*, $\lambda_s^{\text{Cu}} \approx 350$ nm [16] and $\lambda_s^{\text{Al}} \approx 600$ nm at RT [56], because the density of spin scattering centres is low. In addition, spin flip occurs to compensate the spin imbalance at E_F in both NM and FM, which can be negligible for the first approximation.

One can illustrate such accumulated spin transport by characterising the charge current density ($J = J_{\uparrow} + J_{\downarrow}$) and the spin current density ($J_s = J_{\uparrow} - J_{\downarrow}$) as follows [57].

$$\vec{J}_{\uparrow\downarrow} = -\frac{\sigma_{\uparrow\downarrow}}{e} \nabla \mu_{\uparrow\downarrow}, \quad (2.3.2)$$

where e is the electron charge, $\sigma_{\uparrow(\downarrow)}$ is the spin-dependent conductivity and $\nabla\mu_{\uparrow(\downarrow)}$ refers to the local variation in the spin-dependent electrochemical potential for the up-(down-)spin electrons. It is evident from Eq. 2.3.2 that a gradient of the electrochemical potential for the two spin orientations drives the corresponding electrons diffusively. The electrochemical potential is expressed in Fig. 2.7 as a function of position from the FM/NM interface. For a transparent interface, the electrochemical potential, μ_{\uparrow} (shown as a red solid curve) and μ_{\downarrow} (shown as a blue dashed curve), are continuous. Moreover the electrochemical potential, μ (shown as a green dash-dotted line), is calculated as an average between μ_{\uparrow} and μ_{\downarrow} in NM [$\mu^{\text{NM}} = 1/2(\mu_{\uparrow} + \mu_{\downarrow})$]. However, in FM, it is a weight average given by $\mu^{\text{FM}} = \alpha_{\text{FM}}\mu_{\uparrow} + (1 - \alpha_{\text{FM}})\mu_{\downarrow}$, where $\alpha_{\text{FM}} (= \frac{N_{\uparrow}(E_{\text{F}}) - N_{\downarrow}(E_{\text{F}})}{N_{\uparrow}(E_{\text{F}}) + N_{\downarrow}(E_{\text{F}})})$ refers to spin imbalance at E_{F} in FM ($0 \leq \alpha_{\text{FM}} \leq 1$). This induces a gap in the electrochemical potential, *i.e.*, $\Delta\mu = \mu_{\text{FM}} - \mu_{\text{NM}}$, at the interface as shown in Fig. 2.7.

In order to describe the propagation of the accumulated spins in the NM metal, the spin diffusion equation can be employed as [58]:

$$\frac{d\mu_s}{dt} = D\nabla^2\mu_s - \frac{\mu_s}{\tau}, \quad (2.3.3)$$

where D is the diffusion coefficient in NM, τ is the spin relaxation time and $\mu_s (= \mu_{\uparrow} - \mu_{\downarrow})$ is the non-equilibrium accumulated spins. When equilibrium is achieved in the system, *i.e.*, $d\mu_s/dt = 0$ by $\mu_s(x \rightarrow \infty) = 0$, exponential decay of accumulated spins is anticipated as a function of distance from the interface (x) to be defined by $\mu_s \propto \exp(-x/\lambda_s^{\text{NM}})$. In this expression, λ_s^{NM} refers to the spin diffusion length in the NM electrode and is given by $\sqrt{D\tau}$. The mechanism which causes the spin relaxation in NM is elaborated in Section 2.5.

As shown in Fig. 2.7, spin accumulation in NM can be treated as a supply of spin electromotive force that generates a voltage $\Delta V \propto (\mu_{\uparrow} - \mu_{\downarrow})$. This can be detected through an additional ferromagnetic electrode [60], by forming a FM1/NM/FM2 trilayer as similar to the CPP-GMR junction. The electrochemical potentials are shown in Fig. 2.8 as a function of position for the

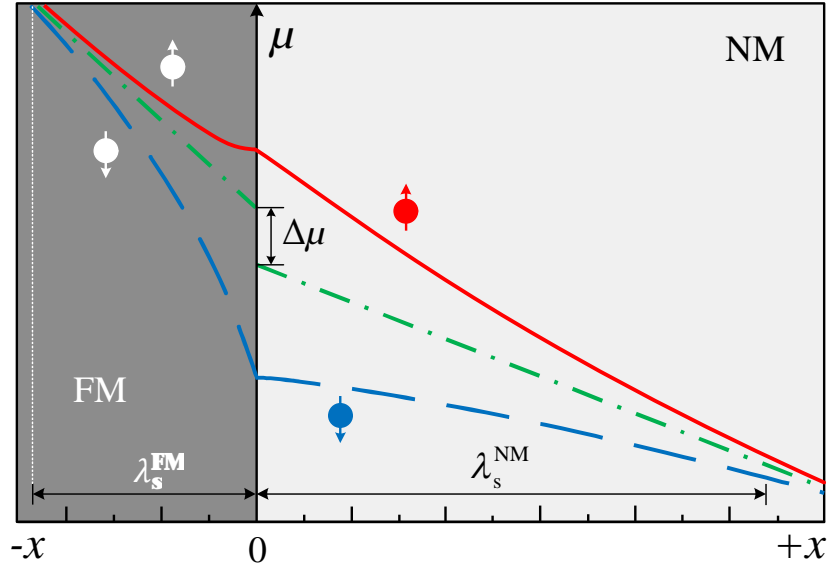


Figure 2.7: Spatial distribution of the spin-dependent electrochemical potentials (μ) for the both spin orientations near the FM/NM interface in the presence of a charge current. After [59].

FM1/NM/FM2 trilayer, of which magnetisations are (a) parallel and (b) antiparallel. By injecting a spin-polarised current from FM1, spin accumulation occurs in NM and diffuses into NM. The dashed-dot (green) line in Fig. 2.8 indicates the average spin potential ($\sim E_F$) and its gradient provides the electrical field that drives the charge current. The solid (red) curve indicates up-spin population and dashed (blue) curve indicates the down-spin population. A change in the magnetisation alignments between FM1 and FM2 results in a change in the electrochemical potential distributions. It is easy for the up-spin electrons to diffuse into FM2 for the P configuration [see Fig. 2.8(a)]. This is shown by the reduced electrochemical potential at the interface between NM and FM2. For the AP configuration as shown in Fig. 2.8(b), it is difficult for the up-spin electrons to diffuse into FM2 by the increased electrochemical potential at the NM/FM2 interface. Unlike the down-spin electrons, the up-spin electrons experience high resistance. Moreover, the accumulated spin voltage in the antiparallel state $V_{\uparrow\downarrow}$ developed at the two interfaces is higher as compared to that of the P state $V_{\uparrow\uparrow}$.

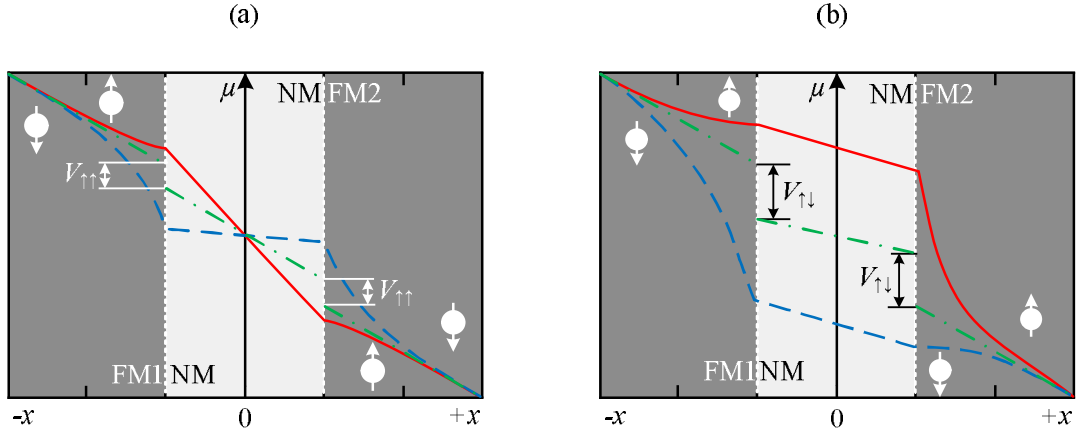


Figure 2.8: Spatial distributions of the spin-dependent electrochemical potentials μ for the both spin orientations in a FM1/NM/FM2 structure with the presence of a charge current for the (a) parallel and (b) antiparallel magnetisation configurations. After [61].

2.4 Lateral spin-valves

One can use the FM/NM/FM structure for executing the processes of spin injection, transport and detection as mentioned in Sections 2.2 and 2.3. The estimated GMR signal from such a structure is controlled by J_s as well as J and the charge current partly obscures the spin-related effects. For example, stray fields induced by the magnetisation reversal of the FM contacts can generate a local Hall voltage in NM. Such a Hall voltage may be considered as a part of the GMR effect by mistake. An intrinsic effect of anisotropic magnetoresistance (AMR) can also be misleadingly included in the signal, which arises from the spin-orbit coupling and its magnitude is found to be dependent on the orientation of J with respect to the magnetisation of the FM contacts [62].

Utilisation of a pure spin current is ideal approach to avoid such parasitic signals. Spins passing through a metal without any net charge flow constitute such a pure spin current. Here, the number of up-spin electrons flowing in one direction is balanced by the same number of down-spin electrons traveling in the opposite direction ($J_{\uparrow} = -J_{\downarrow}$) [63]. Such a pure spin current can be pro-

duced in a FM/NM bilayer as shown in Fig. 2.9(a). A charge current can be separated from a pure spin current in this structure. Spin-polarised electrons are accumulated in close proximity with the FM/NM interfaces, when the spin-polarised current, which consists of both spin and charge currents (shown by solid arrow), passing through the FM electrode enters the NM electrode. From the interface, the accumulated spins travel in both directions, *i.e.*, along the NM wire within the distance of spin diffusion length λ_s^{NM} . At the same time, the charge current is extracted only from one NM end (left-hand side of the NM wire). Hence, the pure spin current (dash arrow) without any net charge currents flows into the right-hand side of the NM wire [64]. Figure 2.9(b) depicts the spin-current flow in NM using the electrochemical potentials for up-spins (solid curve) and down-spins (dashed curve). It is worth mentioning that the greatest spin accumulation is realised at the interface and the spin accumulation decays exponentially with the distance from the interface as described in Eq. 2.3.3.

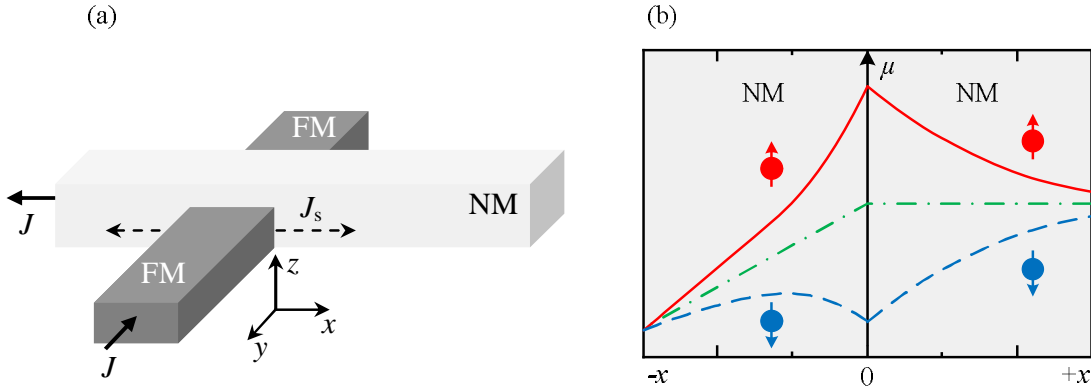


Figure 2.9: (a) Typical lateral structure with two electrodes. (b) Spatial distribution of the spin-dependent electrochemical potentials μ for the both spin orientations in the NM wire in (a). After [4].

The so-called non-local geometry can be used to detect the pure spin current electrically. A typical lateral spin-valve (LSV) structure used to achieve the non-local geometry is shown in Fig. 2.10(a). It consists of a pair of FM electrodes as a spin injector and detector, which are linked by a horizontal NM wire. As men-

tioned above, the spin accumulation is achieved close to the FM1/NM interface in this case. A pure spin current is generated and travels from the FM1/NM interface to the NM/FM2 interface. As FM has different $\sigma_{\uparrow}^{\text{FM}}$ and $\sigma_{\downarrow}^{\text{FM}}$, detectable voltages ($V_{\uparrow\uparrow}$ and $V_{\uparrow\downarrow}$) are generated with respect to the relative configurations of the magnetisations of FM1 and FM2, *i.e.*, parallel (P) and antiparallel (AP) [see Fig. 2.10(b)]. The voltage $V_{\uparrow\uparrow}$ in the P state is low and voltage $V_{\uparrow\downarrow}$ in the AP state is high. The high voltage of AP state is related to the down-spin $\mu_{\downarrow}^{\text{NM}}$ electrochemical potential and a low voltage in the P state relates to the up-spin $\mu_{\uparrow}^{\text{NM}}$ electrochemical potential in the NM wire. The pure spin-dependent signal (ΔR_s) can therefore be measured as below [65, 66].

$$\Delta R_s = \frac{\Delta V}{I} = \frac{V_{\uparrow\uparrow} - V_{\uparrow\downarrow}}{I} = \frac{\eta_1 \eta_2 \lambda_s \rho}{A} e^{-l/\lambda_s}, \quad (2.4.1)$$

where η_1 is the fractional spin injection efficiency at the FM1/NM interface, while η_2 is that at the NM/FM2 interface. ρ and A indicate the resistivity and cross-sectional area of the NM electrode. l is the edge-to-edge distance between the injector and detector electrodes. This equation again confirms that the output signals decay exponentially with l . In this study, LSV has been employed to characterise the spin-current transport and amplification as detailed in Chapters 6 and 7, respectively.

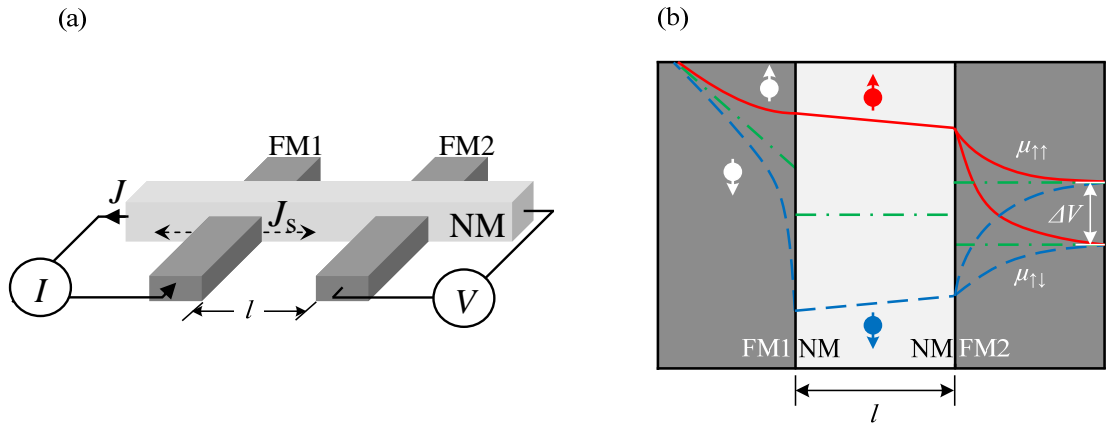


Figure 2.10: (a) Schematic illustration of the non-local measurement using a LSV structure. (b) Spatial distribution of the spin-dependent electrochemical potentials in the LSV device. After [4].

2.5 Spin relaxation mechanisms in metals

As mentioned in Section 2.3, the non-equilibrium spin-polarised electrons relax with distance. Such spin relaxation in metals are known to be caused by the Dyakonov-Perel mechanism, the Elliot-Yafet mechanism and magnetic impurity scattering [4, 67]. The following three subsections detail these spin relaxation mechanisms.

2.5.1 Dyakonov-Perel mechanism

The Dyakonov-Perel mechanism is only possible in a crystal that lacks inversion symmetry [4]. In such a crystal, electrons with the same momentum state can have different energies for the up- and down-spins. In order to understand this situation, one can consider the reference frame of the electrons producing an effective magnetic field due to their motion in an atomic-lattice site. For the lattice without the inversion symmetry, a magnetic field with different magnitudes is subjected to the electrons travelling in opposite directions (see Fig. 2.11). As a result, the average field experienced by a randomly scattering electron is non-zero. The Dyakonov-Perel mechanism is therefore irrelevant to the current study in this thesis since Copper in a face-centred cubic (fcc) lattice, which possesses inversion symmetry, has been used as a diffusive channel. Here, the energy of a diffusive electron between two subsequent scattering events is the same as the wavevector (k) is reversed without changing the spin orientation [4]. Moreover, the Elliot-Yafet mechanism and magnetic impurity scattering can only cause relaxation as detailed in the following subsections.

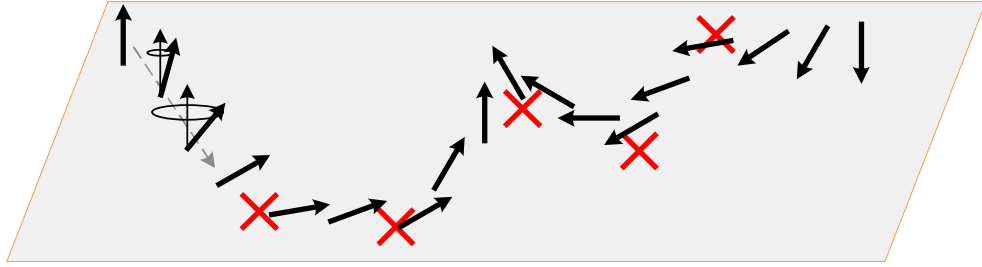


Figure 2.11: Schematic view of the Dyakonov-Perel spin relaxation mechanism. The black arrows indicate spins, which precess during their transport along their internal spin-orbit field induced by the crystal field. The dashed-gray arrow and the red crosses indicate the direction of the electron flow and scattering events, respectively. After [4].

2.5.2 Elliot-Yafet scattering

In a crystal, Bloch states (momentum eigenstates) are not eigenstates for spins and hence any spin-independent scattering results in spin mixing leading to spin relaxation. This is the fact on which the Elliot-Yafet mechanism is based [4, 67]. The spin degeneracy of the Bloch states originates from a local atomic electric field induced by crystalline lattice ions. This electric field can then mix the up- and down-spin states through the spin-orbit interactions. Consequently, an electron spin in the crystal does not share its quantisation axes with the FM injector or detector.

The actual spin polarisation depends, though to a small degree, on the wavevector of the electron (see Fig. 2.12). There are two possible mutually antiparallel spin orientations for each wavevector state defined by the FM injector and detector. However, the spin orientations related to different wavevector states can be oriented at different angles. If the wavevector or momentum of an electron is changed by a collision with a non-magnetic scatterer, such as an impurity or phonon in the crystal, it changes its spin orientation as well. This suggests the spin orientations related to the wavevector states before and after the scattering may not share their quantisation axis. Therefore, any collision

events with a spin scatterer, which result in altering the wavevector of an electron, can also flip its spin from the virtually down-spin state at k_1 to the virtually up-spin state k_2 . Such spin-flip scattering can occur in a sequence as shown in Fig. 2.12(b). Momentum relaxation, in small magnitude, always occurs with these scattering. In this study, the Elliot-Yafet mechanism plays the key role for the spin relaxation.

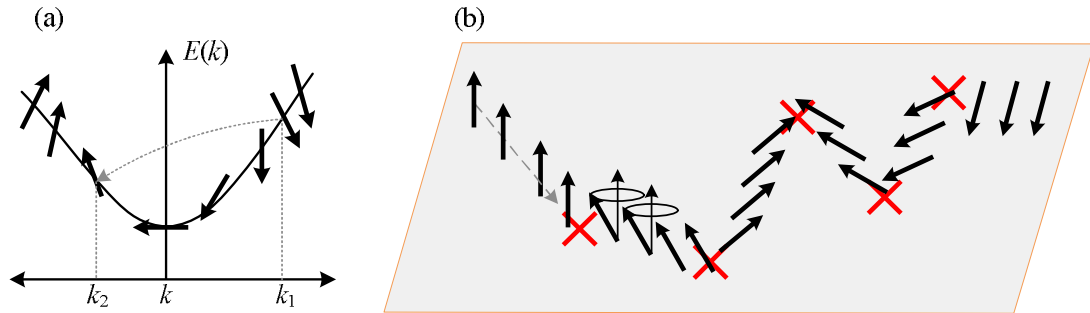


Figure 2.12: (a) Energy-wavevector relation showing the spin polarisations at different wavevector states. (b) Schematic view of the Elliot-Yafet spin relaxation mechanism. The black arrows indicate spins, which precess during their transport along their internal spin-orbit fields induced by the atomic ion. The dashed-gray arrow and the red crosses indicate the direction of the electron flow and scattering events, respectively. After [4, 67].

2.5.3 Magnetic impurity scattering

The other mechanism for the spin scattering and relaxation is induced in the NM host with small quantity of magnetic impurities. This mechanism involves exchange interactions between a conduction electron spin and a localised spin in the magnetic impurities [68]. The conduction electron spin is to be flipped when it is scattered by a magnetic impurity. At the same time, the localised magnetic moment is changed to compensate the change in the scattered electron spin.

A competition is induced among the conduction electrons to form a singlet with the impurity spin, which is induced by the antiferromagnetic exchange coupling between the conduction electron and the magnetic impurity spin [68]. This competition becomes stronger for the non-magnetic and magnetic scattering. The conduction electrons screen the magnetic impurity spins at low temperatures, leading to reduce the magnetic scattering rate. Therefore, at such temperatures (typically 5 to 10 K for metals [30, 69]), the spin scattering from magnetic impurities becomes significant. This temperature is unique for a host material and impurity, which is known as Kondo temperature [30, 69–71]. Hence, such magnetic impurity scattering can be negligible in this study, carried out at RT.

2.6 Spintronic devices

In the previous sections, the fundamental principles of spin-dependent transport are reviewed. Namely, it is shown that a spin-polarised current can be generated, transported and detected in a FM1/NM/FM2 structure. In this section, spintronic devices are described by implementing these principles.

2.6.1 Spin-valve read heads

In 1991, Dieny *et al.* [44] reported the first observation of the GMR effect in a spin-valve consisting of a FM1/NM/FM2 trilayer, in which one FM magnetisation was fixed (pinned) by coupling with an antiferromagnetic (AF) layer, while another was free. Figure 2.13(a) shows a schematic diagram of the spin-valve structure. Very small magnetic fields of less than 10 Oe can switch the magnetisation of the free layer and the magnetic configurations can be read electrically as GMR signals. A spin-valve read head sensor for a hard disk drive (HDD) has been accordingly developed in 1997 by IBM, which is the first commercial

application in the field of spintronics. It enables HDD to read the data bit in a scalable and sensitive way, resulting the areal density growth to be 60-100% every year [45,46].

Figure 2.13(b) shows the basic structure of HDD. Here, a magnetic platter is used for recording, which rotates at high speed (typically between 4200 and 15000 rpm). A head is used for writing and reading the digital signals in the form of "0" or "1" from the circular disk tracks. The HDD head is known as a flying head as it stays above the rotating disk with small gap (< 3 nm) as shown in Fig. 2.13(c). In the read head, the magnetisation of the free layer is flipped with respect to the stray field from the disk, leading to the change in the magnetoresistance in the spin-valve head. When the free layer becomes AP to the pinned layer, the high-resistance state is measured, corresponding to the signal "1". The P configuration provides the low-resistance state, corresponding to the signal "0". This change in the resistance, which is known as the GMR effect as discussed in Section 2.2, gives rise to the binary signals retrieved from HDD [see Fig. 2.13(d)].

The areal recording density of the HDD has been increased by three orders of magnitude since the introduction of the spin-valve head, from ~ 0.1 to ~ 100 Gbit/in², during the period from 1997 to 2003. The GMR head has been replaced by a TMR head with a magnetic tunnel junction (MTJ). The main difference between these heads is that in the MTJ a thin insulating layer is used instead of the metallic NM spacer layer in the spin-valve. The insulating layer can be an oxides such as Al₂O₃ or MgO. Seagate has first implemented the MTJ head into the HDD in 2004 [72]. A recording density of greater than 200 Gbit/in² and a data transfer rate of 1 Gbit/s has been achieved by the MTJ read head [63].

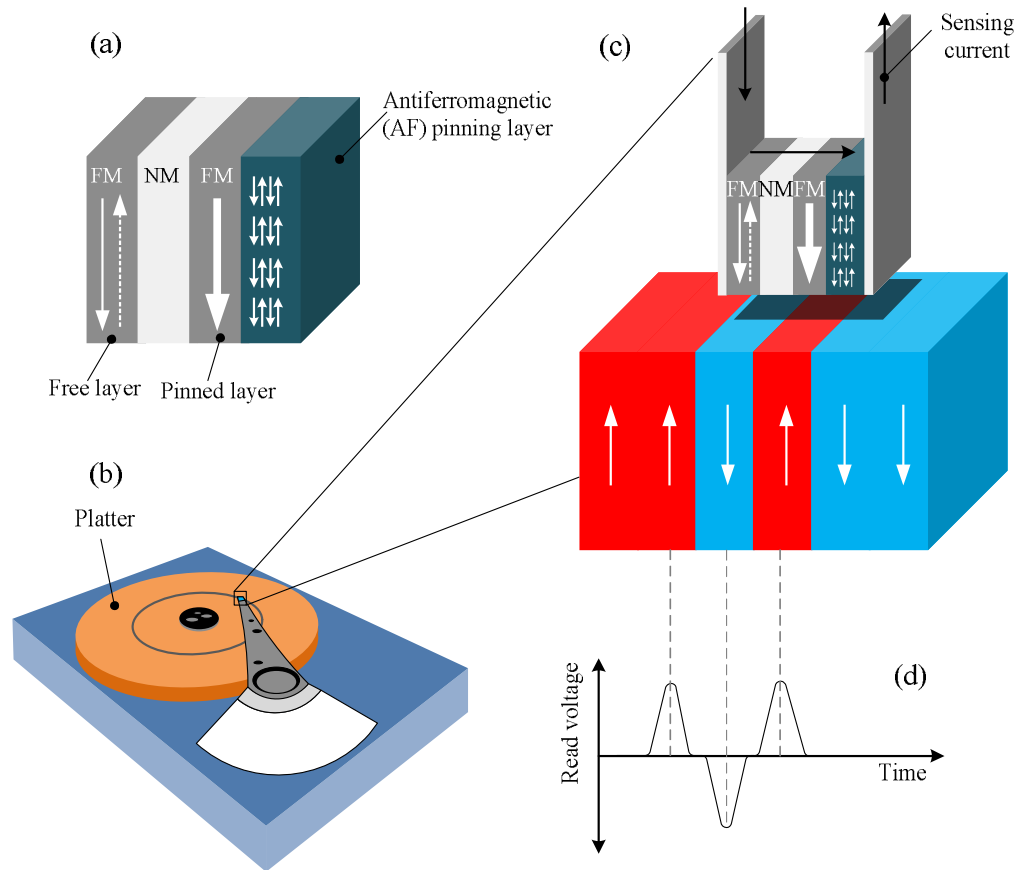


Figure 2.13: Schematic views of (a) a simple spin-valve structure, (b) HDD and (c) a magnetic recording mechanism with a read head sensor flying above the magnetic disk. (d) GMR signal corresponding to the parallel and antiparallel configurations between the free layer of the spin-valve and the data bit on the disk.

2.6.2 Magnetic random access memory (MRAM)

The other recent spintronic application is a non-volatile magnetic random access memory (MRAM). Unlike conventional random access memories (RAM), such as static RAM (SRAM) and dynamic RAM (DRAM), data bits in MRAM are not stored as an electric charge but as a magnetisation in a spin-valve or MTJ element. In MRAM, the logical “0” and “1” data are stored using the relative orientations of the free and pinned FM layers of the element. Either GMR or TMR effect is used for the data read-out.

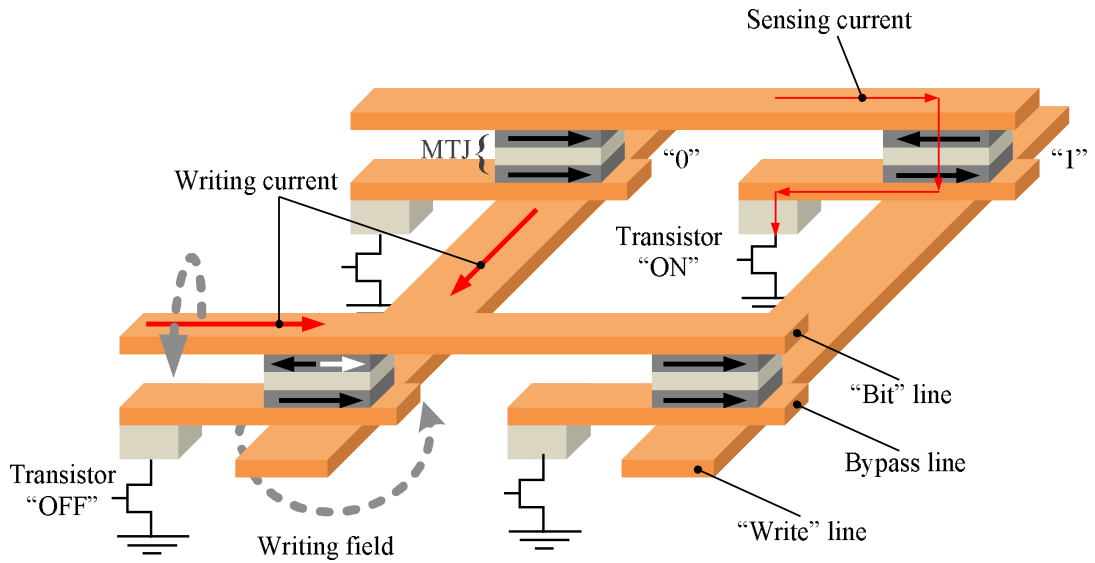


Figure 2.14: Schematic structure of MRAM. After [73].

Figure 2.14 shows a simplified structure of MRAM. If the orientation of the magnetisations in the two FM layers is in parallel, a large current is produced because of the lower resistance, which indicates the cell to be in the “0” state. The “1” state is achieved when the magnetisations have the AP configuration, flowing a small current because of the high resistance as shown in Fig. 2.14. For data recording in a MRAM cell, writing currents are passed through a pair of write and bit lines perpendicular to each other, generating magnetic fields, sum of which is large enough to change the free-layer magnetisation in the element.

In the field writing, false writing may happen, which is a serious problem. This is because the induced fields overlap over a small area and may change the magnetisation of the neighbouring elements. Additionally, the power consumption for the field writing increases by decreasing the cell size [63]. Therefore, a spin transfer torque (STT) technique has been developed to solve these problems as shown in Fig. 2.15 [63]. Here, a spin-polarised current transfers its magnetic momentum to the free ferromagnetic layer and switches the magnetisation. The current requirement for the STT writing is greatly decreased by 60% as compared with the field writing for a 20 nm diameter pillar [74].

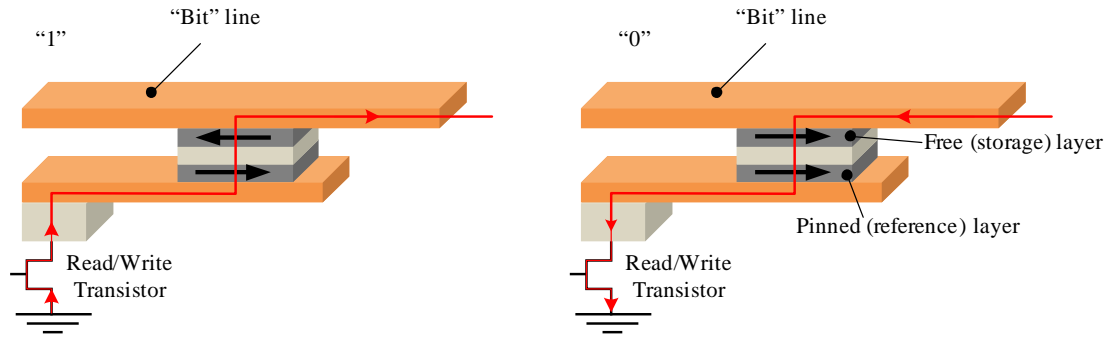


Figure 2.15: Schematic diagrams of STT-based magnetisation switching for the cases of the (a) P to AP and (b) AP to P configurations. After [4].

MRAM is expected to become the first universal memory advantageous over the conventional RAM. The power consumption of MRAM is low because the data is stored as a magnetisation in the FM layer and does not require electrical refreshing. On the other hand, DRAM (not SRAM) cells must have their bits to be refreshed thousands of times in a second to maintain their states. MRAM can also be used as a working non-volatile memory (NVM), like flash memory. However, the flash memory requires a high voltage (about 10 V) to inject hot electrons across the insulators to erase their data bits. Such a charge injection deteriorates the insulating barrier of the flash cells. Accordingly, only 10^6 - 10^8 write cycles are possible for the flash memory. However, the lifetime of MRAM is very long ($> 10^{15}$ cycles) because the write voltages do not exceed 1 V.

2.6.3 Spin-polarised field effect transistor (Spin FET)

A spin-polarised field effect transistor (spin FET) has been proposed by Datta and Das in 1990 [75] as shown in Fig. 2.16. The spin FET has a similar structure with the metal oxide semiconductor field effect transistor (MOSFET) except the fact that the source and drain are FM materials. The basic idea of this device is to control the spin orientation by applying an alternating gate voltage, which induces an effective magnetic field.

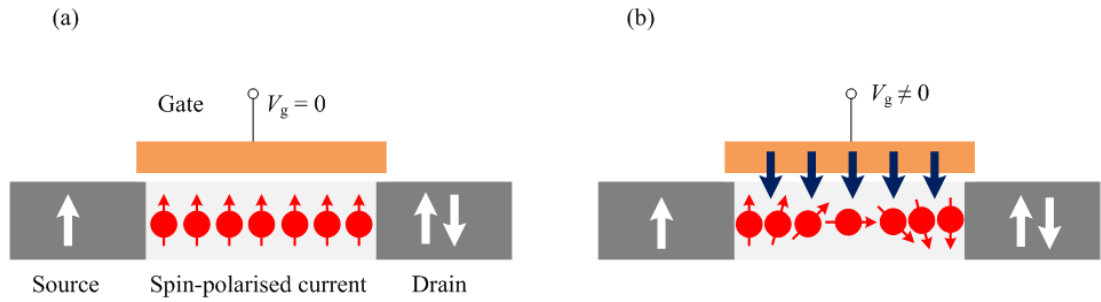


Figure 2.16: Schematic diagrams of Datta-Das spin FET operated (a) without and (b) with a gate voltage. After [75].

In the absence of a gate voltage, *i.e.*, $V_g = 0$, the FM source can inject a spin-polarised current into the channel, which is extracted by the FM drain without losing its initial spin orientation when the gate length is designed to be below the spin diffusion length. When the magnetisations of the FM layers are in parallel, the magnetoresistance is the minimum and the corresponding current can flow through the channel. The spin FET in this configuration is considered as in its “on” state as shown in Fig. 2.16(a). However, the electrons change their spin orientations when a gate voltage is applied, *i.e.*, $V_g \neq 0$. For this configuration the spin FET is turned “off” [see Fig. 2.16(b)]. However, the signals can be recovered by 360° rotation of the spin orientations by the gate. By forming the AP configuration between the source and drain, the signal can also be recovered by 180° rotation. It is therefore possible to make the FET operation to be more flexible as compared with the conventional MOSFET.

The spin FET is still a concept under development [2, 3, 76]. Various kinds of spin FETs using different FM materials, such as dilute magnetic semiconductors and half-metallic ferromagnets, have been studied [77]. There are still some outstanding technical issues, such as low spin-injection efficiency into the channel and effective gate control that can turn off the transistor completely, which need to be solved [77]. These issues are also applicable for the LSV investigated in this study.

Chapter 3

Computational Modelling of Modulated Lateral Spin-Valves

In this chapter, a two-dimensional model is described for the study of geometrical effects upon a spin-polarised electron current induced in a non-magnetic (NM) nanowire in a lateral spin-valve (LSV) device. Numerical methods are employed to simulate the electron spin diffusion in different NM-nanowire shapes in the non-local configuration. By using this simple model, the shapes have been optimised. Only asymmetric shapes added at the centre of the NM channel show a crucial difference in the diffusive rates for up- and down-spin electrons along the wire, which leads to the amplification of non-local spin-current signals.

3.1 Introduction

Spin-dependent transport phenomena in magnetic nanostructures have attracted great attention from their fundamental properties [78] to new spintronic device applications [63]. A LSV device, consisting of two ferromagnetic (FM) nanowires bridged by a NM nanowire, is one of the promising candidates as

such a structure [79, 80]. In the LSV, a pure spin current, *i.e.*, a diffusive flow of spin angular momentum with no net charge flow, has been demonstrated to be generated using the non-local configuration as discussed in Section 2.4 [16, 22, 81]. This implies that in such a configuration we can extract pure spin-polarised current contributions from the spin-dependent transport phenomena and can eliminate parasitic effects, such as the Hall effect and anisotropic magnetoresistance (AMR) [56]. Moreover, the separation between the spin injector and detector gives rise to a very thin spin-valve read sensor which could be implemented in next generation magnetic recording systems [82, 83].

However, the use of a conventional LSV geometry in device applications is still hampered by its small magnitude of the spin current. Therefore, spin-current amplification becomes crucial. This chapter focuses on the amplification of the pure spin-current signals by implementing new geometrical shapes using calculations. Here, the conventional NM straight nanowire in the LSV has been replaced by one with additional square or triangular wings implemented at the centre of the wire. Two-dimensional (2D) spin diffusion simulations have been performed to identify the geometrical effect. For this simulation, the spin-diffusion equation has been solved using a 2D finite element method implemented in FreeFem++ software [84]. The geometry of the modulated NM nanowire has been confirmed to be very important to amplify the spin signals. In the following section, the outline of this simulation software is described. Subsequent sections explain the development, limitations and validity of the model and the corresponding results.

3.2 FreeFem++

Many physics, natural science and engineering problems are modelled mathematically with partial differential equations (PDEs) with initial and/or boundary conditions. A PDE is a function with more than one independent variables.

They are very often not easy to solve analytically, especially when their computational domains have complex shapes. Numerical methods [85] are therefore used to sub-divide the complicated shape into a series of simpler shapes for which the PDE can be solved.

The finite element method (FEM) is the most powerful and popular technique to solve a PDE, and often forms the core of simulation software. FreeFem++ is one of these simulation packages, which is based on the FEM to solve linear and non-linear PDEs numerically. The FreeFem++ package allows quick specification of any linear PDEs and solves non-linear time-dependent problems. In addition, FreeFem++ provides a fast, light and user-friendly mesh-generating tool with parametric input and visualisation capabilities. The mesh is generated automatically based on the Delaunay-Voronoi diagram, which is refinement of the mesh by increasing the number of points at the boundaries [86].

Figure 3.1 shows a typical simulation flow in the 2D FreeFem++ simulator. The main steps in the implementation of the FreeFem++ simulator are outlined here. First, a computational domain boundary ($\partial\Omega$) needs to be described analytically using a parametric equation depending on x and y variables. When the boundary $\partial\Omega$ consists of more than one line segment, *i.e.*, $\partial\Omega = \sum_{j=1}^J \partial\Omega_j$ ($j = 1, 2, \dots, J$ and J is the number of the segment boundaries) [see Fig. 3.2(b) for example], each segment $\partial\Omega_j$ needs to be specified without overlapping one another except at the end points. Normally a set of triangulated mesh can be generated with the automatic mesh tools, *i.e.*, `buildmesh` and `square`, on $\partial\Omega$. In this study, to discretise the non-square geometries, more advanced mesh operators, *i.e.*, `trunc` and `movemesh`, have been used (see Appendix A for the code).

Once the domain is subdivided into a finite number of discrete-sized elements, the space over the mesh points must be defined with piecewise continuous polynomial functions, such as P0, P1 and P2. Thus the variables, whose values are determined at the representative mesh points, can also be approx-

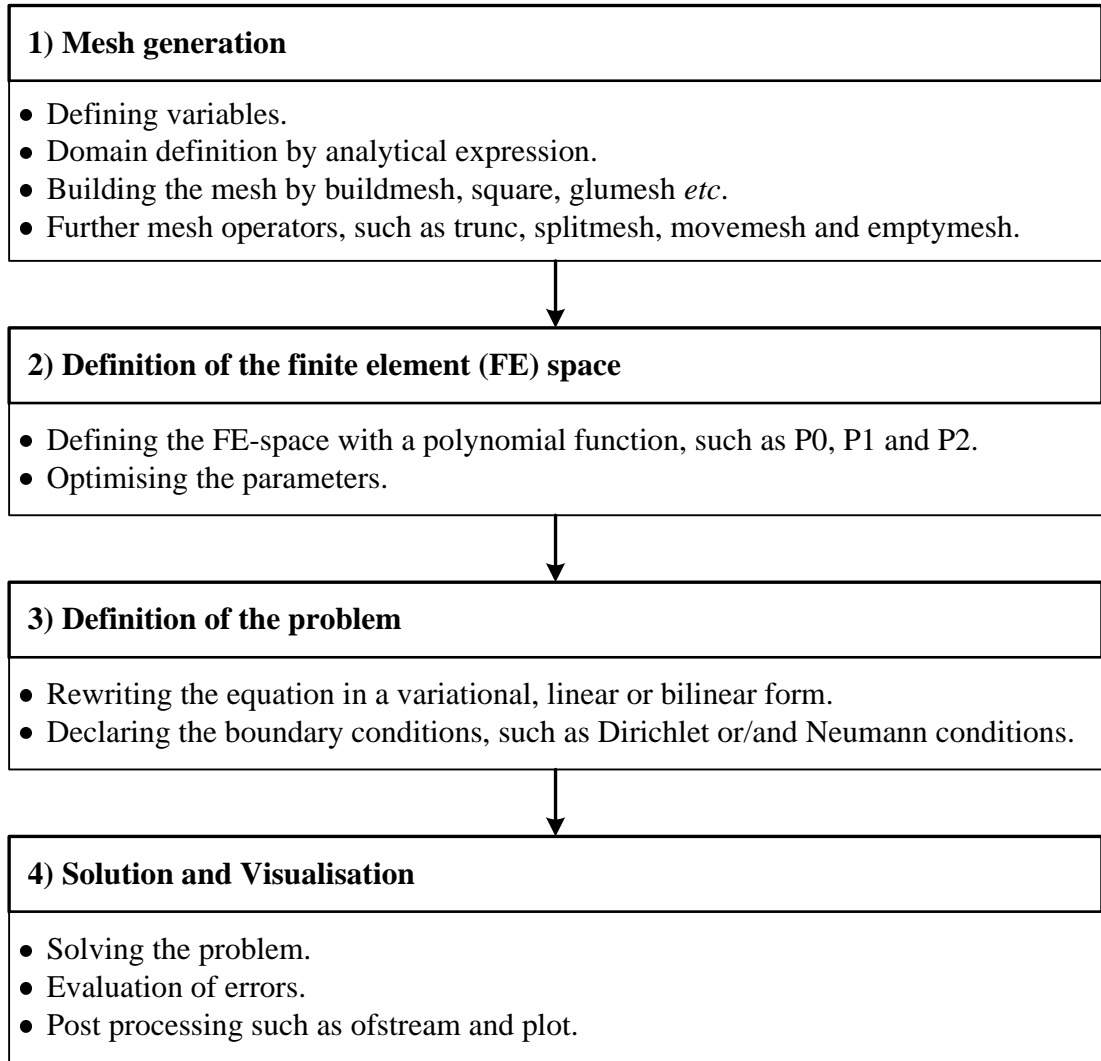


Figure 3.1: Typical simulation flow in the 2D FreeFem++ simulator.

imated in between the mesh points. For additional information on the finite element space, refer to the relevant textbooks [87–90]. In the next step, a variational formulation of the PDE and the associated boundary conditions need to be declared over the finite element space. Here, the boundary conditions, which specify a solution and its derivative, are usually known as Dirichlet- and Neumann-type boundary conditions, respectively. For a time-dependent problem, it is also crucial to declare the initial condition of the system at the starting point, *i.e.*, $t = 0$. The “*solve*” statement in FreeFem++ can then be used to solve the problem. Finally, a solution can be stored and displayed in several ways; conventional, vector and contour plots. In this study, the contour plots have been used.

3.3 Model development

A simplified model for realistic spin diffusion transport was studied in a 2D NM nanowire in a LSV structure. A series of Cu nanowires with different shapes were investigated to identify the effect of NM nanowire geometries on the amplification of a spin-current signal as shown in Fig. 3.2. The calculations were based on the spin-polarised electron transport in the non-local spin-valve (NLSV) geometry as shown in Fig. 3.2(a). A current was introduced from FM1 to the left end of the Cu nanowire, whereas a resulting voltage was measured between FM2 and the right end of the Cu nanowire. The NM geometries were modified from a simple straight nanowire without any additional shapes [see Fig. 3.2(b)] to relatively sophisticated geometries with additional shapes, *i.e.*, squares and triangles with equilateral, obtuse and right angles [see Figs. 3.2(c)-(f), respectively], with allowing 50 nm separation between the FM wires and these shapes. The key parameters used for these calculations were base length (b), height (h) and a number of the shape pairs (n). The edge-to-edge separation between the injector (FM1) and the detector (FM2), defined as the channel length (l), was varied depending on the base length of the implemented shapes, *i.e.*, $(50 + n \times b + 50)$ nm.

These shapes could be divided into two geometries; symmetric [Figs. 3.2 (a)-(d)] and asymmetric shapes [Fig. 3.2 (e) and (f)]. Signal amplification was not observed for any symmetric shapes, including the conventional straight NM nanowire in a LSV device. This was because the diffusive transport processes for up- and down-spin electrons in the NM nanowire experienced the same diffusion rate along the wire. Therefore these geometries did not introduce any changes between up-and down-spin electron transport. The spin signals should only be amplified by asymmetric shapes as detailed in Section 3.6.

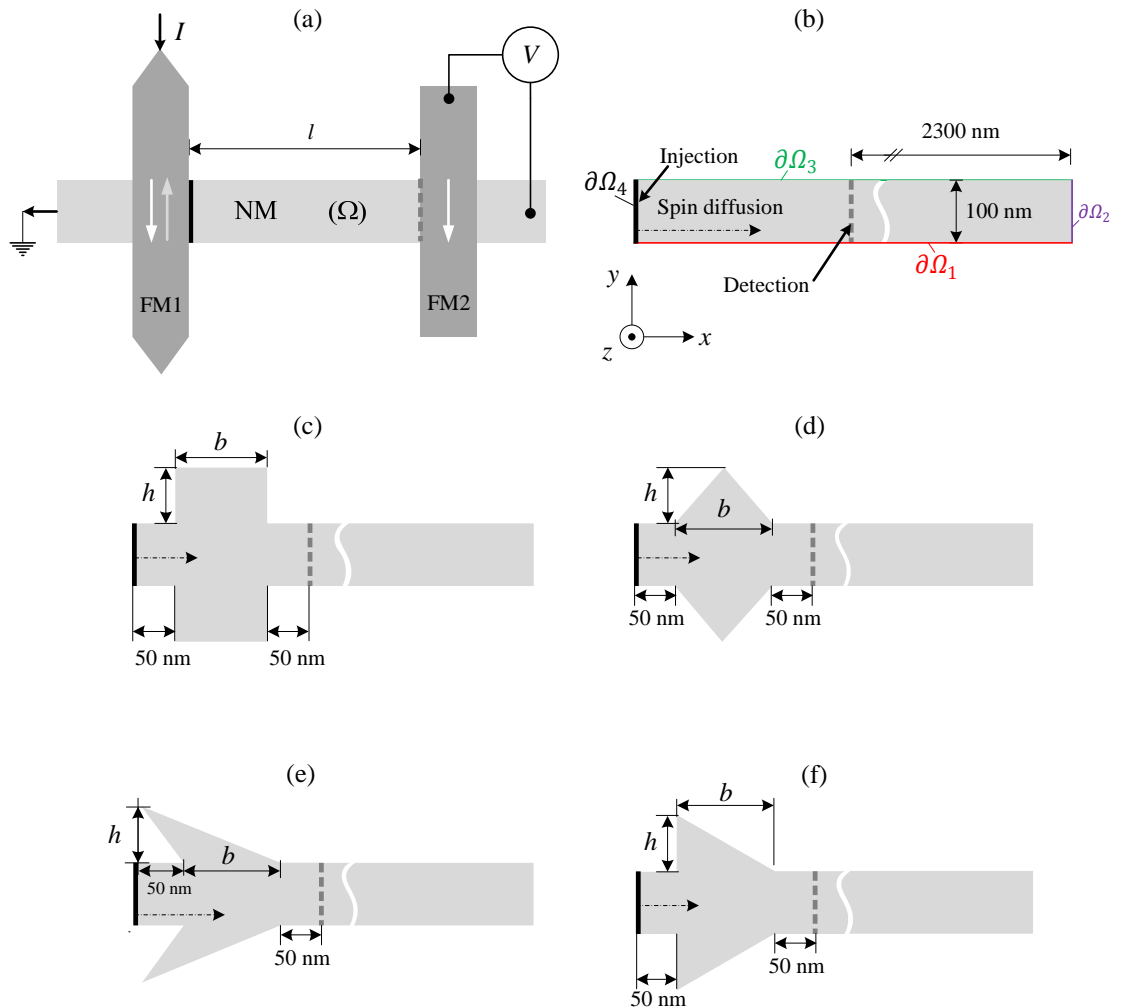


Figure 3.2: (a) Schematic diagram of the non-local measurement on a conventional LSV device. (b) Simplified straight wire geometry used for the 2D simulations. Nanowires with additional (c) squares and triangles with (d) equilateral, (e) obtuse and (f) right angles were also used for the simulations.

3.4 Assumptions and limitations of the model

In this model, the electron spin diffusion cannot be evaluated directly. In practice, when spin-polarised electrons are injected into the NM nanowire, a non-equilibrium spin accumulation is induced. This process causes the Fermi energy level to be split between up- and down-spin electrons. The accumulated spin signals decay gradually as they diffuse away from the injection point with a finite decay coefficient (τ). In this computational model the above spin-diffusion procedure is replaced by electron charge carrier diffusion. This simplified diffusion transport is governed by the time-dependent diffusion equation [53,91]:

$$\frac{\partial \mu_s(x, y, t)}{\partial t} = D \nabla^2 \mu_s(x, y, t) - \frac{\mu_s(x, y, t)}{\tau}, \quad (3.4.1)$$

where $\mu_s(x, y, t)$ is the density of free electron carriers in a 2D nanowire domain (Ω), D is the diffusion constant, ∇^2 denotes the Laplacian operator and τ is the spin-flip relaxation time. The boundary conditions for Eq. 3.4.1 are given by:

$$\mu_o(x, y, t = 0) = \delta(x - X) \quad (\text{Initial condition in } \Omega), \quad (3.4.2)$$

$$\frac{\partial \mu_s(x, y, t)}{\partial \hat{\mathbf{n}}} = 0 \quad (\text{Neumann boundary condition in } \partial\Omega), \quad (3.4.3)$$

$$\mu_s(x, y, t) \Big|_{x=\pm\infty} = 0, \quad (3.4.4)$$

where $\mu_o(x, y, t)$ is the density of injected electrons at $t = 0$, $\hat{\mathbf{n}}$ is the unit vector normal to the boundary surface ($\partial\Omega$) and δ is the Dirac delta function which represents the injected electron packet at a given position X in Ω . In order to satisfy Eq. 3.4.4 and to converge the results with respect to the grid parameters, the boundary condition at the detector end has been set to be 5 times longer than the spin diffusion length ($5 \times \lambda_s$) to avoid any electron interferences due to the reflection at the end of the wire [see Fig. 3.2(b)].

Here, a half-metallic spin injector was assumed by introducing only up-spin electrons from left to right in the device as shown in Fig. 3.2 and a flow-back current to the FM wire due to the charge accumulation in the Cu wire was

neglected. In the non-local measurements, these diffusive up-spin electrons were compensated by the flow of down-spin electrons in the opposite direction. These two spin currents were implemented in the model by two independent processes. For the up-spin electrons a packet of electrons as a pulse (Dirac-delta-like pulse) was introduced at the left Py/Cu junction (solid line, $\partial\Omega_4$, in Fig. 3.2) and the electron density was measured at the right junction (dashed line in Fig. 3.2) as a voltage (V_{LR}). On the other hand, the same number of the down-spin electrons was introduced at the right junction (dashed line in Fig. 3.2) and was monitored at the left junction [solid line, $\partial\Omega_4$, in Fig. 3.2(b)] as a voltage (V_{RL}) to compensate the above up-spin flow. These two opposite flows generated a pure spin current [16, 63, 78–80]. This model provided a measure of spin-current amplification of the non-local signals by taking their differences ($\Delta V_{\text{calc}} = V_{LR} - V_{RL}$) at each evolving time step (dt). Plots of ΔV_{calc} against time (t) could hence reveal the geometrical effect on the spin-dependent diffusive transport.

In this model, since the injected electron packet is considered to be 100% spin polarised, the calculated results cannot be compared directly with the experimental result quantitatively but they provide a measure of the spin-current amplification. It is also important to note that the modelling has been carried out in 2D, while in reality the device has a finite thickness, *i.e.*, in 3D. As a result the spin injection and detection is measured as a line density but in reality is an areal density.

3.5 Validation of the model

One of the major problems in simulating such a system is verifying whether the model is an accurate representation of the system being studied. If the calculations are not valid, any conclusions derived from it are of little value. Therefore validation is the most important step in any simulation models.

As a validation step, symmetric shapes, such as a straight wire and equilateral shaped wire, were studied. The aim of this step was to confirm that the calculation is reproducible and reliable. This could be done by designing a correct mesh distribution. The FEM technique was used to obtain numerical solutions for Eqs. 3.4.1-3.4.4. These equations were solved in two ways using two different types of mesh distributions. In the first way, the numerical domain was divided into a triangulated mesh with non-uniform size. Another way used an isotropic (uniform) mesh, which had the same separation length between the mesh points in all directions. An example of the geometry and the mesh used in the validation step was chosen to be a straight wire as shown in Figs. 3.3(a) and (b). The parameters used in this calculation were taken from Ref. [16] as listed in Table 3.1.

Table 3.1: Parameters used in the calculations.

Parameters	Notations	Values
Spin-flip relaxation time in Cu	τ	11 ps [16]
Diffusion coefficient of electrons in Cu	D	$0.01213 \text{ m}^2 \text{ s}^{-1}$ [16]
Wire strip width	w	100 nm
Introduced electron packet potential	μ_o	4.5 mV
Evolution time step	dt	0.25 ps
Complete time period	t_c	50 ps
Mesh size unit area	–	0.5 nm^2
Triangle height	h	10 to 100 nm
Triangle base length	b	100 to 450 nm

As mentioned in the previous sections, the rate of up-spin electrons diffusing along any symmetrically shaped NM nanowires must be the same with that of down-spin electrons diffusing in the opposite direction. This means identical electrical potentials formed across all the detection points, *i.e.*, $V_{\text{LR}} = V_{\text{RL}}$. In the numerical calculations, this can be accomplished only if the diffusion rate throughout the computational structure has absolute mesh independency. Figure 3.3(c) shows that the diffusive rates for the two opposite processes using

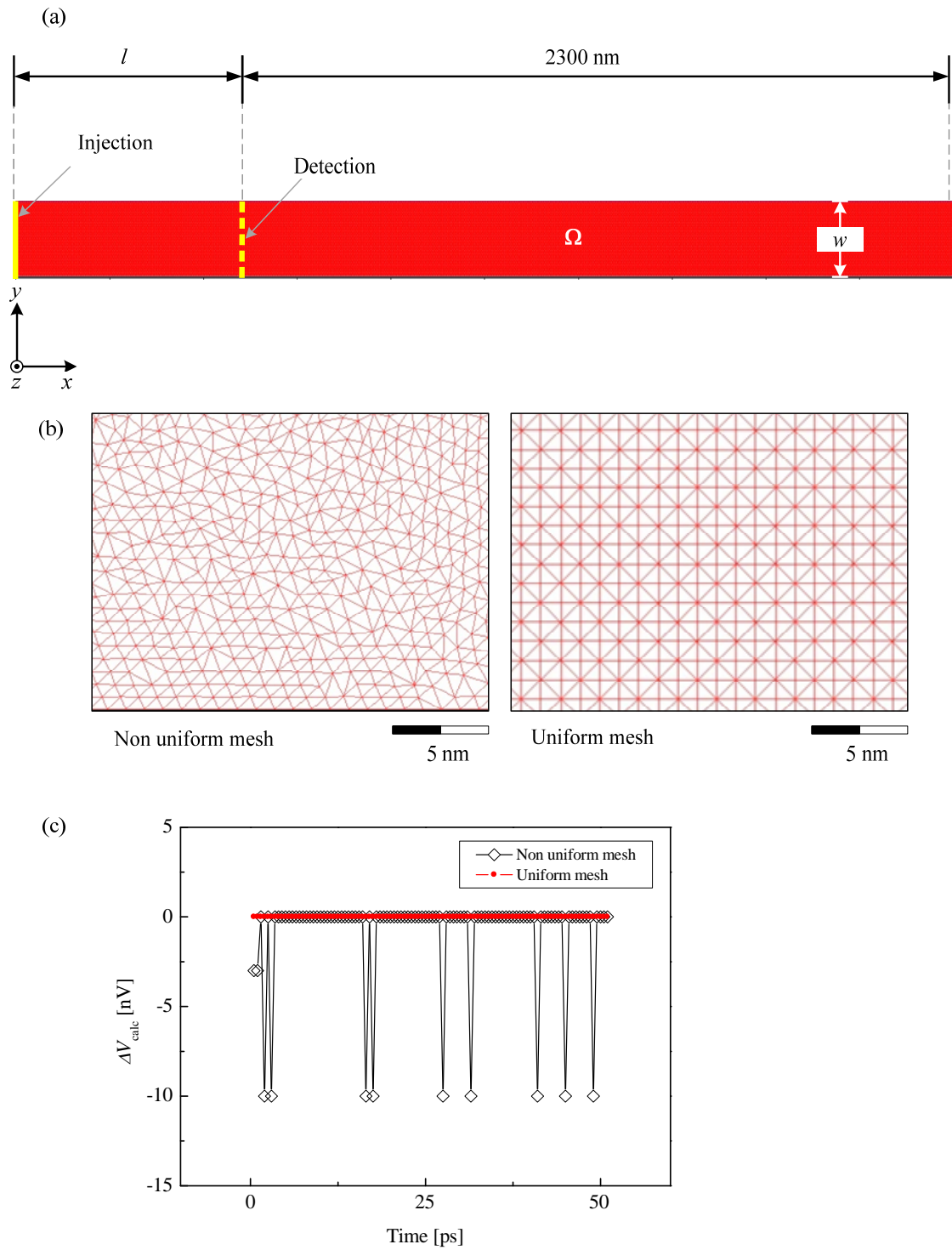


Figure 3.3: (a) A straight NM nanowire, which was calculated using (b) non uniform (left) and uniform (right) meshes. (c) Comparison of the time-dependent potential differences (ΔV_{calc}) for both meshes.

the non-uniform mesh exhibit finite values at evolving time steps. The result obtained from the left to right process is not identical to the result obtained in

opposite direction. Therefore, the calculations derived from the non-uniform meshed model cannot be relied upon. On the other hand, the uniform meshes show ΔV_{calc} to be zero at evolving steps as shown in Fig. 3.3(c). This confirms that the numerical calculations with the uniform mesh distribution are reliable and reproducible. This indicates that the model using uniform mesh can be used to evaluate the spin signals in LSV devices as described in the following sections.

3.6 Results and discussion

3.6.1 Symmetrical shapes

The first set of simulations was carried out for the symmetric shapes, a straight nanowire and nanowires with the squares and equilateral triangles as shown in Figs. 3.2(b)-(d). The calculations were performed for two independent time-dependent processes, one from left to right (up-spins) and another from right to left (down-spins). The corresponding snapshots of these simulations, which were taken at time $t = 1$ ps, were shown in Fig. 3.4. These snapshots revealed that the flow of the electrons remains laminar in the wires but they are disturbed strongly in the additional shapes. It should be noted that the electron distributions were symmetric with respect to the injection point.

The time evolution of the electron densities for the straight nanowire and nanowires with squares and equilateral triangles are presented in Figs. 3.5(a)-(c), respectively. As expected from Fig. 3.4, the up- and down-spin diffusion signals are confirmed to be identical. This leads to zero amplification, *i.e.*, $\Delta V_{\text{calc}} = 0$, as expected. The symmetric geometries of these 2D nanowires provide equal diffusive rates for both directions along x - and y -axes, *i.e.*, the transmission for the up- and down-spins is invariant in these symmetric geometries.

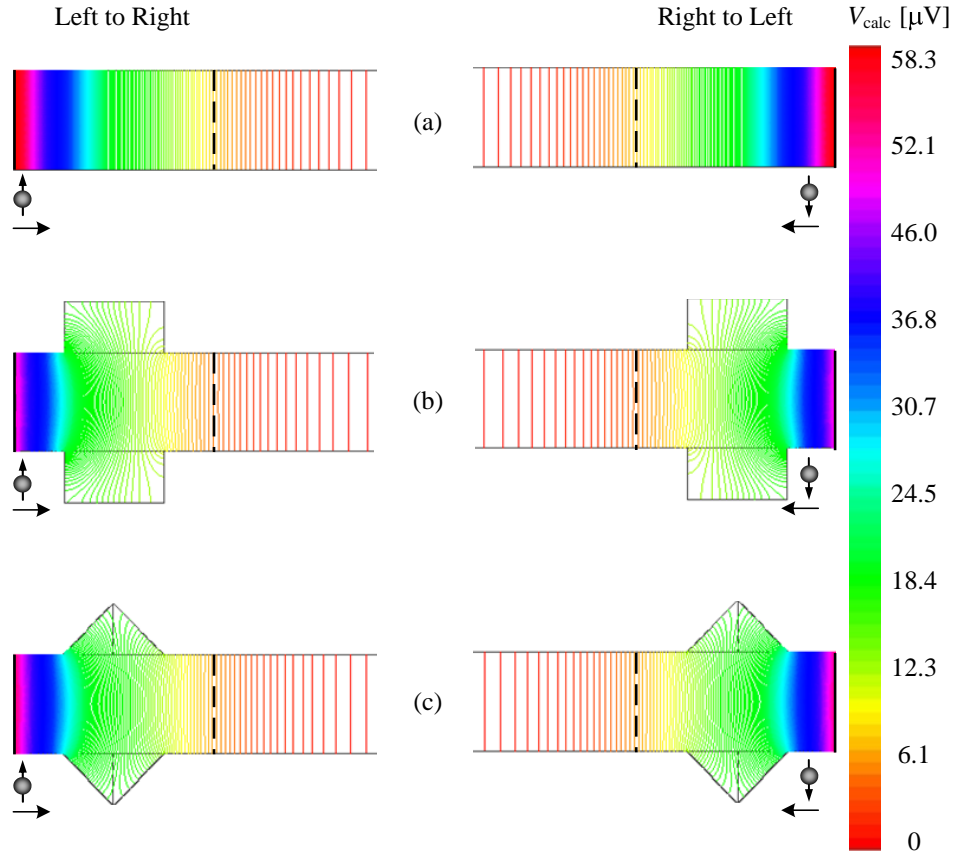


Figure 3.4: Snapshots of the electron distributions at $t = 1$ ps for the electrons flowing from left to right and right to left for the (a) straight nanowire and nanowires with the (b) squares and (b) equilateral triangles.

The wave front for both up- and down-spins can be defined as the density distributions (V_{calc}) in Figs. 3.5(a)-(c) as pronounced peaks at 1.34, 1.45 and 1.37 ps, respectively. This clearly indicates that the injected pulse signature is still preserved at the detection position. This happens because the evolving time scale is shorter than the spin-flip relaxation time ($\tau = 11$ ps at room temperature (RT) for Cu [16]). In other words, the detection position ($l = 200$ nm) is shorter than the spin diffusion length ($\lambda_s = 350$ nm at RT for Cu [16]). For the case of the straight nanowire [see Fig. 3.5(a)], one can note a sharper peak with full width half maximum (FWHM) of 6.43 ps as compared with 7.28 and 6.90 ps for the nanowires with the squares and equilateral triangles [see Figs. 3.5(b) and (c), respectively], confirming the spin diffusion with the y -axis components in

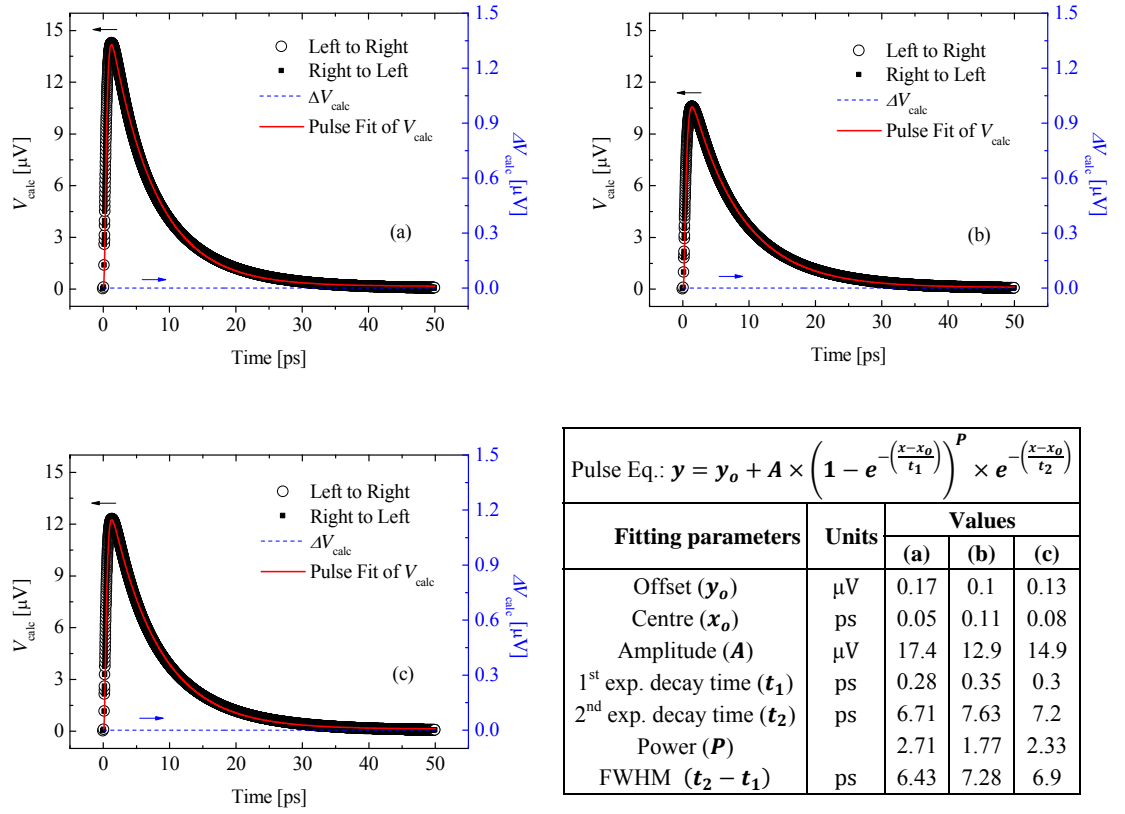


Figure 3.5: Time dependences of voltages (V_{calc}) calculated at the detector position for the (a) straight nanowire and nanowires with the (b) squares and (c) equilateral triangles after the pulsed current injection from left to right and right to left. The solid lines are the fits as detailed in the table. The differences between the two current directions are also shown as ΔV_{calc} .

the additional shapes. A similar work has been done by Kaltenborn *et al.* [92] in the context of time-dependent behaviour of a charge wave in an infinitely thick Gold straight wire after introducing ultra-fast spin-polarised electrons at the left boundary of the Gold wire. However in their work, they have considered a generalised spin-wave diffusion equation in one dimension instead of 2D spin-diffusion equation as discussed above.

3.6.2 Asymmetrical shapes

In this section, the influence of the asymmetric geometries on the non-local signals was studied. Simulations were carried out for the obtuse- and right-angle triangular shapes with unequal sides as shown in Figs. 3.2(e) and (f), respectively. Here, similar to the symmetric calculations, two separate time-dependent processes, one for up-spin electrons flowing from left to right and another for down-spin electrons flowing from right to left, were performed. The corresponding pictures of these processes at $t = 1$ ps were shown in Figs. 3.6(a) and (b) for the obtuse- and right-angle triangular shapes, respectively. From these results, the difference in their potentials ($\Delta V_{\text{calc}} = V_{\text{LR}} - V_{\text{RL}}$) were calculated by subtracting the potential of the down-spin electrons (V_{RL}) from that of the up-spins (V_{LR}) at each time step dt . Plots of ΔV_{calc} against time (t) revealed the geometrical effect on spin-dependent diffusive transport (see Fig. 3.7 for example), suggesting the realisation of the spin-current amplification in the device.

The second objective was to optimise the geometrical shapes and the number of the wing pairs, *i.e.*, one- and two-pair triangular wings ($n = 1$ and 2 , respectively). The first set of simulations was carried out for $n = 1$ with different values of h and b . These results were shown in Figs. 3.7 and 3.8 for the obtuse- and right-angle triangles, respectively.

In Figs. 3.7 and 3.8, the curves indicate the difference between the time evolutions of the up- and down-spin electron potentials taken simultaneously at the points C1 and C2 in Fig. 3.6. It is important to mention that the existence of the peak can be attributed to the fact that the device geometry has a significant influence on the diffusion process of the electron flow. The change in cross-section area at the edges of the triangles, at which the electron flow starts to disperse, is a key to explain these peaks. When the electron flow from left to right arrives at the left edge of the triangles, a new diffusion rate along the y -axis is developed due to the sudden increase in the cross section area. The electrons flown into

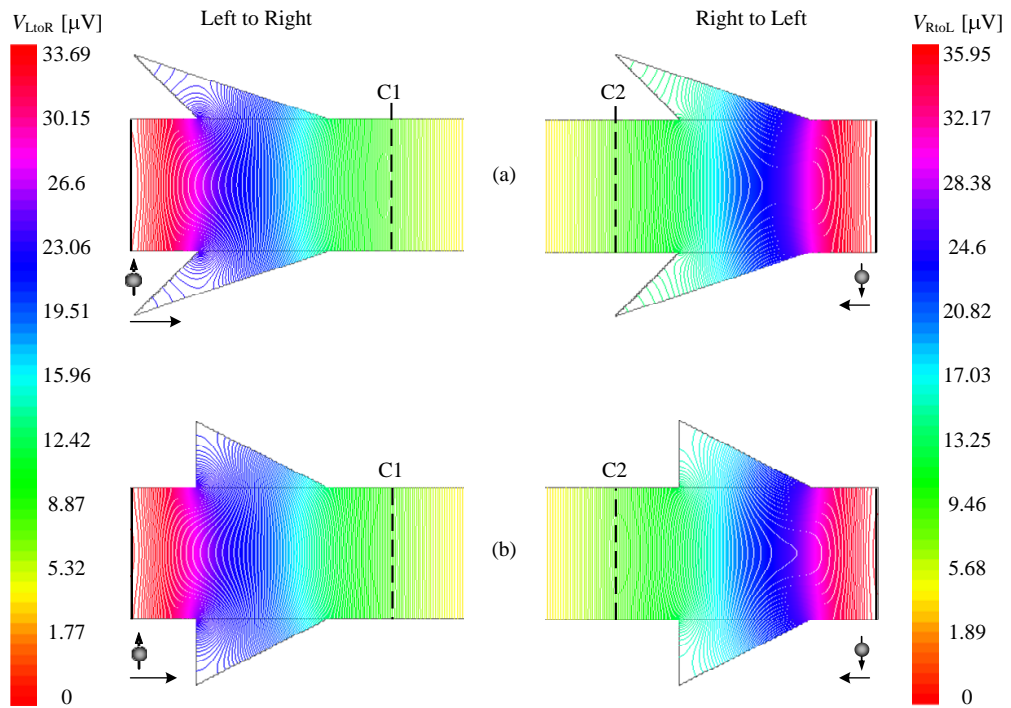


Figure 3.6: Snapshots of the electron distributions at $t = 1$ ps for the electrons flowing from left to right and right to left with the (a) obtuse- and (b) right-angle triangular shapes.

this area tend to diffuse along the y -axis faster than those flown into the right edge of the triangles from right to left in Fig. 3.6. As a result, the diffusion rates for the two opposite spin flow become different and the corresponding electron distributions become different. Even larger difference will be induced at the end edges of the triangles as described below.

Phenomenologically in such geometries as depicted in Fig. 3.6, the up-spin electrons flowing from left to right experience very small resistance from the triangular wings as the up-spin electrons are gradually dispersed into the wings and are gradually returned to the straight wire by flowing along the hypotenuse. On the other hand, the down-spin electrons flowing in the opposite direction suffer from larger resistance as these electrons are gradually dispersed into the wings but they see sudden decrease in the width of the wings at their edges. Hence the potentials induced by these independent electron currents

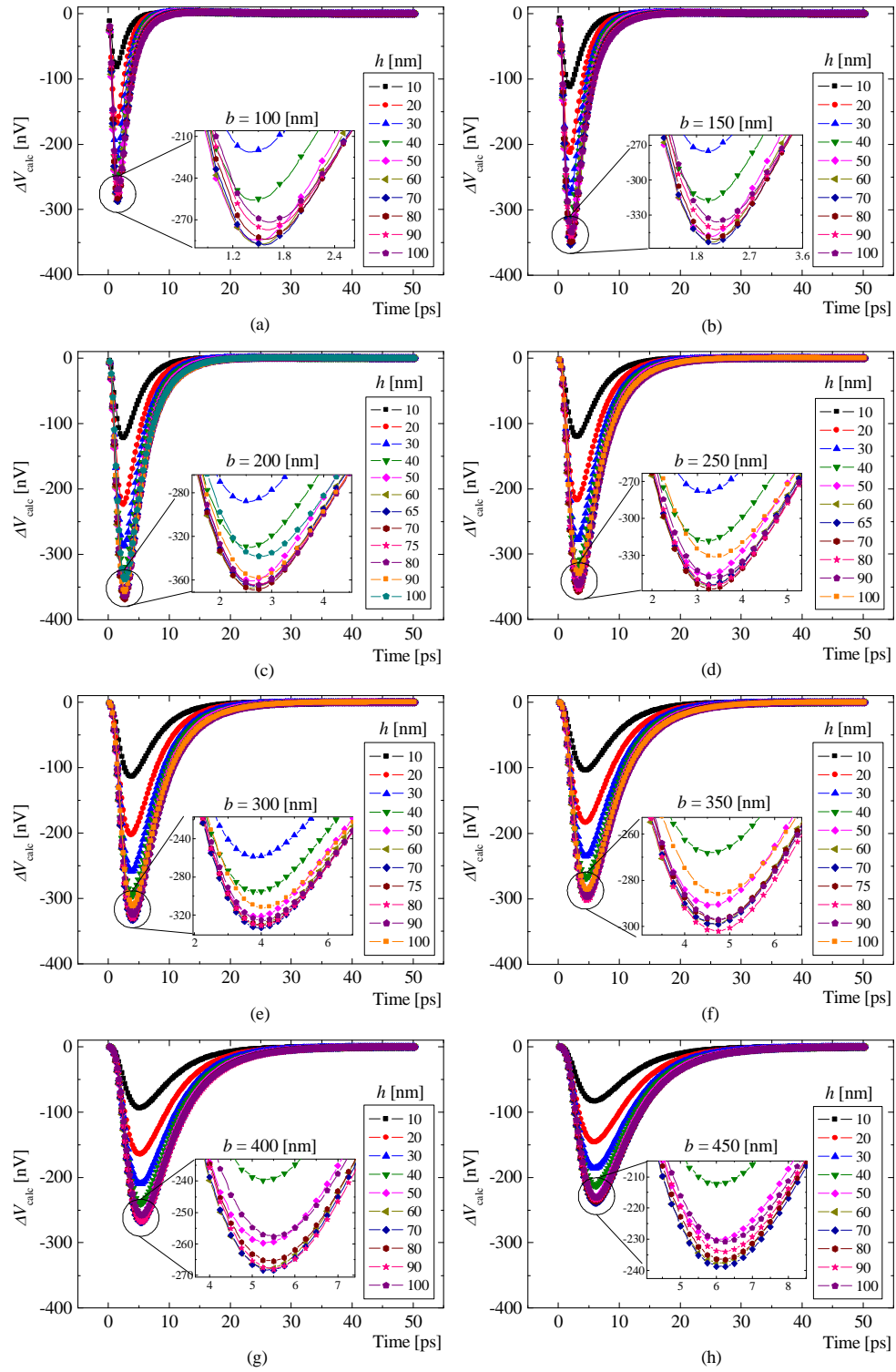


Figure 3.7: Comparison of the time-dependent potential differences ΔV_{calc} for the obtuse-angle triangular wings with different geometrical parameters: $b =$ (a) 100 nm, (b) 150 nm, (c) 200 nm, (d) 250 nm, (e) 300 nm, (f) 350 nm, (g) 400 nm and (h) 450 nm with $10 \leq h \leq 100$ nm. The insets are the magnified views of the peaks.

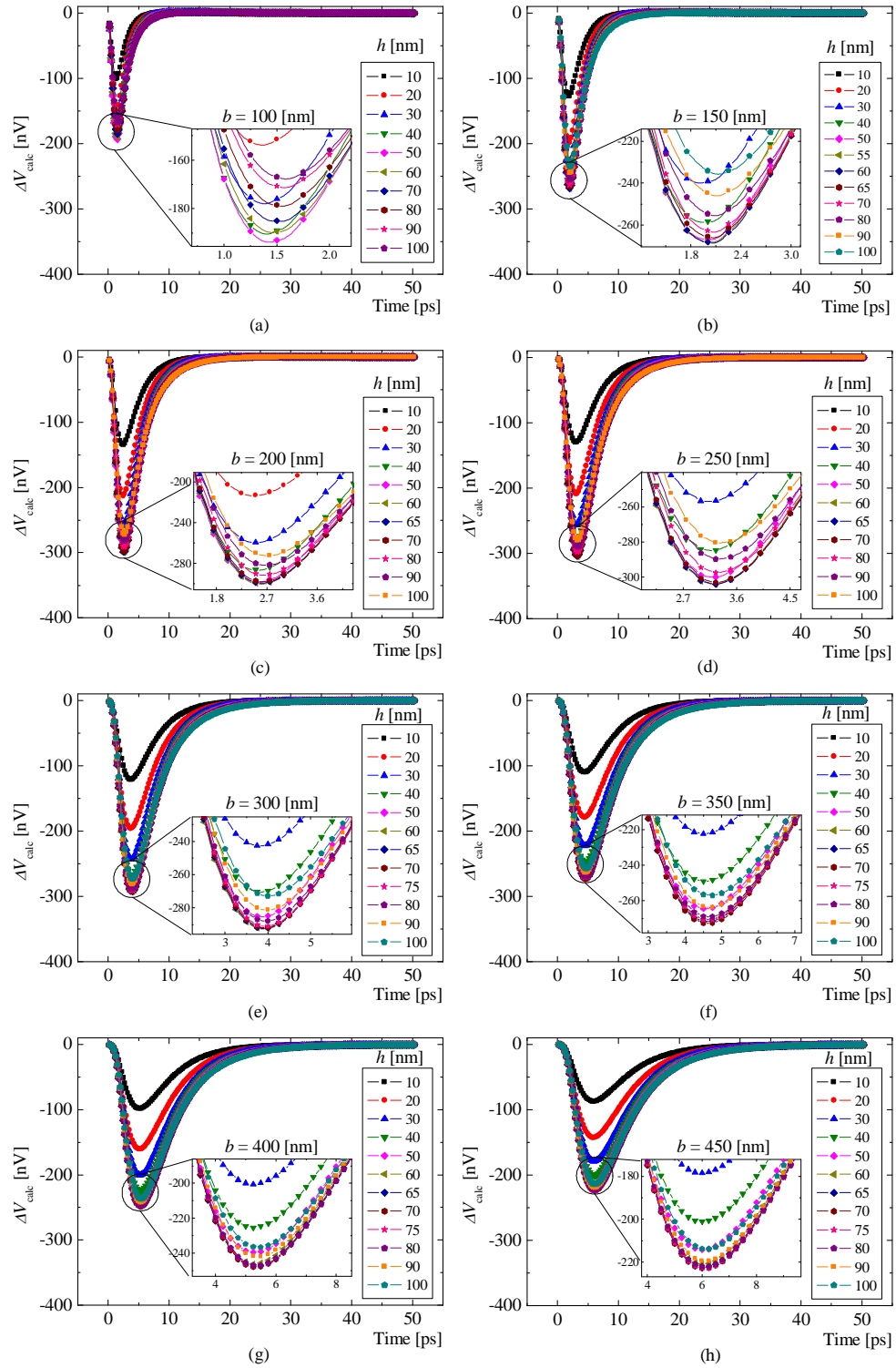


Figure 3.8: Comparison of the time-dependent potential differences ΔV_{calc} for the right-angle triangular wings with different geometrical parameters: $b =$ (a) 100 nm, (b) 150 nm, (c) 200 nm, (d) 250 nm, (e) 300 nm, (f) 350 nm, (g) 400 nm and (h) 450 nm with $10 \leq h \leq 100$ nm. The insets are the magnified views of the peaks.

become different, *i.e.*, $V_{LR}|_{x=l} \neq V_{RL}|_{x=l}$. This suggests the conventional non-local configuration may be locally broken with inducing a local spin-polarised current.

It should also be noted that the curves in Figs. 3.7 and 3.8 peak at different times for different triangle base lengths b . For the larger values of b the peak positions are shifted toward the higher t values. This is expected since the electron packet takes longer time to travel a longer effective path. The peak values of the electron density also depend on the height h of the triangle wings. For a constant value of b , an optimised h values can hence be identified.

Now the dimension of the asymmetric triangles need to be optimised to maximise the spin-current amplification. In order to optimise b and h , the values of b are plotted which show the maximum ΔV_{calc} with a series of h for the obtuse- and right-angle triangles, as summarised in Figs 3.9(a) and (b), respectively. From these curves, the largest ΔV_{calc} can be found at $h = 70$ and 65 nm for the obtuse- and right-angle triangles, respectively.

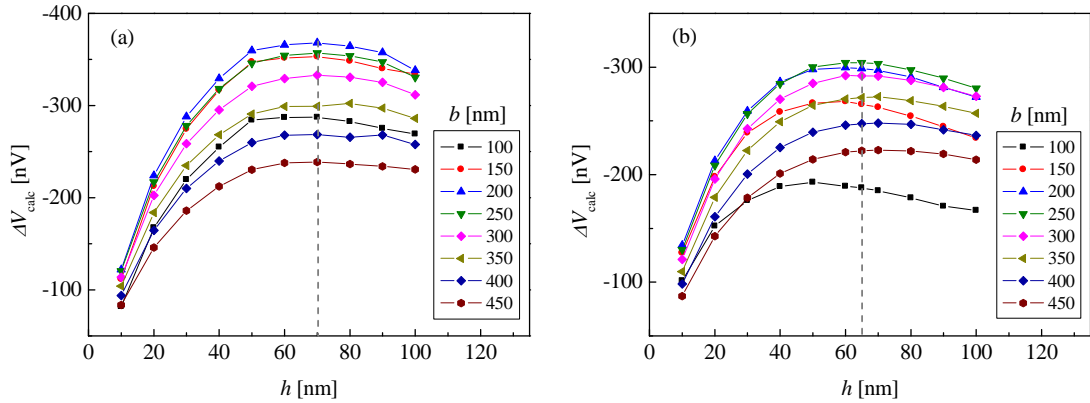


Figure 3.9: Corresponding peak values of ΔV_{calc} with different h for (a) obtuse- and (b) right-angle triangular wings.

Figure 3.10(a) shows the peak values of ΔV_{calc} for the different values of b for the obtuse- and right-angle triangles with their optimised heights. This indicates that the maximum amplification ΔV_{calc} can be achieved at $b = 200$ nm and 250 nm for the obtuse- and right-angle triangles, respectively. These optimum

conditions give ΔV_{calc} to be -368 nV and -305 nV for the obtuse- and right-angle triangles, respectively. Figure 3.10(b) shows the optimised combinations of b and h values where the signal peaks.

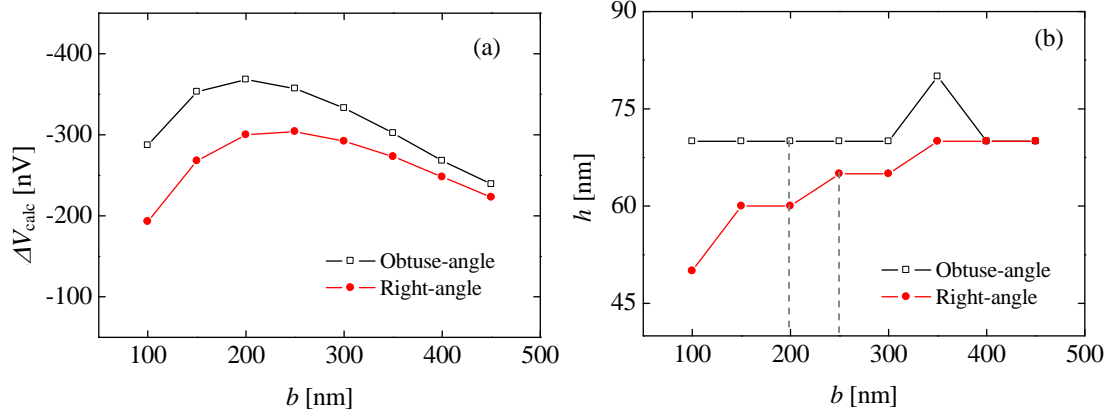


Figure 3.10: (a) Corresponding peak values of ΔV_{calc} with different b for both obtuse- and right-angle triangles. (b) Calculated relationship between h and b values to maximise ΔV_{calc} .

However, it is also important to mention that the increase in the difference (ΔV_{calc}) is usually compensated by the increase in the effective current path induced by the increase in b [see Figs. 3.2(e) and (f)]. This eventually leads to the reduction of the actual spin-current signals in the NM channel (above the spin diffusion length) dramatically due to the spin-flip scattering [63] and makes the LSV signals difficult to be detected. Thus in order to achieve the maximum amplification of the spin-current signals in the NLSV measurements, a combination of a short NM channel and an optimum triangular wing geometry is required. Hence, an obtuse-angle triangular shape ($b = 200$ nm and $h = 70$ nm) and a right-angle triangular shape ($b = 250$ nm and $h = 65$ nm) can be defined as the optimum condition. Even so, in this thesis, due to the fabrication challenges (see Section 4.2), only right-angle triangular shapes with $b = 100$ nm and different $0 \leq h \leq 60$ nm have been investigated experimentally. The corresponding results are presented in Chapter 7.

The influence of the number of pairs of triangle wings is also investigated for $n = 2$ as shown in Figs. 3.11 and 3.12. It can be seen that the peak values of ΔV_{calc} for the same values of h and b are decreased by 30-40% with increasing the number of triangle wings. This is due to the fact that the additional pair of the triangular wings has increased the effective current paths for the electrons. The additional geometry may also induce a destructive interference effect on ΔV_{calc} . For the same wire length (l) and channel-area, such an effect can be seen by comparing the results presented in Figs. 3.7 and 3.11 (Figs. 3.8 and 3.12) for the obtuse- (right-)angle triangles for $n = 1$ and 2, respectively. For instance, the peak value ΔV_{calc} is calculated to be -178.5 nV for the single-paired right-angle triangles with $h = 80$ nm and $b = 100$ nm as shown in Fig. 3.8(a). This is approximately four times larger than ΔV_{calc} (-47.4 nV) obtained for the two-pair right-angle triangles with equal area and wire-length, *i.e.*, $h = 80$ nm and $b = 50$ nm, as shown in Fig. 3.12(a). Therefore, only $n = 1$ cases are investigated experimentally in this study.

3.7 Steady-state diffusion equation

Since the experimental measurements were performed with a DC current, the steady-state of the electrons injected in the opposite directions were also calculated. In the steady state ($t = \infty$), $\mu_s(x, y, t)$ became time-independent and hence Equation 3.4.1 could be rewritten as

$$D\Delta\mu_s(x, y) = \frac{\mu_s(x, y)}{\tau} \quad (\text{on } \Omega). \quad (3.7.1)$$

Here, the boundary conditions for $\mu_s(x, y)$ were given by Eq. 3.4.3 together with the Dirichlet condition:

$$\mu_s(x, y) |_{x=0} = \mu_o, \quad (3.7.2)$$

where μ_o is the electron density injected at the Py/Cu interface at $t = 0$.

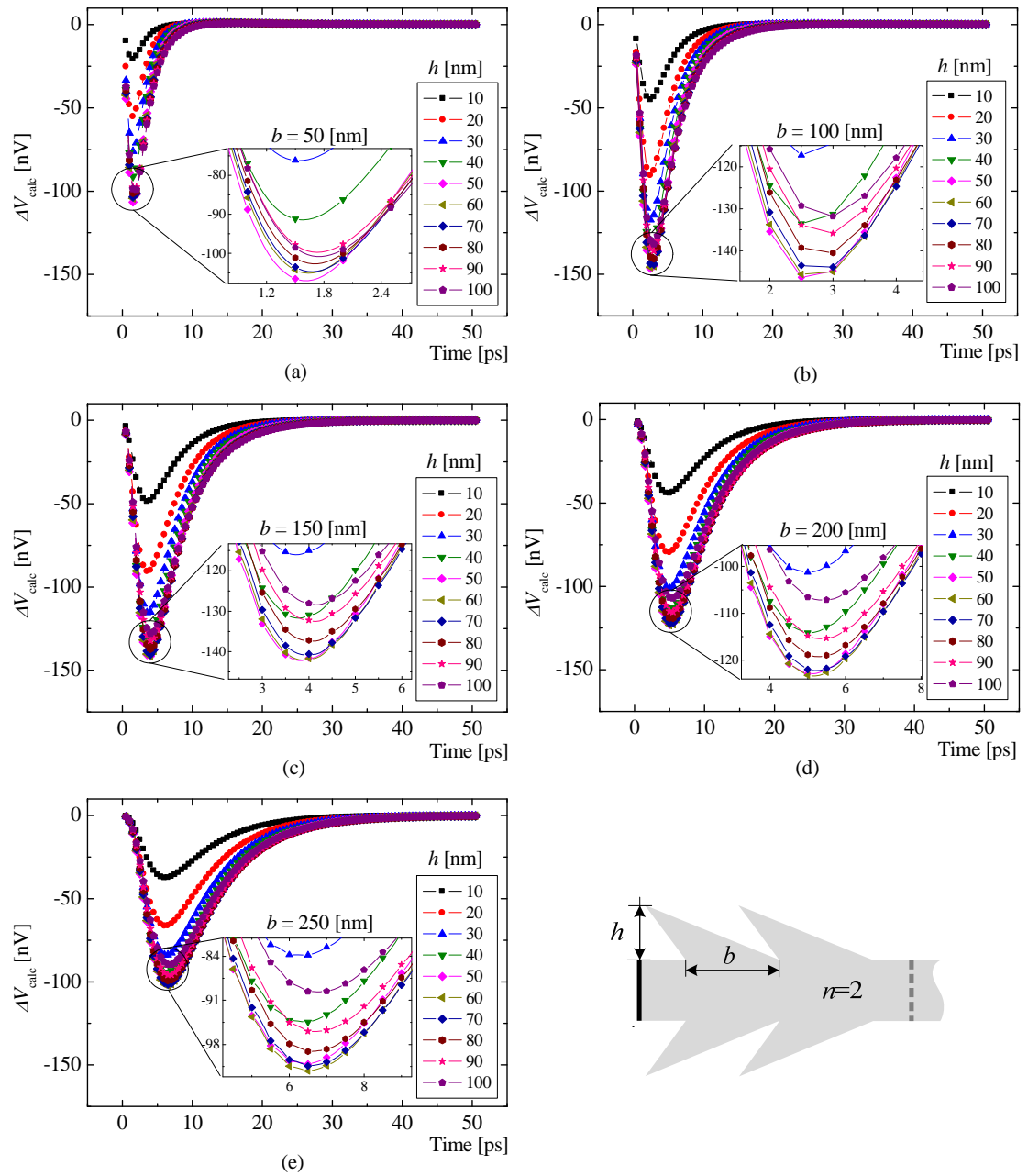


Figure 3.11: Comparison of the time-dependent potential differences ΔV_{calc} for the two-paired obtuse-angle triangular wings with different geometrical parameters: $b =$ (a) 50 nm, (b) 100 nm, (c) 150 nm, (d) 200 nm and (e) 250 nm with $10 \leq h \leq 100$ nm. The insets are the magnified views of the peaks. A schematic diagram of the structure is also shown.

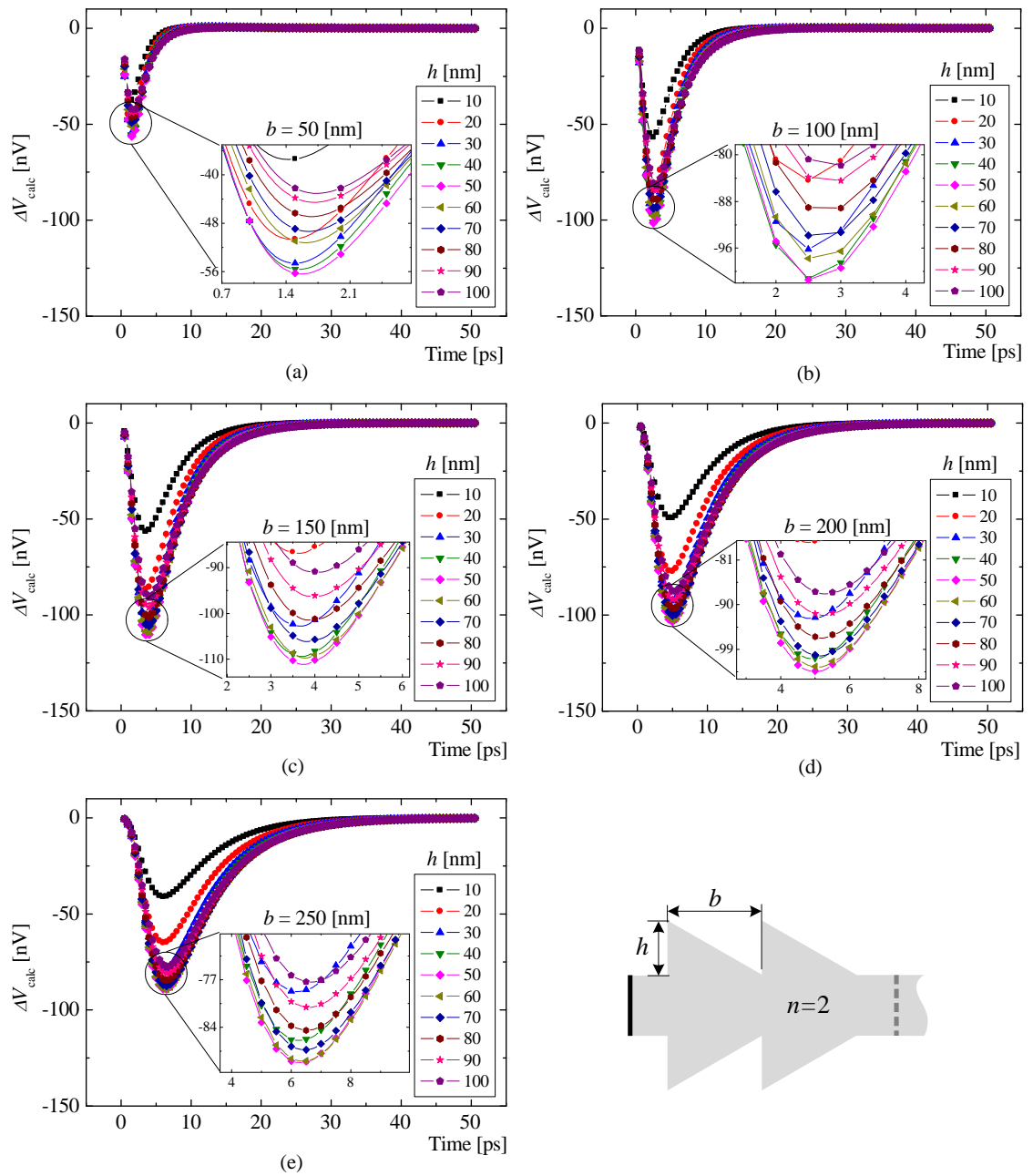


Figure 3.12: Comparison of the time-dependent potential differences ΔV_{calc} for the two-paired right-angle triangular wings with different geometrical parameters: $b =$ (a) 50 nm, (b) 100 nm, (c) 150 nm, (d) 200 nm and (e) 250 nm with $10 \leq h \leq 100$ nm. The insets are the magnified views of the peaks. A schematic diagram of the structure is also shown.

Figures 3.13(a)-(f) show the steady-state electron distributions at $t = \infty$ for the LSVs with the right-angle triangular shapes ($b = 100$ nm and $0 \leq h \leq 100$ nm). These images clearly indicate that the electron distributions due to the geometrical triangular wings still exist in the steady state. From the contour plots, which are the representative spacial distributions of the electrochemical potentials, it is apparent that the potential distributions are not uniform along the y -axis near the triangular regions, which is similar to those induced by a pulsed current as shown in Fig. 3.6. Such non-uniform distributions yield different diffusion processes for the up- and down-spins as phenomenologically explained in Section 3.6.2. Therefore, these devices have been fabricated and characterised in their steady states as described in the following chapter 7.

In order to define the steady state in spin diffusion processes, the above condition 3.7.2 was substituted to Eq. 3.4.1. The corresponding time-dependent ΔV_{calc} was plotted in Fig. 3.13(g) for the case of a LSV with the right-angle triangular shapes ($b = 100$ nm and $h = 50$ nm). As similar to the above steady state the non-zero ΔV_{calc} was obtained at $t = 56.8$ ps after the pulsed current introduction. ΔV_{calc} was found to be $13.89 \mu\text{V}$, which is the same with the above steady-state results. Hence, the steady state was found to be achieved above 56.8 ps after the current injection.

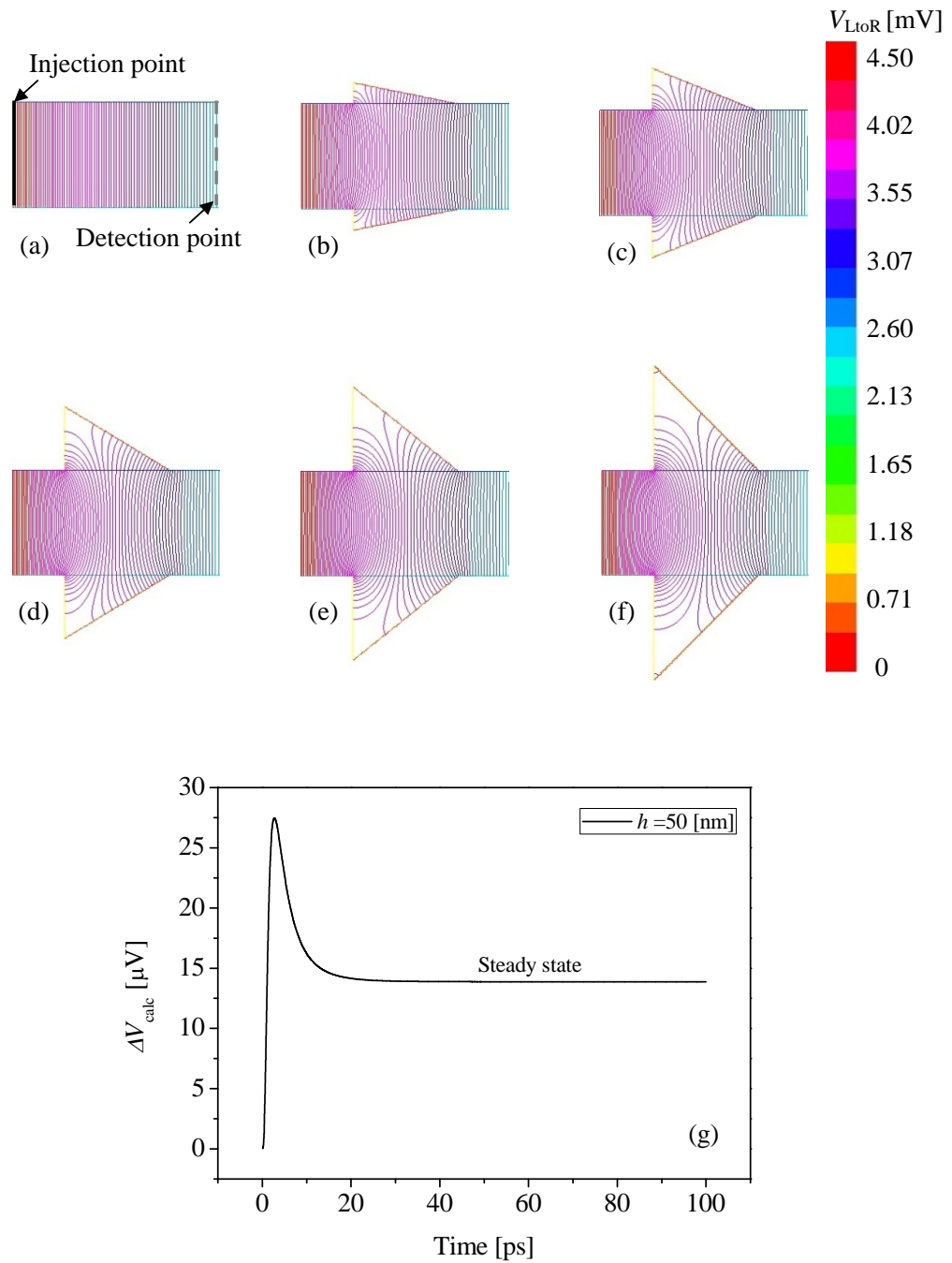


Figure 3.13: Electron distributions in their steady-states calculated for an electrical current injected from left to right with triangular shapes ($b = 100$ nm): $h =$ (a) 0, (b) 20, (c) 40, (d) 60, (e) 80 and (f) 100 nm. (g) Time-dependence of ΔV_{calc} for the right-angle triangle ($b = 100$ nm and $h = 50$ nm) showing the steady state.

Chapter 4

Device Fabrication

This chapter describes the equipment and techniques used for the fabrication of devices. The designs of nanoscale devices are also presented. The flow charts of the fabrication steps are detailed, including wafer cleaning, spin coating, lithography, development, metallisation, lift-off and wire bonding.

4.1 Introduction

The discovery of several new physical phenomena in the field of spintronics is a direct result of recent developments in nanofabrication techniques. One of the main driving factors has been the development of electron-beam lithography (EBL) which uses a focused high energy electron beam (EB) to fabricate high-resolution patterns on a polymer resist coated on a substrate wafer. E-beam lithography can define patterns with features below 10 nm [93]. Such high resolution allows the fabrication of nanoscale devices with dimensions much smaller than the critical length scale in studying spin-dependent electron transport in metals. For spin injection into non-magnetic materials, the critical length

scale is the spin diffusion length λ_s , ranging from 100 to 1200 nm at room temperature (RT) depending on the material [16,56,81,94–98].

E-beam lithography is not suitable for large scale production because of its limited throughput and high cost. In this context, optical lithography such as ultraviolet (UV) photolithography is the most common technique in defining larger patterns. However, the resolution is limited by the wavelength of the light and the optical diffraction effect. Typically the range of light wavelengths used in current photolithography is between 200 to 450 nm [99]. This range provides for the device features below 50 nm in industry [100].

4.2 Device designs

Before settling the final design of LSV devices for spin-current amplification, two sets of preliminary devices were designed and fabricated. The first set was a ladder shaped device, consisting of five identical nanowires at equidistant in parallel. These were connected to each other via a so-called bridging wire placed perpendicular to them [see Fig. 4.1(a)]. This device was employed to measure the electrical properties of the materials to be used in the LSV devices as described in Section 6.1. The second set was a conventional LSV structure with a straight non-magnetic wire as shown in Fig. 4.1(b). This set was used to measure non-local LSV signals as discussed in Section 6.3.

The effect of non-magnetic nanowire geometry on the LSV signal amplification was then investigated as discussed in Chapter 7. Numerical simulations revealed that the obtuse-angle triangles were predicted to give the largest spin-current amplification. However, due to practical fabrication challenges, the edges of the triangular wings cannot be determined as clearly as those in theoretical models. Therefore to reduce this uncertainty only a pair of right-angle triangles were fabricated and measured. Figure 4.2 shows the detail of the LSV

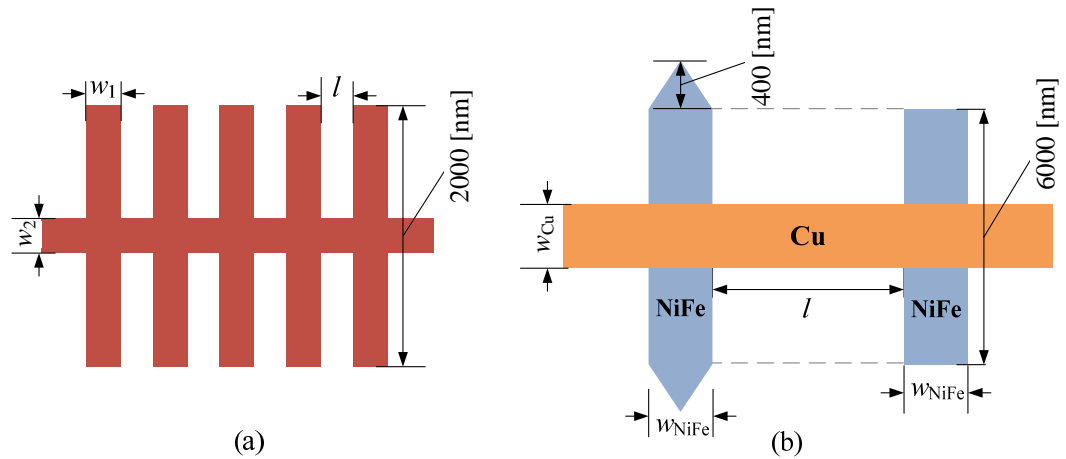


Figure 4.1: Schematic diagrams of (a) a ladder device consisting of five parallel nanowires with equal separations connected through an orthogonal bridging wire and (b) a conventional LSV device with a straight bridging wire.

device with a pair of right-angle triangles with their height $0 \leq h \leq 60$ nm and base $b = 100$ nm. The pair of triangular wings were located 50 nm away from the two Py wires, maintaining the channel length l to be 200 nm. The width of the Cu and Py wires were designed to be 100 nm and 200 nm, respectively.

These devices were fabricated with different dimensions on 16 mm square thermally oxidised Silicon substrates as listed in Table 4.1. Each substrate contained 9 chips and each chip held 3 LSV devices. Each chip had up to 20 external electrical contacts as shown in Fig. 4.3. In total there were 27 LSV devices on a substrate.

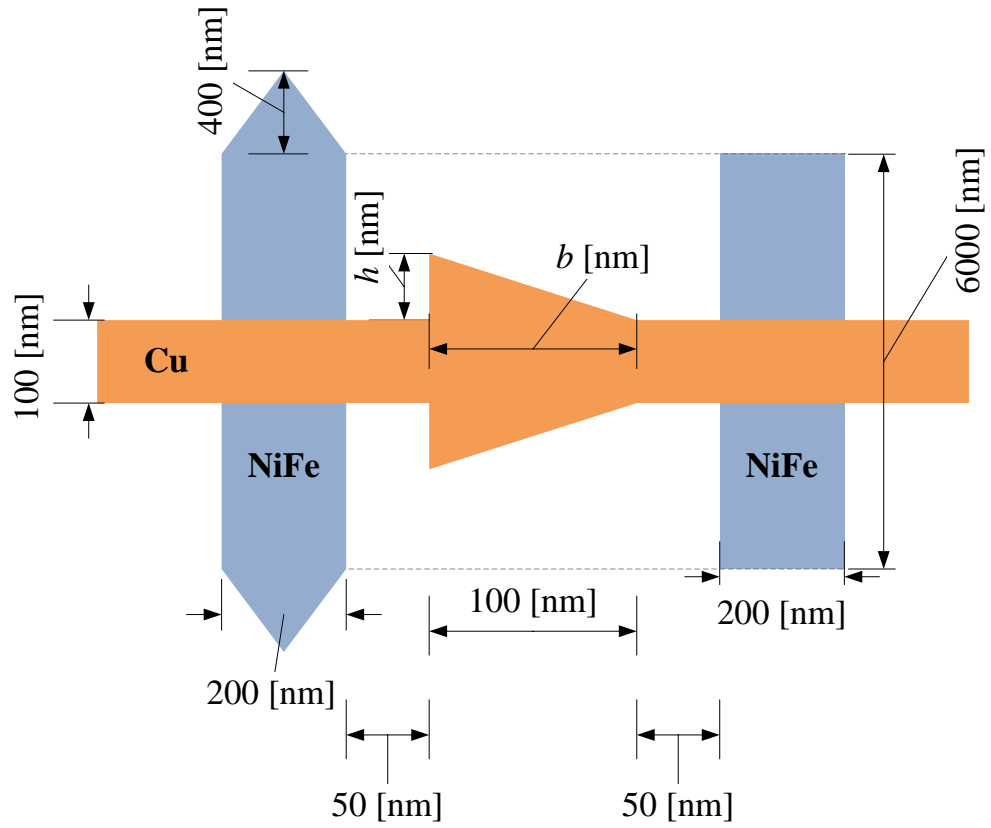


Figure 4.2: Schematic diagram of the LSV with the triangles.

Table 4.1: Dimensions of the devices fabricated.

Ladder		LSV with a straight wire		LSV with triangles
w [nm]	l [nm]	w [nm]	l [nm]	h [nm]
100	200	100	100, 200	20
500	200	200	300, 400	40
100	500	200	500 & 600	50
500	500	500	300	60
		500	400	
		500	500	

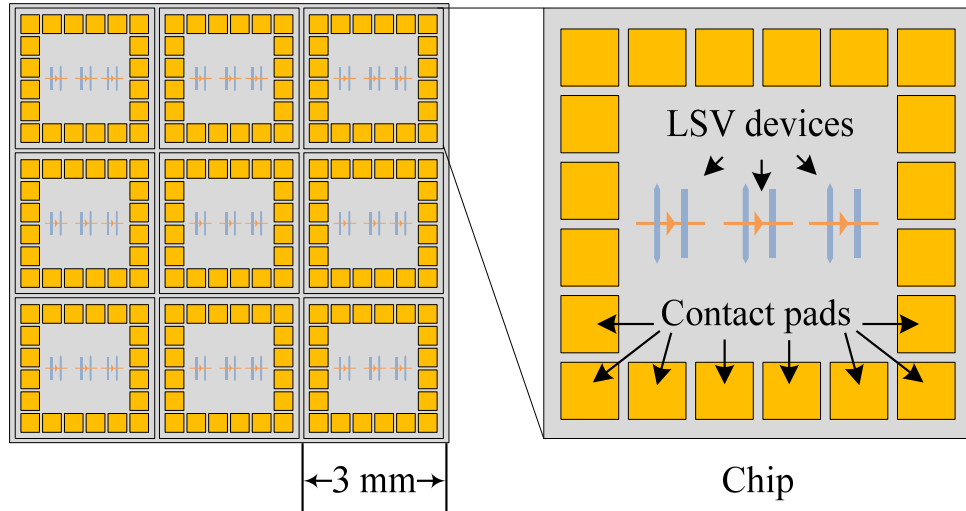


Figure 4.3: Device layout on the 16 mm square substrate containing 9 chips.

To evaluate dimension distributions in the fabricated devices and understand the possible origins of the distributions, the dimensions of the devices were measured by analysing SEM images using image processing tools in Microsoft office Visio [101]. In the analysed image, each pixel represented a unique length, depending on their image resolution. The width (w) and length (l) of the devices were calculated by counting the pixels. Based on the measured values on the SEM images with the magnification of $100\text{-}200 \times 10^3$, the standard deviations (σ_{sd}) of w and l were calculated to be <3.5 nm and <5.5 nm, respectively. It should be noted that σ_{sd} for l was almost twice the value of σ_{sd} for w . This can be attributed to the summation of σ_{sd} for the two parallel wire widths (w), between which determined the edge to edge distance (l).

4.3 Fabrication processes

As discussed in the previous section the dimensions of the devices are in the nanometric range. This requires the use of EBL for patterning. In order to make electrical contacts onto the devices using wire bonding, they need reasonably sized contact pads (typically $500 \mu\text{m} \times 500 \mu\text{m}$). The fabrication processes are

divided into multiple lift-off processes with EBL for inner LSV nanostructures and photolithography for outer contact pads.

4.3.1 LSV devices

E-beam lithography procedures

The typical EBL procedures used in this study are shown in Fig. 4.4.

- 1st step : Spin coating of resist
- 2nd step : EBL exposure (first layer)
- 3rd step : Resist development
- 4th step : Metallisation
- 5th step : Lift-off
- 6th - 10th steps : Repeating the 1st to 5th steps for the second layer

4.3.1.1 Spin coating of resist

Most of the resists used in EBL are electron-sensitive materials consisting of hydrocarbon-based polymers. They are classified into two groups based on their interactions with the EB exposure: positive and negative resist (see Fig. 4.5). For the positive resist the interactions of the polymer with the EB causes the molecular chains to break forming lower molecular weight molecules. This allows the exposed area to be dissolved in solvent used for the development, whereas the unexposed regions are not dissolved. For the negative resist the opposite scenario occurs. The interactions between the resist and the EB causes

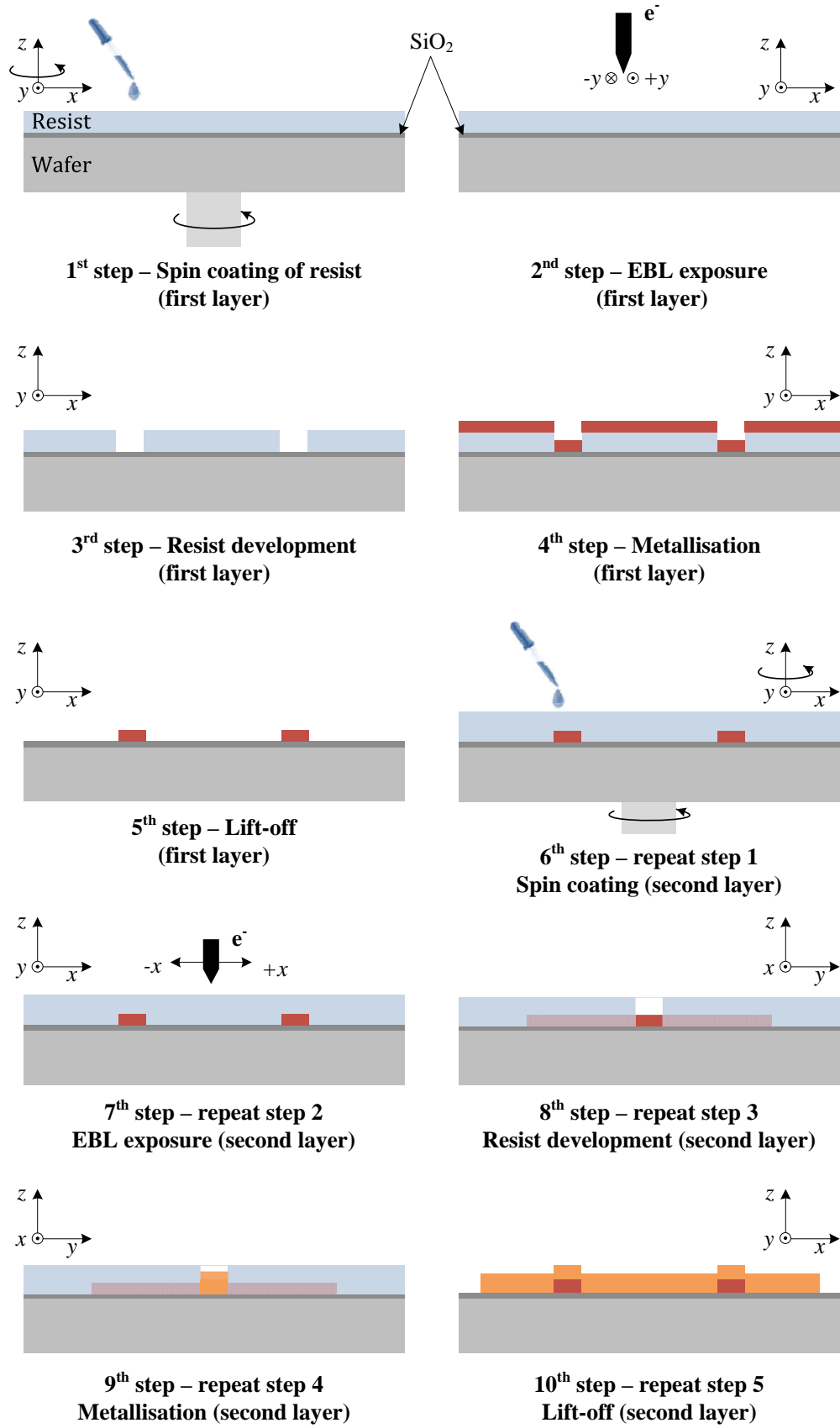


Figure 4.4: Schematic diagrams of the EBL patterning processes.

cross-linking of the polymer chains which makes them have higher molecular weight. Hence the exposed area is not dissolved when developed [102].

In this study, high resolution positive EB resist (Zeon, ZEP520A) was used in its diluted form by anisole at a ratio of 1:1. ZEP520A has higher sensitivity than conventional resists, such as polymethyl methacrylate (PMMA) [103].

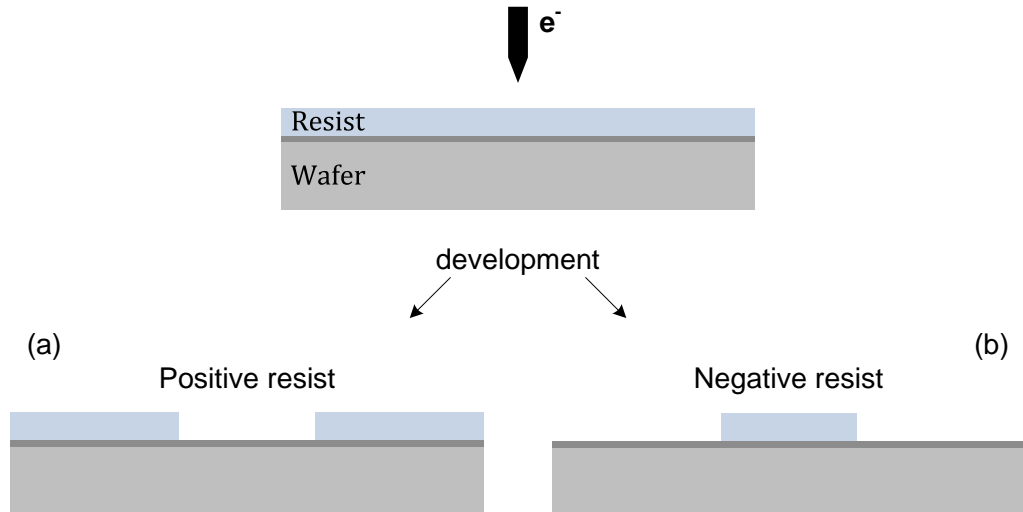


Figure 4.5: Schematic diagrams of the EBL exposure onto two types of resist layers: (a) For the positive resist the exposed area becomes soluble upon the development. (b) The negative resist exhibits the opposite effect.

Before the process of resist coating, a 16 mm square silicon substrate with a 300 nm thick SiO_2 layer on the surface was cleaned in acetone using an ultrasonic bath for about 5 min. Subsequently the substrate was cleaned in isopropanol (IPA) in an ultrasonic bath for 1 min. The substrate was then placed on a 180 °C hotplate for about 2 min. in order to evaporate the remained solvents.

The cleaned substrate was then coated with the ZEP520A resist by spin coating at 4000 rpm for 40 s. This process provided an approximately 140 nm thick resist layer. The resist was pre-baked at 180 °C for 2 min. to ensure the evaporation of the remaining solvent in the resist and to improve the adhesion of the resist to the substrate [104].

4.3.1.2 EBL exposure (first layer)

The EBL processes in this work was developed at the Manufacturing and Research Facility in the University of Leeds. The e-beam system (JEOL, JBX-6300FS) as shown in Fig. 4.6 was used. The system was controlled by Nanometer Pattern Generation System (NPGS) software during the writing of the patterns giving a resolution of $<2\text{ nm}$ and a stitching accuracy of $<\pm 7\text{ nm}$. For the first layer, which patterned the two ferromagnetic wires, the EB parameters were set through the NPGS software. An EB with 100 keV acceleration energy, 10 nm spot size and 400 pA emission current was used to expose to the resist. Once the EB exposure was completed, the substrate was unloaded.



Figure 4.6: Photograph of the JEOL JBX-6300FS EBL system at the University of Leeds [105].

4.3.1.3 Resist development

After the e-beam exposure, the substrate was dipped in the developer solution for 50 s in order to remove the exposed area with leaving the unexposed resist behind. The development solution used was ZED-N50. The development time was critical to achieve the precise patterning as designed. If the development time was too short, the pattern appeared to be underdeveloped leading to residual resist in the exposed area. On the other hand in the case of excessive development time, the pattern appeared to be overdeveloped causing larger and rounded features than those designed. The above condition was optimised by Dr A. J. Vick.

4.3.1.4 Metallisation

After the development, permalloy ($\text{Py} = \text{Ni}_{81}\text{Fe}_{19}$) was deposited onto the patterned substrate using an e-beam evaporator (Leybold, UNIVEX 350). The evaporator consisted of eight separate sources, allowing the deposition of different metals without breaking a vacuum. The base pressure was around 2.5×10^{-5} Pa and that during the evaporation was 5×10^{-5} Pa.

4.3.1.5 Lift-off

After the metallisation the substrate was placed in cyclopentanone for 60 min., followed by 5 s in an ultrasonic bath to remove the remaining polymer completely. It was then flushed in cold IPA and dried. This process provided Py electrodes for spin injection and detection, *i.e.*, two 30 nm thick and 200 nm wide Py wires with different shapes at their ends. One wire was designed with square ends and another was with sharp ends to assist domain nucleation for reversal at a lower magnetic field as shown in Fig. 4.7 [106].

4.3.1.6 Second layer patterning

The second layer was patterned to form a Cu nanowire. The above steps 4.3.1.1 to 4.3.1.3 were repeated to complete the second EBL patterned layer. Prior to the Cu metallisation (step 4.3.1.4) the surface of the two Py wires were cleaned by oxygen ashing to create an Ohmic and transparent Py/Cu junctions. These junctions were necessary to inject a spin-polarised current with high efficiency [16, 107]. The thickness and width of the Cu nanowires were designed to be 70 nm and 100 nm, respectively. Triangular wings were attached to the Cu nanowires with fixed base lengths of 100 nm and height between 0 and 60 nm. These wings were located 50 nm away from the edges of the Py/Cu junctions. After the lift-off as described in Section 4.3.1.5 the LSV devices consisting of Ni₈₁Fe₁₉ electrodes and the Cu wire were observed by SEM as shown in Fig. 4.7.

The brightness of the SEM image is primarily due to the topography of the deposited layer surfaces. The top layer, which is the highest above the sample stage, is the Cu wire deposited uniformly on both Py wires. From the magnified image, the triangular wings have a small offset and asymmetry in their locations and shapes. There are two different reasons for the offset: (1) Overlay alignment ($< \pm 7$ nm) between the two e-beam steps causes a lateral shift in the device features. (2) With non-rectangular shapes it is usually very difficult to get the correct e-beam dose for every part of that shape. The e-beam vector line scan sometime affects the resist in the neighbouring area, which may overdose the resist. Consequently distributions in the dimensions occurs at the edges of the triangular wings. As can be seen in Fig. 4.7, the base b is measured to be 92 nm and 104 nm for the right and left triangular wings, respectively.

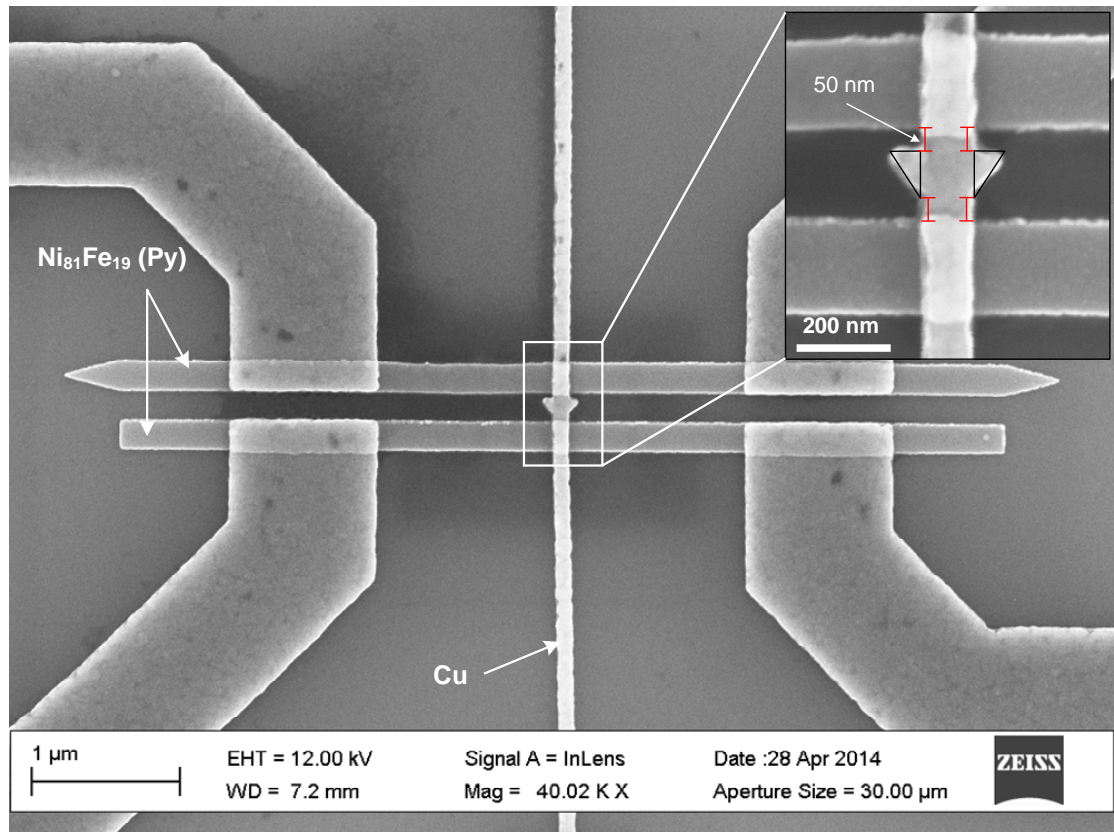


Figure 4.7: SEM image of the LSV with the triangles after the second EBL process. Inset is the magnified image of the LSV device with designed triangular dimensions. (Courtesy of Dr. A. J. Vick).

4.3.2 External electrical contacts

4.3.2.1 Photolithography

In the second stage of the fabrication the contact pads were patterned using photolithography. This was carried out using an EGV Mask Aligner at the University of Leeds. The photolithography transferred a geometric pattern from a photomask to a photosensitive resist layer on the substrate by exposure with ultraviolet (UV) light [108]. The photomask was made of a thin quartz glass plate with a reflective Chromium coating and contained 27 structures with 20 contact pads for each structure and alignment marks for overlay exposure. The masks were designed using L-Edit [109] as shown in Fig. 4.8.

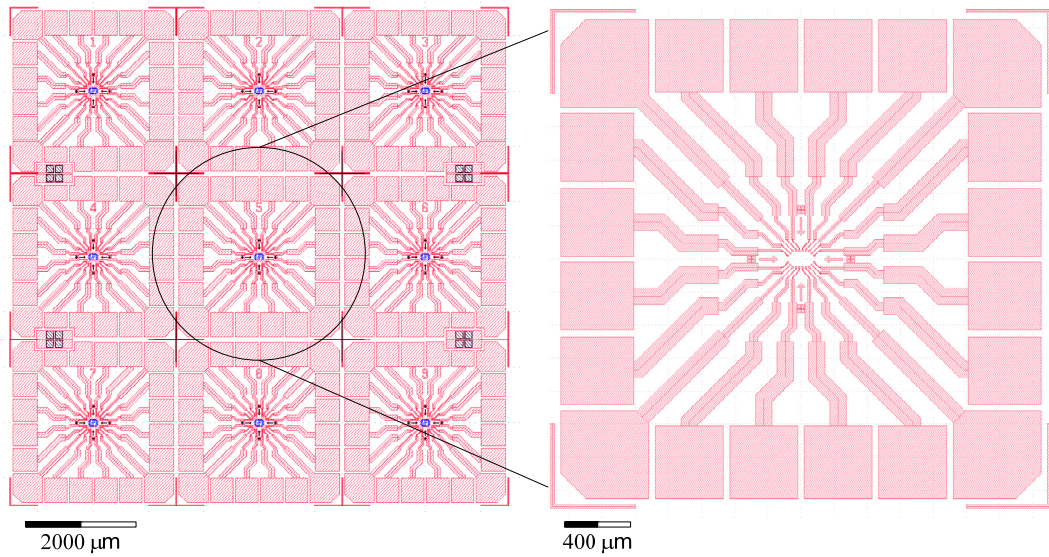


Figure 4.8: Schematic mask design drawn by L-Edit (Courtesy of Dr. A. J. Vick).

After the second EBL lift-off process, S1813 positive photoresist was spin-coated using a SUSS spin coater. Typical spin coating parameters were 4000 rpm for 40 s. This gave a resist thickness of approximately 1300 nm as indicated by the manufacturer's data sheet, which was baked at 110 °C for 3 min. The substrate was then exposed for 2.8 s to UV light with wavelength of 365 nm and intensity of 110 mJ cm⁻². The development was subsequently carried out with MF319 developer. The optimal development time was determined to be 110 s.

4.3.2.2 Metallisation

Chromium or Titanium (10 nm thick) and Gold (150 nm thick) layers were deposited onto the substrate using an e-beam evaporator (Leybold, UNIVEX 350). The thin Chromium or Titanium layers were deposited prior to Gold to enhance the adhesion of the Gold layer onto the substrate. The pressure for deposition was similar to the step 4.3.1.4.

After the metallisation the substrate was placed in acetone for 60 min., followed by 5 s in an ultrasonic bath to remove any remaining polymer completely. The lifted-off chip contained 20 contact pads as shown in Fig. 4.9. Finally the

samples were coated with optical resist (LOR3A) to prevent the devices from being oxidised and damaged during dicing.

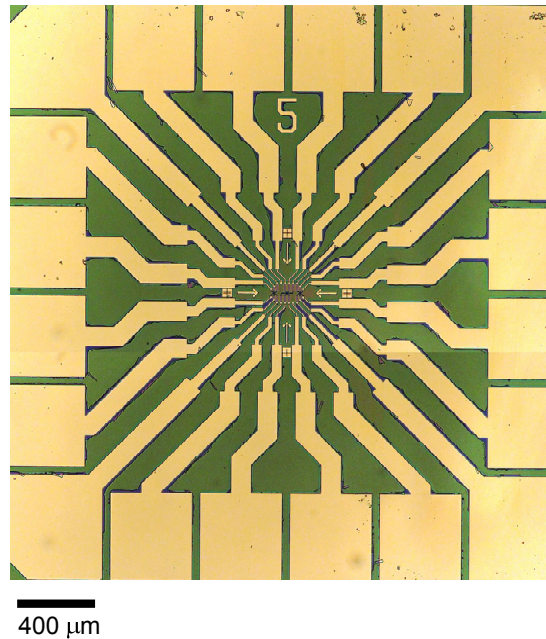


Figure 4.9: Optical microscope image of completed electrical contacts of one chip fabricated by photolithography connected to the LSV device.

4.4 Wire bonding

Wire bonding was used as a reliable means of connecting the electrical contact pads on the chip to the bond pads on a chip carrier. There are three bonding methods that have been developed in the semiconductor industry: thermocompression, thermosonic and ultrasonic methods as listed Table in 4.2 [110, 111]. The thermocompression bonds a Gold wire to the heated surface of the contact pad by pressing with force (typically 40 kN). The thermosonic method uses ultrasonic vibration to bond a wire to a hot pad surface. The ultrasonic method connects a lead wire to the pad surface using both force and vibration simultaneously. Here, several wire materials are available but the most commonly used are Gold (Au) or Aluminium (Al).

Table 4.2: Comparison of wire bonding methods.

Wire bond type	Force	Temperature	Ultrasonic	Wire
Thermocompression	High (~ 40 kN)	300 – 500°C	No	Au
Thermosonic	Low (~ 0.7 N)	100 – 250°C	Yes	Au
Ultrasonic	Low (~ 0.4 N)	25°C	Yes	Al, Au

Furthermore these three methods use two wire bonding techniques; ball-wedge and wedge-wedge bonding [110–112]. The ball-wedge bonding is typically associated with thermocompression and thermosonic bonding methods, where a ball forms after the bonding sequence and assists the first bonding by deforming a ball at lower energy. The second wedge bonding utilises ultrasonic vibration and force to connect the wire and the pad surface without using a ball. The wedge-wedge bonding only uses the wedge process.

In this project the devices were mounted onto a 20-pin chip carrier using Silver paint. A K&S wedge wire bonder (model 4523) was used at the York JEOL Nanocentre. Electrical connections to the samples were made by means of thermosonic wire bonding using 25 μm diameter Au wires. The first bond was done onto the pad on the sample and then the second bond was performed onto the pad on the chip carrier. Figure 4.10 shows an example of a mounted sample after the wire bonding.

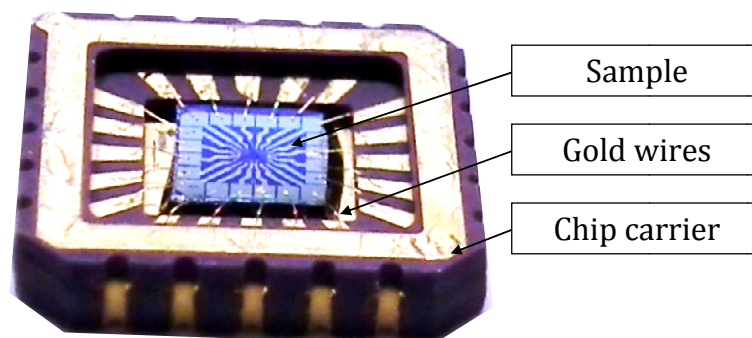


Figure 4.10: Photograph of a mounted sample after wire bonding.

To make a good contact, the first and second bonding conditions were carefully optimised by adjusting the parameters as listed in Table 4.3. These parameters were determined such that the bonding would not damage the contact pads with stable connections for electrical measurements.

Table 4.3: Optimised wire bonding parameters.

Parameters	1st bond	2nd bond
Force (g)	50	50
(N)	0.49	0.49
Ultrasonic power (W)	0.7	0.7
Time (ms)	120	120
Temperature (°C)	150	150

Here, the magnitude of required force can vary depending on the position of the counterweight on the bonding head cover. Re-adjustment may be required for different sample-stage height. In this study the counterweight and sample-stage height were set to be 20 g and 10.15 cm, respectively.

Chapter 5

Characterisation Techniques

This chapter describes the equipment and techniques used for the electrical measurements and characterisation in this work. For effective characterisation to be undertaken, it is essential that apparatus is designed and constructed to meet the purpose of this work. Specific modifications are required for more general apparatus to make accurate and reproducible measurements on the devices that have been produced. It is critical to reduce the number and the magnitude of errors from specific sources. It is also necessary to design measurement procedures and protocols to ensure the above requirements. The distributions in device dimensions due to the fabrication process is also assessed by scanning electron microscopy which has sufficient resolution.

5.1 Transport measurement setup

The main focus of this section is to discuss the measurement setup developed to perform the I - V characterisation of the nanodevices. The setup consists of four major components: direct-current (DC) electrical measurement equipment, a high vacuum cryostat (2×10^{-3} Pa) to hold the sample and to isolate it from the environment, an electromagnet to generate magnetic fields of up to ± 0.3 T,

and a PC with National Instruments LabView and Data Acquisition (DAQ) card [113]. Figure 5.1 shows the experimental setup which was used for the electrical and magneto-transport measurements.

The devices were mounted on a 20-pin chip carrier (see Fig. 4.10) and placed on a specially designed chip holder fixed inside the cryostat mounted between the pole pieces of the electromagnet. The chip holder could be rotated inside the cryostat to align the devices precisely along a magnetic field. The cryostat was evacuated by a combination of rotary and turbo pumps in order to avoid electrical arcing during the measurements.

The chip carrier was connected via a home-made breakout box to the electrical measurement units, which consisted of a DC current source (Keithley, Model 2400) and a highly sensitive nanovoltmeter (Keithley, Model 2182A). All the instruments were controlled by customised LabView software via a GPIB DAQ card. This allowed the control of the measurements remotely and the synchronisation of the functions of the equipment. The collected data were saved as a file in the Excel format.

All the measurements were performed at room temperature (RT). A DC current with the magnitude ranging from 1 to 45 μA was applied. The connection box allowed three states for each contact, *i.e.*, grounded, floating and connected to the measurement unit device (MUD). This was crucial to protect the samples from sudden current flow or electrostatic discharge (ESD).

5.2 Noise and errors in electrical measurements

Low level signal to noise ratio (S/N ratio) measurements are often made on devices with low source impedance. Electrical noise has to be minimised in making such measurements. Noise can be particularly severe for non-local voltage measurements which require the detection of small voltages of the order of nV.

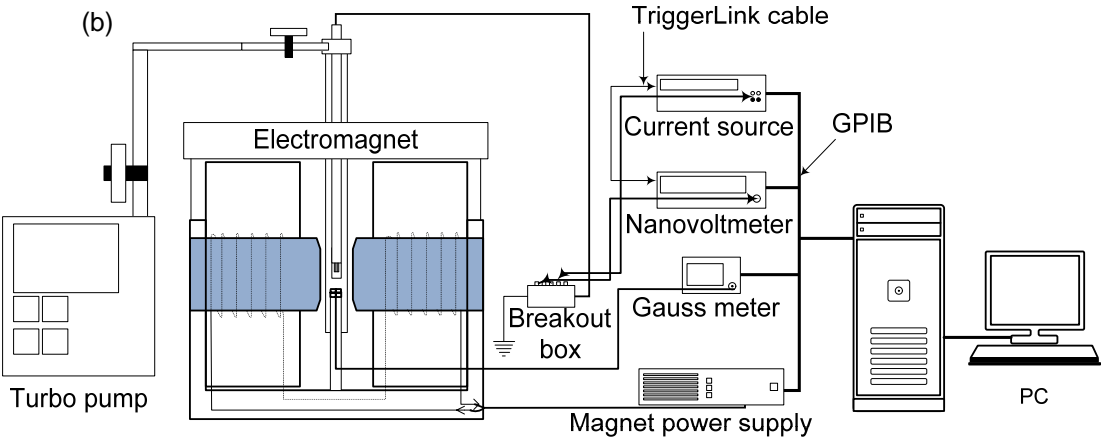
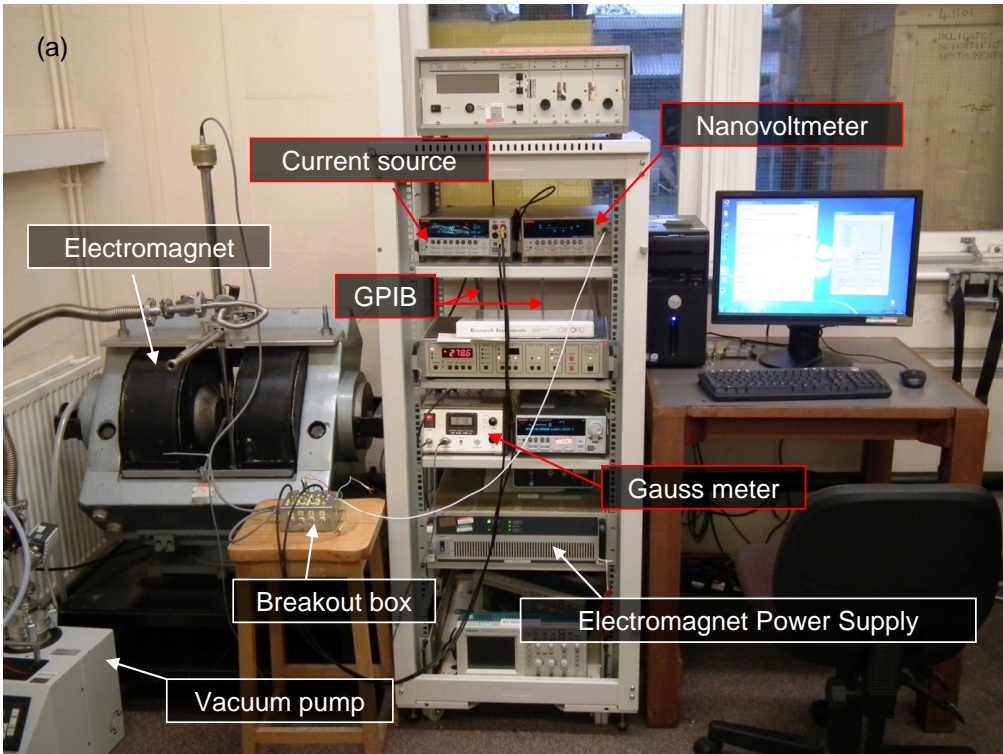


Figure 5.1: (a) Photograph and (b) block diagram of the electrical and magnetotransport measurement setup.

Therefore it is crucial that noise levels and origins are well understood for such weak signals. The probable sources of electrical noise are the equipment itself, inductive loops and thermal fluctuations in the sample during the measurements.

For low voltage measurements, errors are composed mainly of white noise (random noise across all frequencies), flicker noise, shot noise, thermoelectric voltages (electromotive force or EMF) and the voltage drop in leads and junctions [114,115]. These can be reduced during the measurements by simple techniques such as averaging, filtering and shielding.

Electrical measurements on nanoscale devices provide additional challenges to reduce the noise further. This is because in nanoscale device measurements, the applied current needs to be kept small (typically $\leq 45 \mu\text{A}$ in this study) to prevent heating or even damage the device. Actual signals to be measured are often hindered by noise which severely affects accuracy. In the following subsections the most common sources for noise are discussed.

5.2.1 Thermal noise (Johnson noise)

Thermal noise was discovered by J. B. Johnson in 1927 [116,117]. A year later Nyquist published a paper offering theoretical explanation for Johnson's measurements based on thermodynamics [118]. It is also called white noise because it is generated by random thermal motion of the charge carriers inside electrical resistors across all frequencies. The noise level can theoretically be determined from the temperature, resistance and frequency bandwidth. The root mean square (rms) of the noise level (V_J) generated is given by:

$$V_J(\text{rms}) = \sqrt{4k_B T R \Delta f}, \quad (5.2.1)$$

where k_B is the Boltzmann constant, T is temperature, R is the resistance of a device under the test (DUT) and Δf is the measurement bandwidth.

This is unavoidable noise regardless of any applied voltages. One can reduce this noise by lowering one of the above parameters in Eq. 5.2.1, such as lowering T , R or Δf . Cooling the device under the test from room temperature (293 K) to liquid nitrogen temperature (77 K) may reduce the voltage noise by approximately a factor of two [114], but reducing temperature is not practical in this study. Therefore, in this study a digital-averaging filter and integrating over multiple measurement cycles were considered as a first attempt to lower Δf , *i.e.*, lowering the noise level. The moving average filter, which uses a first-in first-out memory stack, was used because of its fast averaging processes (typically 100 Hz in this study). For the first reading, the stack is filled and the readings averaged [119]. For the subsequent readings the oldest reading in the stack is removed and replaced with the next one, providing a new average.

However reducing the bandwidth too much increased the response time of the measurements, and consequently the measurements took a very long time (~ 20 s). This made the measurements more susceptible to the other noises, such as a thermoelectric voltage due to temperature drifting (see Section 5.2.4). Therefore the other technique developed more recently to minimise the noise was used. This technique is called “*DC reversal*” and uses DC polarity reversals in the applied current signal to minimise the noises. Although the reduction of the noise level of this technique is still limited by the bandwidth of the instruments, this is selected in this study to minimise the thermal noise. The details of this technique are explained in Section 5.3.

5.2.2 Flicker noise

Flicker noise is also a critical type of noise, which is called “ $1/f$ -noise” or “*pink noise*”. It appears in electronic components, test circuits and instruments, and is defined by the shape of its spectral power density $S(f)$ [120]. The power of the

noise level is approximately proportional to reciprocal frequency:

$$S(f) \propto \frac{1}{f^\alpha}, \quad (5.2.2)$$

where f is frequency and $0 < \alpha < 2$.

The flicker noise is induced by a variety of effects, such as temperature, humidity and chemical reactions within components. The effect of this noise can be reduced by running the measurement at higher frequency (typically less than 1 kHz) [121].

It is challenging but not impossible to filter the flicker noise. Conventionally, an alternating-current (AC) lock-in amplifier has been used for measurements in the mid-range resistance between 100 m Ω and 1 M Ω [114]. With this method small AC signals down to a few nanovolts can be accurately measured even when the background noise is higher than the signals to be measured. It relies on “phase sensitive” detection to single out the signals at a selected test frequency (typically around 13 Hz [114]) from the other frequencies related to the flicker noise. However the reduction of the flicker noise with this technique is not as good as the “DC reversal”. This is due to the low common mode rejection ratio (CMRR), which specifies how well an instrument can reject noise signals superimposed to a voltage to be measured [114]. Therefore in this work the latter technique, “DC reversal”, was used which has a capability to reject the $1/f$ voltage noise by 10 times better than the AC lock-in technique at a frequency of 9 Hz.

5.2.3 Shot noise

Shot noise is the other random noise which involves the fluctuations in an electric current. It is induced by the discreteness of the electric charge flow [122]. The root mean square (rms) value of this current noise (I_{noise}) is given by the

Schottky formula:

$$I_{\text{noise}}(\text{rms}) = \sqrt{2eI\Delta f}, \quad (5.2.3)$$

where e is the electron charge and I is the operating electrical current.

The shot noise is more pronounced in mesoscopic devices particularly for low current measurements. The shot noise is a direct consequence of the intrinsic properties of the charge carriers in an electrical conductor, such as quantisation of charge and spin of electrons, particularly in a non-equilibrium transport state [123, 124]. From Eq. 5.2.3, one can find that the magnitude of the shot noise increases with increasing the square root of the applied current (\sqrt{I}). Since the magnitude of the signal itself (a non-local voltage in this study) increases more quickly than the noise level, the S/N ratio increases accordingly. In this study, by increasing only the injected current from 10 μA to 45 μA , in particular for non-local geometry measurements, the S/N ratio has been increased from 12.5 dB to 30 dB without inducing any other noises. This clearly indicate that the S/N ratio can be improved by three orders of magnitude by optimising the injected current.

5.2.4 Thermoelectric voltage

A thermoelectric voltage is the most common source of noise in low voltage measurements. When two different metal conductors are connected together in a circuit and one of the junctions is at a higher temperature than the other, an electrical potential difference across the open end will appear as shown in Fig. 5.2. This phenomenon is known as the Seebeck effect [125]. The magnitude of this potential difference depends on the type of material used and the temperature difference between the two junctions, which can be defined as:

$$V_{AB} = Q_{AB}(T_1 - T_2), \quad (5.2.4)$$

where V_{AB} is the thermoelectric voltage induced, Q_{AB} is the Seebeck coefficient of material A with respect to B (in $\mu\text{V K}^{-1}$) and T_1 and T_2 are temperatures at the

two junctions (in K). Typically the voltage is in the range of $\mu\text{V K}^{-1}$ to mV K^{-1} .

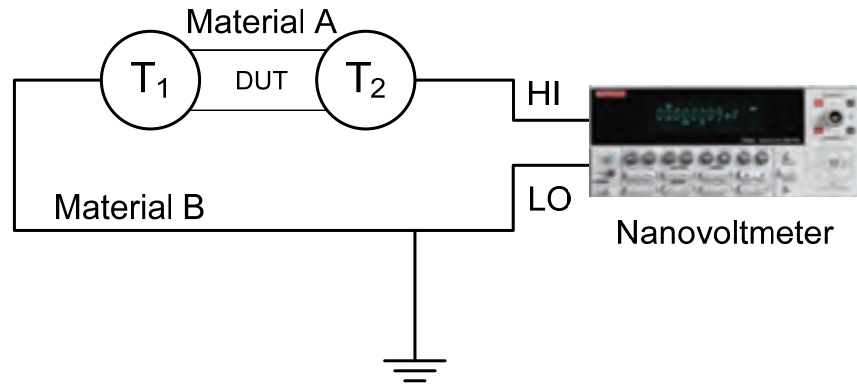


Figure 5.2: Illustration of thermoelectric voltages induced in a circuit consisting of two different materials A and B at two different temperature T_1 and T_2 .

A conventional way to reduce this undesired voltage is the maintenance of a constant temperature around the device under test (DUT). Constructing circuits using the same material for all connections further minimises thermoelectric voltage generation. Sometimes different metals used at connections are unavoidable, inducing a very large thermoelectric voltage under a small temperature difference. In such a case, extra efforts are to be made to maintain the ambient temperature constant with using a high vacuum cryostat for example. The “DC reversal” technique is another way to cancel out such thermal noise (see Section 5.3).

5.2.5 Lead resistance errors

Serious lead resistance errors can arise when a simple two-terminal resistance test is performed as shown in Fig. 5.3. The effect of the lead resistance is particularly important when the resistance of the device under the test is much smaller than the lead resistances. As a result, the lead resistance can induce significant errors since the measured voltages across the leads dominate, providing unexpected changes in the voltage across the device [126].

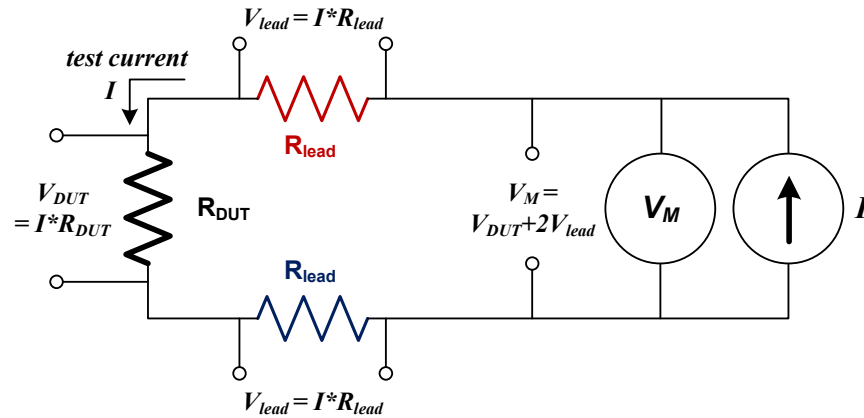


Figure 5.3: Schematic diagram of the two-terminal resistance measurement [126].

This systematic error can be avoided by using a four-terminal (Kelvin) connection as shown in Fig. 5.4. There are two connection wires on each contact. A constant current is driven through one pair of wires, while the resulting voltage drop is measured with the other pair of wires. The high internal resistance of the voltmeter across the device minimises any current flow and thus allows the measurement of only the potential drop across the device under the test. This is the setup used in this study.

5.3 DC reversal measurement technique

When measuring very small electrical signals in the nV range, one has to overcome various difficulties. The above mentioned errors and the low-level S/N ratio are the major issues. For this work a relatively new measurement method known as the “DC reversal” technique has been used to increase the S/N ratio. This technique is often referred as the “two-point Delta Mode” [114].

The electrical circuit as shown in Fig. 5.5 was the instrumentation setup of this measurement technique. Here a DC current source (Keithley, Model 2400)

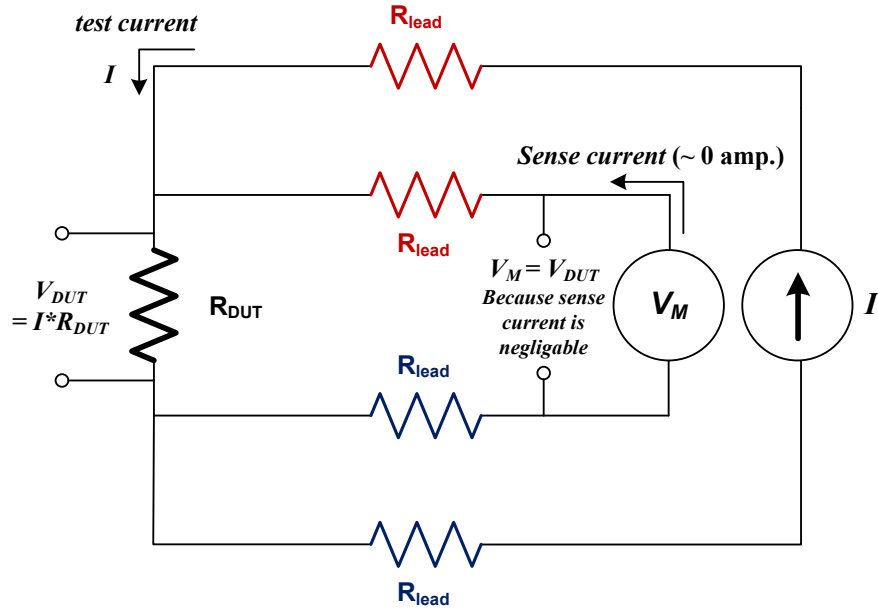


Figure 5.4: Schematic diagram of a four-terminal (Kelvin connection) resistance measurement [126].

was used to supply a bipolar test current of up to about 13 Hz. A nanovoltmeter (Keithley, Model 2182A) was used to evaluate the mean voltage across the device under the test. These instruments were linked by a communication cable (Trigger Link) that synchronised them. Working as one unit, they could effectively cancel out the thermoelectric offsets and low frequency noise as detailed below.

This technique basically utilises the AC source polarity and averages the two corresponding voltage readings to determine the potential difference of the device under the test [see Fig. 5.6(a)]. The two voltage readings represent:

$$V_{M1} = V_{DUT} + V_{EMF}, \quad (5.3.1)$$

$$V_{M2} = -V_{DUT} + V_{EMF}, \quad (5.3.2)$$

where V_{M1} and V_{M2} are the two voltage readings at the two I_{M1} and I_{M2} DC currents, V_{DUT} is the voltage drop in the device under the test and V_{EMF} is the thermoelectric voltage offset which is constant during the measurement time. Elim-

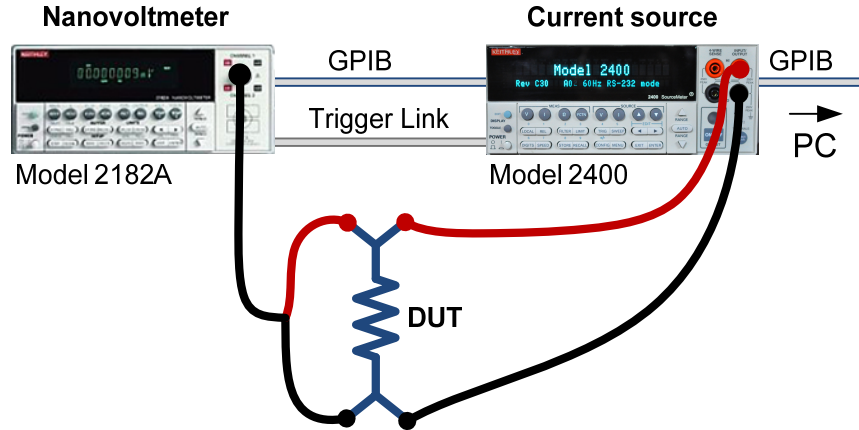


Figure 5.5: Instrumentation setup for the “DC reversal” technique.

ination of the constant thermoelectric voltage offset (V_{EMF}) is possible through a simple subtraction of the two voltage readings as follows:

$$\begin{aligned}
 V_{DUT} &= \frac{V_{M1} - V_{M2}}{2} \\
 &= \frac{(V_{DUT} + V_{EMF}) - (-V_{DUT} + V_{EMF})}{2} \\
 &= \frac{V_{DUT} + V_{EMF} + V_{DUT} - V_{EMF}}{2} \\
 &= \frac{2V_{DUT}}{2}.
 \end{aligned} \tag{5.3.3}$$

Successive readings are averaged using Eq. 5.3.3 to minimise the measurement noise levels. Faster switching of the current polarity between positive and negative can decrease the noise level substantially. For fast alternation any noise whose time constant is greater than the one-cycle period of the “DC reversal” mode measurement can be removed [114, 115]. Therefore to achieve high speed measurement, fast computation and precise synchronisation between the source and the nanovoltmeter are crucial. These can be achieved by using *two-point digital moving-average algorithm* [119] and the TriggerLink cable provided by Keithley [127]. Additionally another method to synchronise the nanovoltmeter with the current source has been developed based on the trigger count of the source meter. This allows the process of the measurement in a discontinuous mode, *i.e.*, buffering V_{DUT} at a maximum rate of 9 Hz with optimised Delta

measurement time without producing extra noise [128].

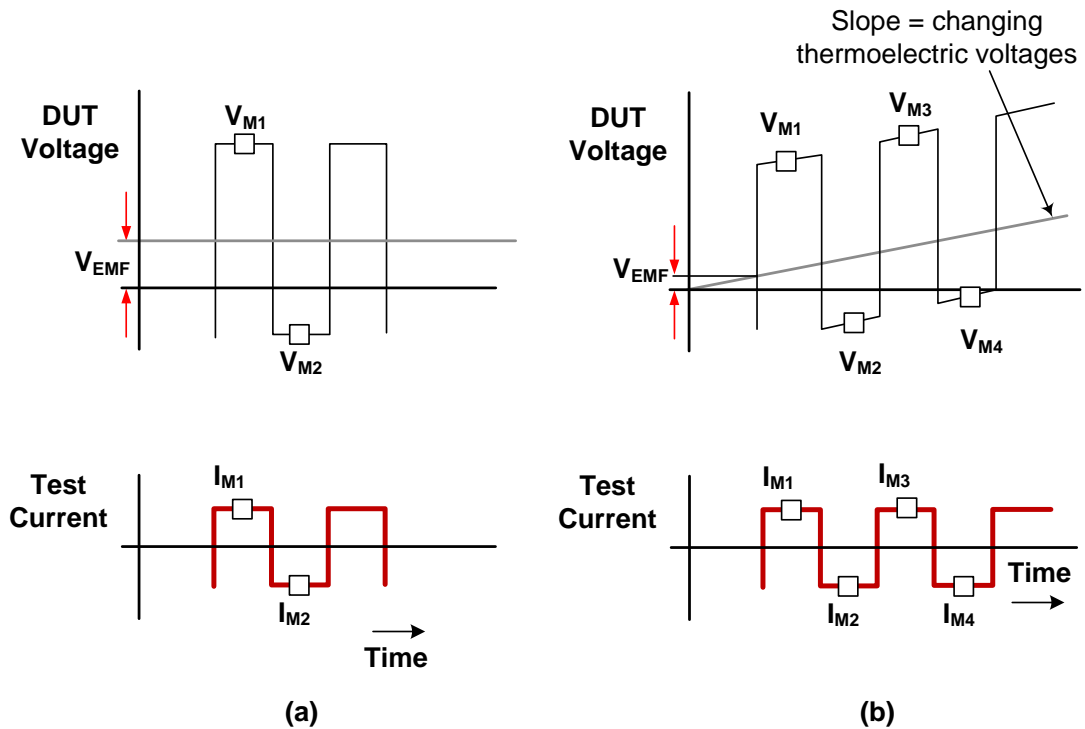


Figure 5.6: Test signal for the “DC reversal” measurements (a) with and (b) without thermoelectric offset errors [129].

It is important to mention that V_{EMF} will not always be constant between the two consecutive voltage readings as shown in Fig. 5.6(b). In nanoscale devices the current density is extremely high because of their small dimensions, which induces Joule heating in the circuit with measurement time. Therefore the two-point Delta technique cannot sufficiently compensate the changes between the two positive and negative test currents. For this reason one has to reduce either the magnitude of the current or minimise the averaging points per each data without compromising the S/N ratio [114]. The other techniques, such as a pulse and three-point Delta method, can measure the device resistance more accurately at very low power [114]. In this study, two-point Delta technique was used with the optimised parameters as detailed below.

A customised LabView programme was written to implement the two-point Delta technique (see appendix B for the LabView code). All the measurement

parameters, such as current amplitude and the number of averaging points, were controlled on the front panel of this program as shown in Fig. 5.7.

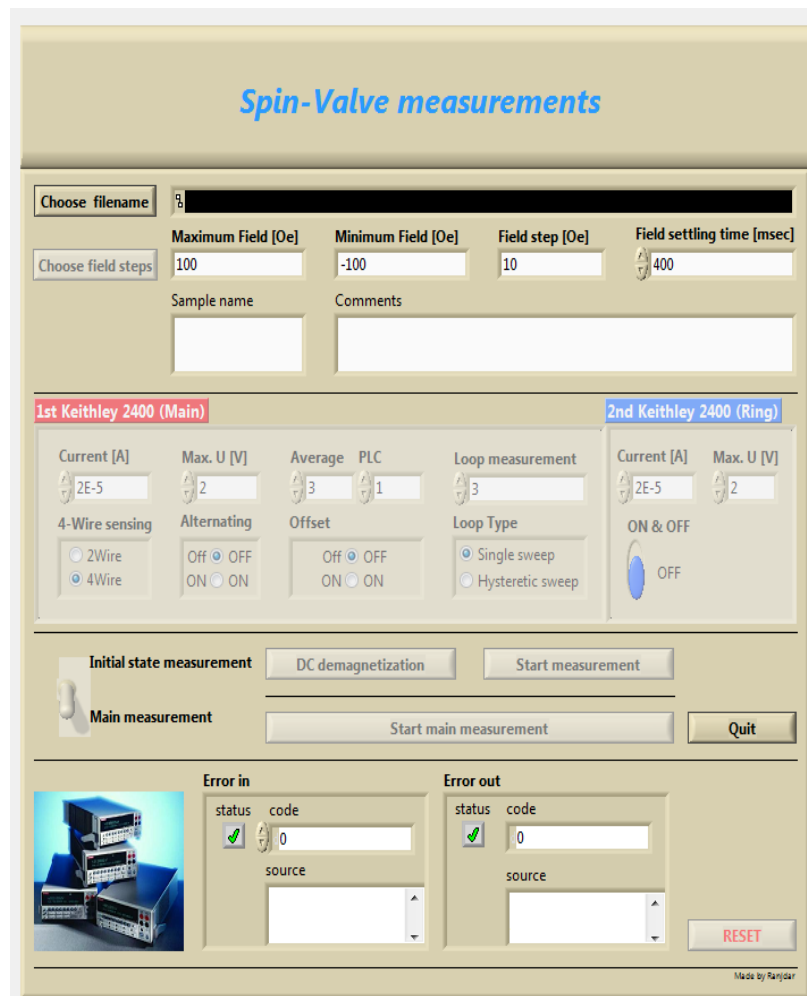


Figure 5.7: Front panel of the “DC reversal” LabView programme.

In this work, three different types of electrical measurements were carried out. First, conventional I - V measurements were performed to measure the electrical resistivity of the materials. The second measurement was a device test measurement to determine the maximum current loading without breaking the device. The third measurement was the non-local I - V measurement to observe the magneto-transport behaviour. For these three measurements three different customised LabView programmes were written based on the above code.

5.4 Scanning electron microscope

A scanning electron microscope (SEM, FEI Sirion, XL30) as shown in Fig. 5.8 is a type of electron microscope, which uses a focused beam of high-energy electrons to construct an image of surface topography of solid specimens. A beam of electrons is generated at the top of the microscope by an electron gun. The beam follows a vertical path through the column of the microscope, which is held in a vacuum [see Fig. 5.8(b)]. The beam travels through a series of electromagnetic lenses which focus and direct the beam down toward the specimen. Controlled by a computer, the SEM can adjust the beam to be focused and scanned over the surface area of interest.

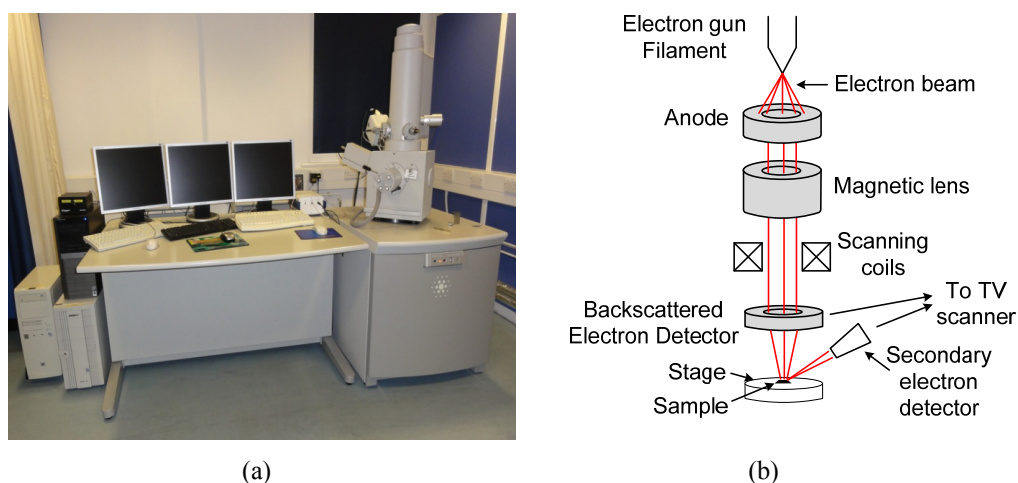


Figure 5.8: (a) Photograph and (b) schematic diagram [130] of the SEM located at the York JEOL Nanocentre.

Once the beam comes in contact with the sample, energised electrons and photons are released from the surface of the sample, including secondary and backscattering electrons as well as X-rays with energies and wavelengths specific to the elements present (see Fig. 5.9). A variety of detectors, such as one for secondary electron in this study, is used to collect these scattered waves and converted them into a signal that generates the image. This process forms the final image.

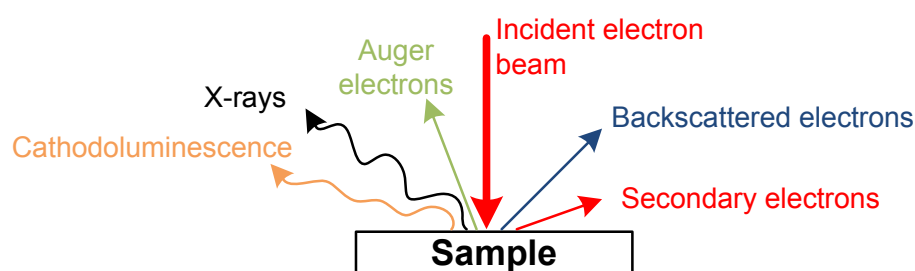


Figure 5.9: Schematic diagram of electron-sample interactions [131].

Since the SEM is operated under a high vacuum (1×10^{-5} Pa) and utilises electrons to form images, special sample preparation is required. This means that liquids and materials containing water and other volatile components cannot be observed directly. They need to be dehydrated or removed. Powder samples are required to be set firmly in a specimen holder so as not to contaminate the vacuum chamber.

Non-conductive materials need to be connected electrically to a conductive specimen holder and to be covered with a thin conductive film by sputtering or evaporation. Typical materials for coating are Gold, Platinum, Carbon and their alloys. In this way the quality of the SEM image can be improved by avoiding the charge accumulation on the surface of the specimen [132].

In this work in order to avoid such charging artefacts, each sample had to be prepared prior to the imaging. The sample was immersed in cyclopentane for at least 24 h and then sonicated for ~ 30 s. The sample was then briefly washed in cold isopropanol and dried by N_2 gas. The sample was mounted on an Aluminum pin mount secured with a Copper conductive tab in order to ground any possible surface charging as shown in Fig. 5.10.

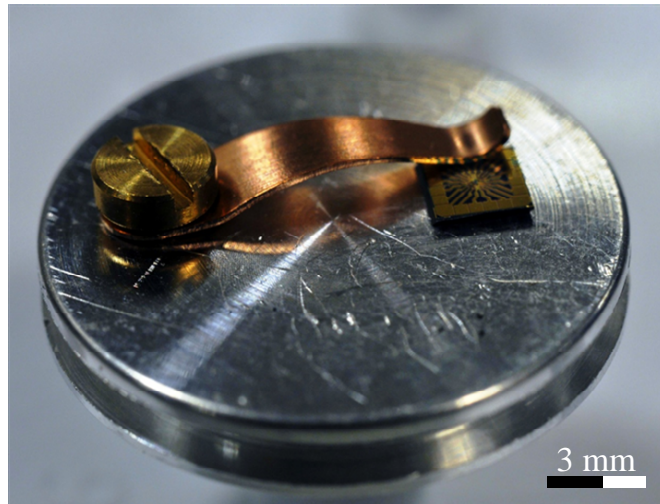


Figure 5.10: Sample holder for SEM with a spring clip.

Chapter 6

Optimisation of the Fabrication and Measurement Processes

In this chapter transport measurements on the preliminary and LSV devices with a straight NM nanowire are presented. The electrical and magnetical parameters, such as electrical resistivity (ρ), spin diffusion length (λ_s) and spin injection/detection efficiency (η) are measured. The obtained results are feedback for the optimisation of the fabrication and measurement processes.

6.1 Ladder devices

Minor variations in fabrication procedures can lead to a major distribution of device properties, such as electrical resistivity, spin diffusion length and spin injection/detection efficiency. It is not possible to anticipate that every nanowire in a sample has a well-defined geometry and the same properties. A partially failed lift-off process can alter the actual form of the nanowires and induce non-reproducible electrical behaviour.

Hence, as discussed in Section 4.2 ladder devices (see Fig. 6.1) were first fabricated and characterised by measuring their electrical resistivity by the four-terminal I - V measurement. Because of the available multiple terminals, the uniformity of the resistance along the horizontal wire was also investigated.

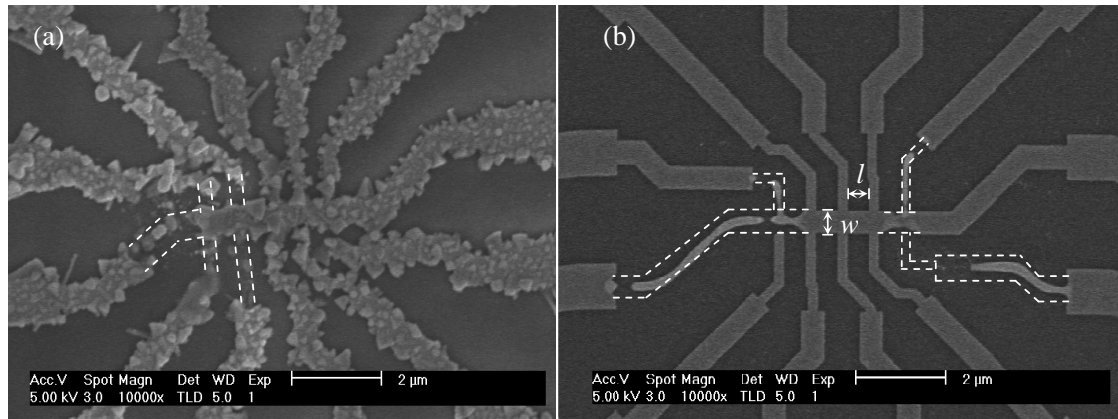


Figure 6.1: SEM images illustrating the ladder devices made of only (a) non-magnetic Cu and (b) ferromagnetic Py.

Two sets of the ladder samples were characterised. They were made of only non-magnetic Cu and ferromagnetic Py nanowires deposited in a single step as shown in Figs. 6.1(a) and (b), respectively. The images were taken after the electrical measurements to avoid any possible damages induced by SEM observation. Each device consists of five vertical nanowires, which were connected via a horizontal bridging nanowire as schematically shown in Fig. 4.1(a). The width of the horizontal nanowires (w) and the edge-to-edge distance of the adjacent vertical nanowires (l) were designed to be $w = 500$ nm and $l = 500$ nm, respectively.

Figure 6.1(a) has many oxide-like grains on the surface and hence cannot be used for the size measurement. From Fig. 6.1(b) the device size was measured to be $w = (500 \pm 7)$ nm and $l = (483 \pm 7)$ nm. The thickness of the Cu and Py films were $t_{\text{th}} = 30$ nm. In order to guarantee good Ohmic contacts between the EBL-patterned devices and the photolithographically patterned electrodes without suffering from oxidation, a capping layer consisting of Cr(2 nm)/Au(5 nm) was

deposited on the Cu and Py films.

The deposited metals were purchased from Alfa Aesar in pellets with their purity of 99.95% for both Py and Cu. However, evaporation materials might react with the residual gas molecules in the chamber during the deposition and therefore the purity of the deposited nanowires could not be as good as the original pellets [133]. In order to increase the purity of the material deposited, it was crucial to work in extremely clean environment. In this study, the metal chamber was kept in a high vacuum with the base pressure below 5×10^{-5} Pa.

The resistivity of a metal, from which the wire is made, can be obtained by the equation,

$$\rho = \frac{RA}{l}, \quad (6.1.1)$$

where R is the electrical resistance, l is the wire length and A is the cross-sectional area of the wire (*i.e.*, $A = t_{\text{th}} \times w$). Given this description, the resistivity does not change with the size or shape of the wire. ρ is an intrinsic property which depends on the materials used and the presence of impurities in them [30, 134, 135]. This means that the resistivity can be used as a good indicator to check the purity of the deposited materials.

The setup which was detailed in Section 5.1 was used to perform the electrical measurements at RT. A demagnetising sweeping field was first applied to nullify any possible magnetic fields. Figure 6.2(a) shows a schematic diagram of the ladder device for a four-terminal measurement. The “DC reversal” technique was used to measure the I - V characteristics. The current (I) was passed through the horizontal nanowire and the nanovoltmeter was placed between the two inner contacts, *e.g.*, between contact 1 and 3 as shown in Fig. 6.2(a). The measurement was repeated with moving the voltage probes to the other contacts. The purpose of repeating the measurements with different contacts was to check the quality of the entire ladder devices. Here, the 300 nm thick SiO_2 layer between the Cu and Py nanowires and the Si substrate eliminated current

shunting into the substrate during the measurements as shown in Fig. 6.2(b).

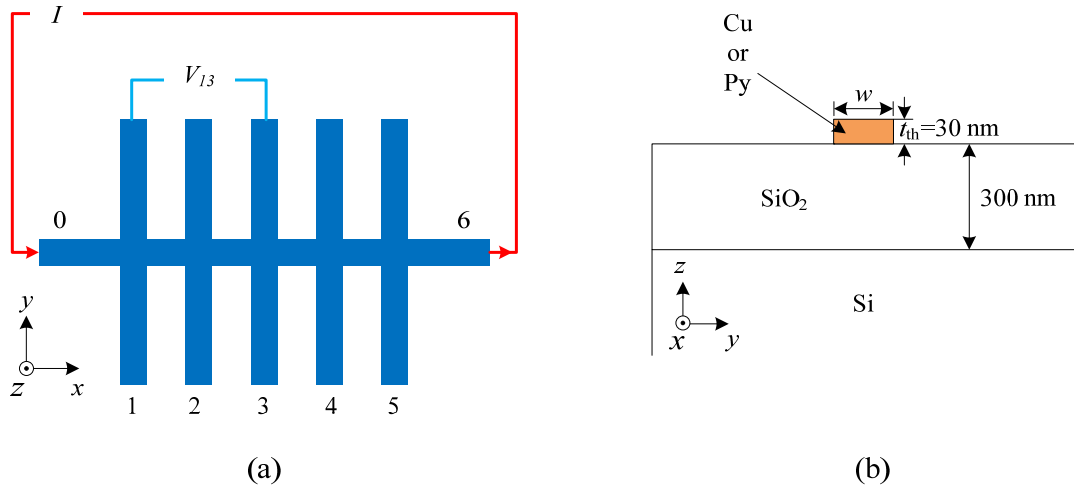


Figure 6.2: (a) Schematic diagram of the measurement configuration for the ladder device. (b) 2D cross-sectional view of the horizontal nanowire with the substrate.

Each measurement was made by taking 50 delta points and 15 moving average filters at each applied current to minimise the white noise. The current range was between 1 to 20 nA with a step of 5 nA for the Cu ladder devices. For the Py ladder devices the current range was reduced to 1 to 15 nA in order to prevent Joule heating because of expecting higher resistivity in Py as compared with that in Cu. Voltage responses against applied currents for the Cu and Py devices were plotted in Figs. 6.3(a) and (b), respectively.

As one can see in these graphs, the linear response of the voltages with the applied currents shows that any possible thermoelectric voltages are diminished by the “DC reversal” technique. Resistances are calculated by taking the gradient of the I - V characteristic curves. Knowing the resistance and the dimensions of the nanowires, one can calculate the resistivity of the materials by substituting these values into Eq. 6.1.1.

For the Cu sample, $\rho_{\text{Cu}}(293 \text{ K})$ is calculated to be $(7.53 \pm 0.13) \mu\Omega \text{ cm}$, which is almost five times larger than the bulk Copper resistivity $\rho_{\text{Cu}}^{\text{Bulk}} = 1.68 \mu\Omega \text{ cm}$

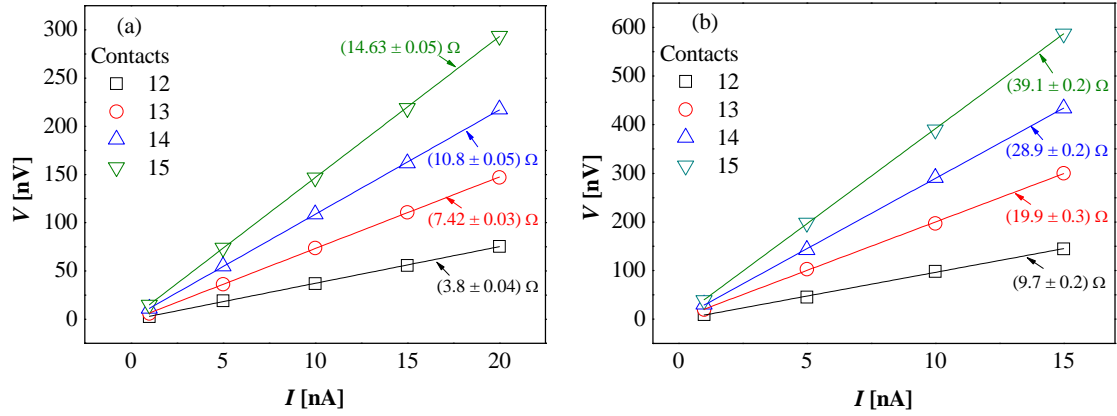


Figure 6.3: Voltage responses against applied currents for (a) Cu and (b) Py ladder devices measured by the four-terminal I - V setup with different contact configurations.

[136]. This is expected because the resistivity of thin nanowires can be fundamentally different from that of a bulk material. In a bulk material the conductance is described by the overlap of the conduction and valence bands. These bands are usually determined using periodic boundary conditions by assuming an infinite crystal structure [30]. This means the surfaces and edges of the material are completely neglected. In thin films and nanowires these cannot be neglected since the other resistivity, such as surface resistivity, contributes strongly depending on the thickness of the film and a neighbouring materials at the interface [137–141]. However the calculated value of ρ_{Cu} is still approximately twice higher than the resistivity value ($\rho_{\text{Cu}} = 3.7 \mu\Omega \text{ cm}$ [142]) reported in the nanostructures in a similar dimension ($t_{\text{th}} = 40 \text{ nm}$ and $w \approx 200 \text{ nm}$). This can be explained by enhanced carrier scattering at the rough surfaces of the nanowires as seen from Fig. 6.1(a). The surface is highly contaminated which can eventually induce larger resistivity across the Cu nanowire.

However, this is not observed in the Py sample as shown in Fig. 6.1(b). $\rho_{\text{Py}}(293 \text{ K})$ is estimated to be $(20.93 \pm 0.35) \mu\Omega \text{ cm}$, which is found to be in the same order with those reported for Py thin films in a similar dimension ($t_{\text{th}} = 30 \text{ nm}$) [19, 107, 143, 144].

Another important point to be considered from Fig. 6.3 is the following: The voltage across the horizontal nanowire increases linearly with increasing nanowire length l . This clearly indicates that the nanowires were uniformly deposited and patterned on the substrates.

6.2 Cu/Cu LSV devices

In order to eliminate the surface contaminations of the Cu ladder devices, another set of Cu/Cu nanowires were fabricated using the two-step LSV patterning method as detailed in Section 4.2 (see Fig. 4.1). For these devices, the capping Cr/Au layers were not deposited to minimise any possible particulate contaminants arising from the post processes for the device fabrication. Instead, a thin LOR3A resist layer was coated on the surface of the devices in order to protect the underlying metallic nanowires from oxidation and damage. As expected the surface contaminations were not formed as shown in Fig. 6.4. The thickness and width of the horizontal bridging wire were designed to be 70 nm and 250 nm, respectively. The width was measured to be (255 ± 12) nm wide from Fig. 6.4. The edge to edge distance between the two vertical Cu wires was designed to be 400 nm and was measured to be (420 ± 14) nm from Fig. 6.4. The increase in the width of $\sim 5\%$ from the designed value might be due to oxidation at the edges of the nanowires as observed as white particles in Fig. 6.4. These oxides might have formed during the measurements.

By using the four-terminal setup and “DC reversal” technique with a test current of $50 \mu\text{A}$, the resistivity measurements were repeated for the horizontal bridging wire. As expected the calculated resistivity was reduced to $\rho_{\text{Cu}} = (3.9 \pm 0.9) \mu\Omega \text{cm}$, which was approximately in the same order with the resistivity reported in previous works [16, 142, 145–147]. This clearly indicates that the surface of the new devices were clean without forming any surface

contaminations.

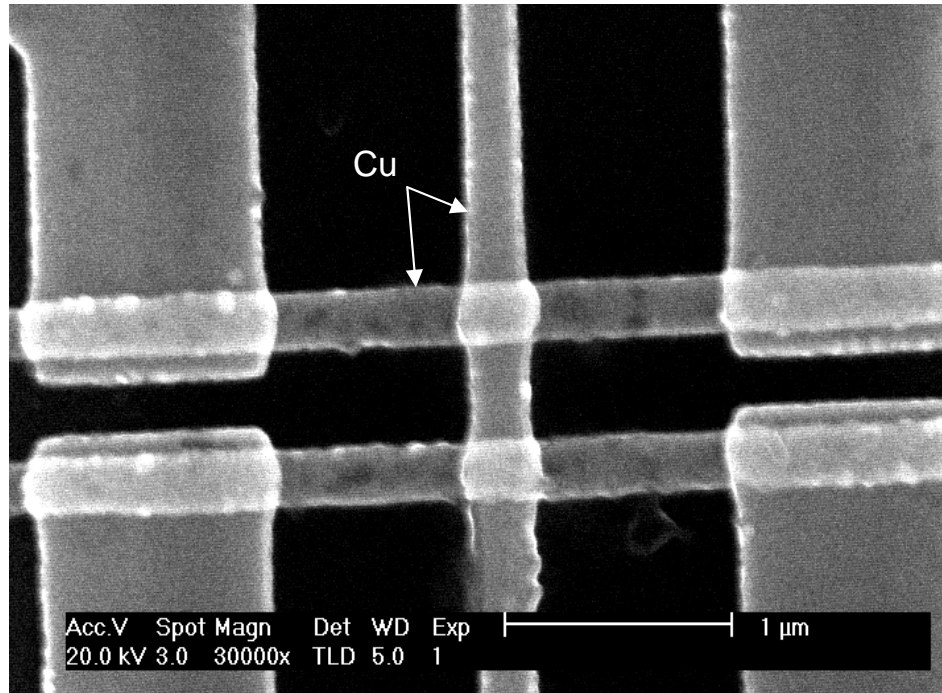


Figure 6.4: SEM image of a typical Cu/Cu LSV device without a Cr/Au capping layer.

6.3 Py/Cu LSV devices with a straight NM wire

Prior to the final fabrication of the ratchet devices, Py/Cu LSV devices with a straight NM Cu wire were fabricated. The aims of fabricating these devices were to investigate their electrical and spintronic properties before studying the actual spin-current amplification effect. As a result, the fabrication procedures were optimised and were used for the ratchet device to be discussed in the next chapter.

The Py/Cu LSV devices were fabricated in the same fabrication conditions used for the previous Cu/Cu devices. Three different designs of the LSV structures were fabricated: $w = 100$ nm, 200 nm and 500 nm with a series of l (see

Table 4.1). A typical LSV device is shown in Fig. 6.5. To avoid magnetic fringe fields from the ferromagnetic electrodes, 30 nm thick Py electrodes were deposited first on a thermally oxidised Si substrate. Both Py wires were equal in their width ($w_{\text{Py}1} = w_{\text{Py}2} = w_{\text{Py}}$) and equal to the width of the Cu channel ($w_{\text{Py}} = w_{\text{Cu}} = w$). In Fig. 6.5, w_{Py} and w_{Cu} were designed to be 200 nm and were measured to be (200 ± 3) nm and (199 ± 4) nm, respectively. The Py wires were different in shapes at their ends as shown in Fig. 6.5(a): the first (Py1) had sharp ends and the second (Py2) had square ends to assist domain nucleation for reversal at lower magnetic fields [106]. These shapes allowed to differentiate clearly the two magnetisation configurations, parallel and antiparallel, of Py1 and Py2 by applying a magnetic field along the Py wire. In the next step, a 70 nm thick horizontal bridging Cu nanowire was also fabricated. Here, the surface of the first layer (Py) had to be exposed to the ambient atmosphere for prolonged time, causing contamination and formation of oxides. Therefore the oxygen plasma ashing, using a barrel asher at the power of 50 W for 30 s in 0.02 Pa O_2 environment, was employed to remove any oxidised layers and remaining resist from the surface of the Py electrodes before the Cu layer deposition. This guaranteed transparent and Ohmic behaviour for both the injector and detector interfaces which was necessary to inject and detect a spin-polarised current with high efficiency. It should be noted these devices had the same junction area for the injector and detector electrodes, which was very important to analyse the spin-transport properties of the LSV devices.

6.3.1 Local resistance test

In order to check the quality of the LSV contacts and identify any possible irregularities in their electrical transport properties, two different configurations to measure local resistance were carried out. Both configurations were based on the four-terminal measurement as shown in Fig. 6.6. In the first configuration, the resistance of the Cu nanowire was measured by passing a current I through

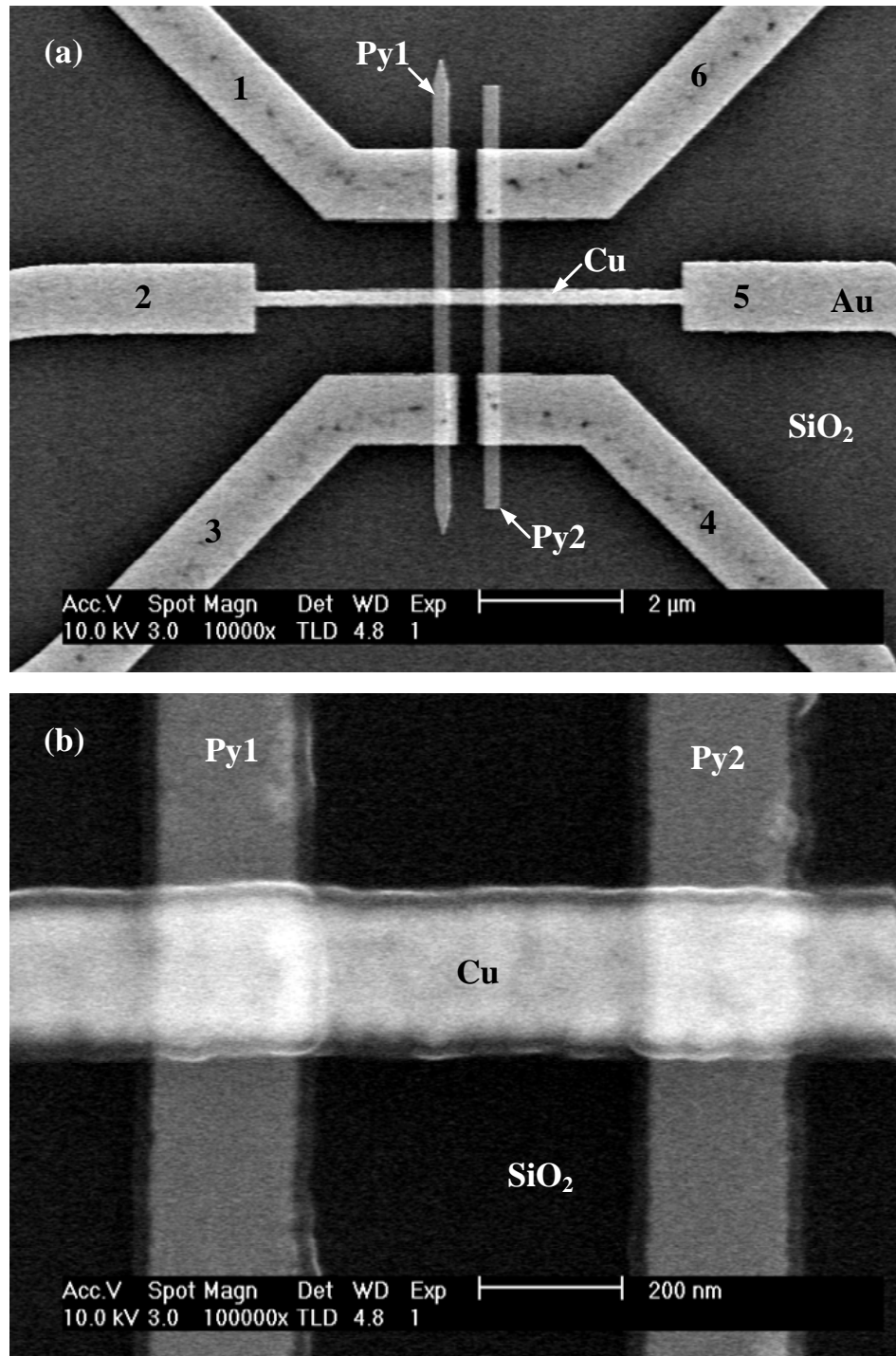


Figure 6.5: SEM images of (a) the Py/Cu LSV device and (b) its magnified junctions. Two vertical wires are the ferromagnetic electrodes, FM1 (Py1) and FM2 (Py2) with $l = (489 \pm 4)$ nm. Their sizes are $6.5 \times 0.2 \mu\text{m}^2$ and $5.8 \times 0.2 \mu\text{m}^2$, respectively. A non-magnetic Cu wire is placed to bridge the Py electrodes horizontally. A total of 6 contacts are connected to the device.

the Cu wire and measuring voltage V_{Cu} by the nanovoltmeter using the two top Py1 and Py2 electrodes [see Fig. 6.6(a)]. In the second configuration the resistance of the Py/Cu junctions was measured by sending a current through these interfaces using the local geometry, while sensing the voltages V_{L} and V_{R} across the left and right junctions, respectively, as shown in Fig. 6.6(b).

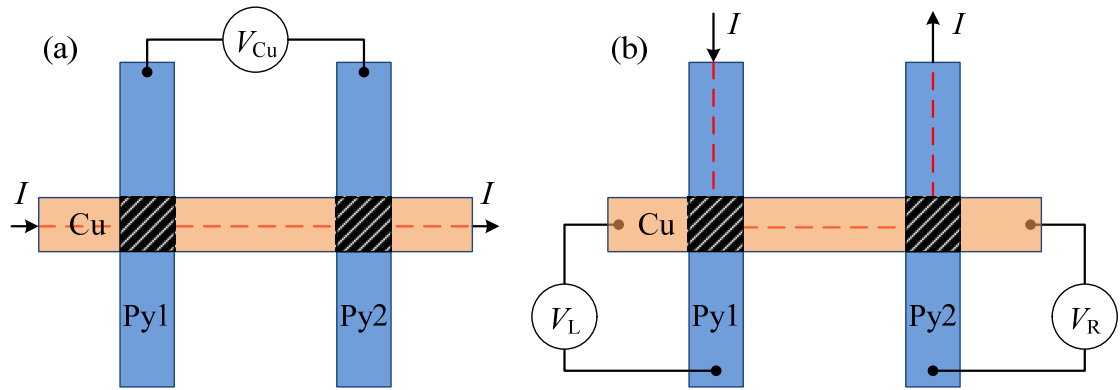


Figure 6.6: Schematic diagrams of four-terminal configurations to measure (a) the Cu channel resistance and (b) the resistance of the left and right Py/Cu interfaces as shaded.

Figures 6.7(a) and (b) show typical local resistances of one of the LSVs with a straight nanowire ($w = 500$ nm and $l = 250$ nm) measured by the above two configurations. The measured data are shown as square symbols, while the solid and dashed lines are their linear fits using Ohm's law ($R = V/I$). As one can see in the graphs, the I - V data points exhibit Ohmic response. The local resistances can be extracted from these fits. From Fig. 6.7(a), the resistance of the Cu channel can be calculated to be (824.2 ± 0.1) m Ω . By substituting this value into Eq. 6.1.1, the resistivity of the Cu wire is found to be $\rho = (3.85 \pm 0.01)$ $\mu\Omega$ cm, which is in the same order of the obtained data for Cu/Cu samples in the previous Section 6.2.

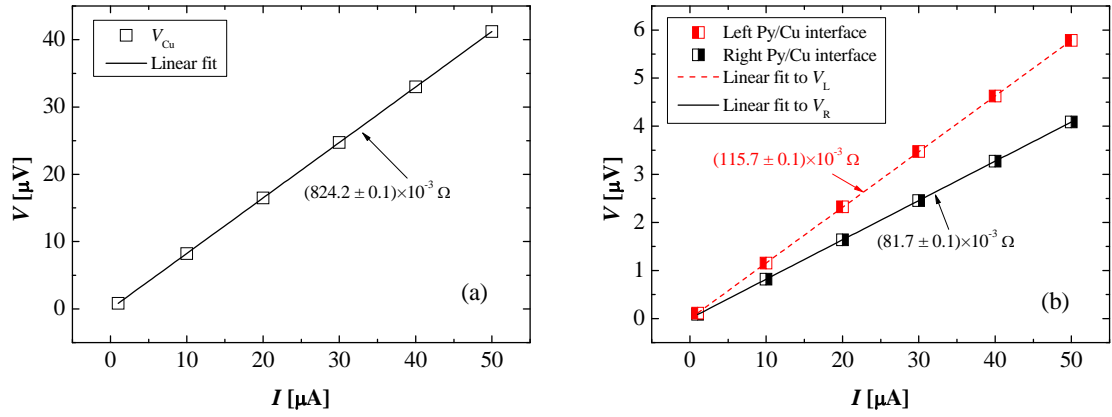


Figure 6.7: Typical local resistances measured for a LSV with the dimension $w = 500$ nm and $l = 250$ nm to estimate the resistances of (a) the Cu channel and (b) the Py/Cu junctions. The measured data are shown as square symbols, while the solid and dashed lines are their linear fits.

Figure 6.7(b) shows the resistances of the left and right Py/Cu junctions obtained by the second configuration. The graph indicates Ohmic behaviour again but with very low junction resistance ($< 0.1 \Omega$), leading to the interfacial resistance $R/A_J = 4 \times 10^{11} \Omega \text{ cm}^{-2}$. This evaluation procedure is repeated for all the samples, resulting in an upper limit of $(96.11 \pm 0.01) \Omega$ for the devices for spin-current amplification with junction area $A_J = 200 \times 100 \text{ nm}^2$, resulting $R/A_J = 4.8 \times 10^{15} \Omega \text{ cm}^{-2}$. A transparent interface typically shows 0.1Ω for $A_J = 1 \times 10^{-14} \text{ m}^2$ ($R/A_J = 1 \times 10^{13} \Omega \text{ cm}^{-2}$) [16,81,95,145]. The increase in this study can be attributed to the presence of minor contamination and oxidation between the Py and Cu nanowires [148], which requires further optimisation of the fabrication process.

6.3.2 Non-local spin transport measurements

The techniques described in the previous sections characterised the electrical properties of each Py and Cu nanowires and their junctions. Here, their spin transport properties were examined in the non-local geometry. In this section, three samples were measured; (1) Sample-500 with $w = 500$ nm and $l = 250$ nm

(2) Sample-200 with $w = 200$ nm and $l = 200$ nm and (3) Sample-100 with $w = 100$ nm and $l = 300$ nm. An external magnetic field (H) was applied up to ± 1 kOe along the Py nanowires.

The non-local spin-valve (NLSV) configuration is shown in Fig. 6.8(a) with an associated SEM image of a typical device in Fig. 6.8(b). The SEM image is labeled with the NLSV configuration of the current introduction and the nanovoltmeter measurement connections corresponding to those in Fig. 6.8(a). Py1 and Py2 represent the spin injector and detector electrodes, respectively.

The spin-current transport in the Cu wire was measured at RT by the “DC reversal” technique. The current ($I = 10 \mu\text{A}$) was injected from the Py1 electrode into the Cu wire and extracted from the left-hand side of the Cu wire. The non-local voltage (V) between the second Py2 electrode and the right-hand side of the Cu wire was measured to detect the spin accumulation in the Cu wire.

6.3.2.1 Non-local spin-valve signals

By sweeping H along the Py wires as shown in Fig. 6.8, the magnetisation configurations could be altered to induce the spin-valve effect as described in Section 2.3. Under a large positive magnetic field both Py wires were saturated along the applied field direction, *i.e.*, a parallel magnetisation state along the positive field direction ($\uparrow\uparrow$). When the field was swept to a negative value, the magnetisation of the Py2 wires was reversed. Since the coercivities (H_c) of the Py wires were different due to their shape anisotropies, the magnetisation of the Py2 wire was flipped before that of the Py1. Accordingly the two Py wires had an antiparallel ($\downarrow\uparrow$) state. Subsequently, as the field sweep continued the Py1 magnetisation was also flipped, resulting the both Py magnetisations in the negative saturation ($\downarrow\downarrow$). This process was reversed when the sweeping field was reversed, *i.e.*, from the negative saturation to the positive saturation.

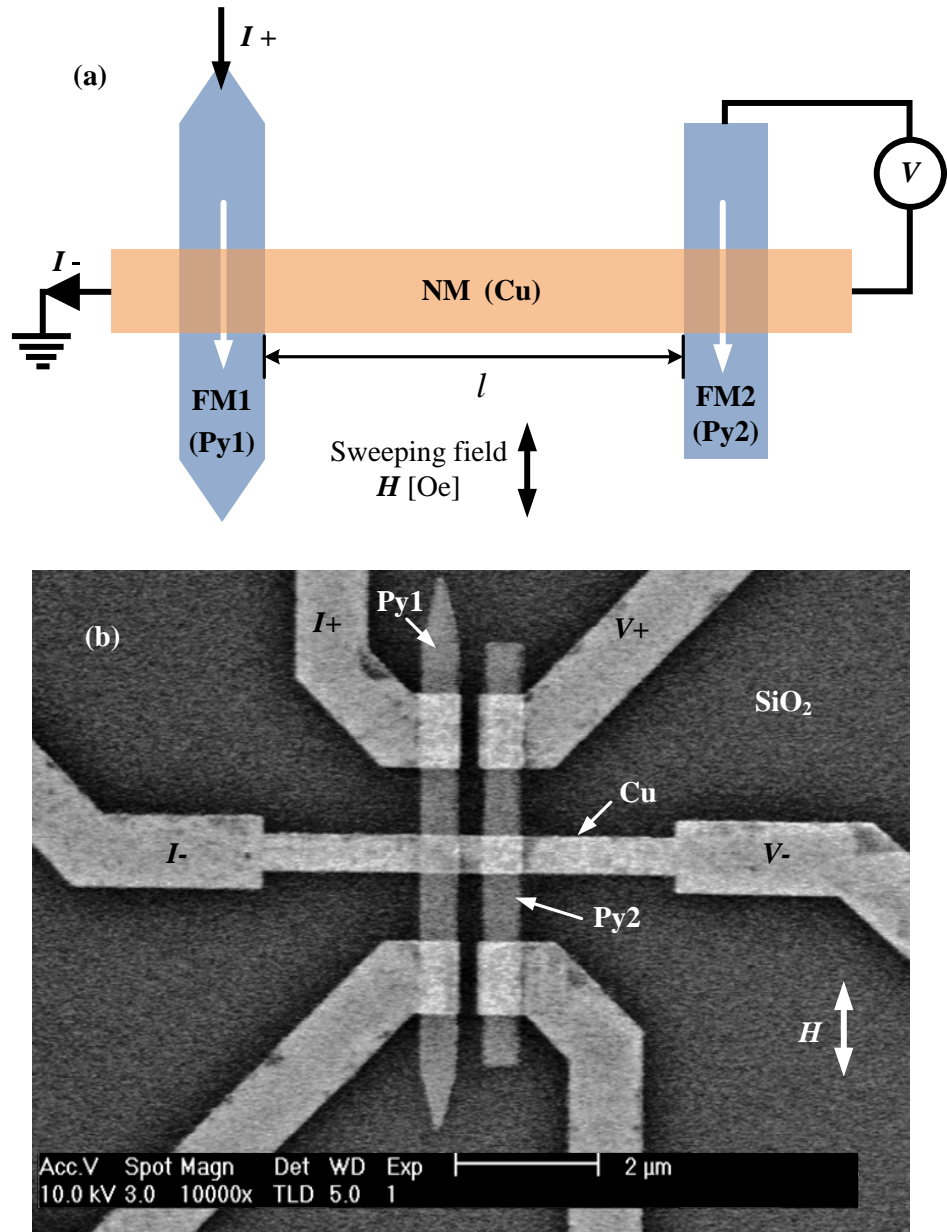


Figure 6.8: (a) Diagram of the NLSV measurement at RT used in this work. (b) SEM image with the current source and nanovoltmeter connections as well as an applied magnetic field orientation.

Figure 6.9 shows typical magnetic-field-dependent non-local voltages obtained for the three samples measured at RT. The non-local spin signals ($\Delta V/I$), which are due to resistance changes between the parallel and antiparallel states, are clearly observed. By sweeping the magnetic field from the positive saturation to the negative saturation, a decrease in the resistance is detected when the first Py2 electrode flips at H_c^{Py2} resulting in an antiparallel magnetisation state. As one can see from these graphs, the three samples exhibit apparent switching at around 125 Oe, 250 Oe and 500 Oe, corresponding to the switching fields of the Py2 wires with their width of 500 nm, 200 nm and 100 nm, respectively. This is due to the fact that the coercivity depends on the width of the ferromagnetic nanowires with the same length. For isotropic NiFe nanowires, the reduction in the shape anisotropy by increasing the width reduces the switching fields [106, 149, 150].

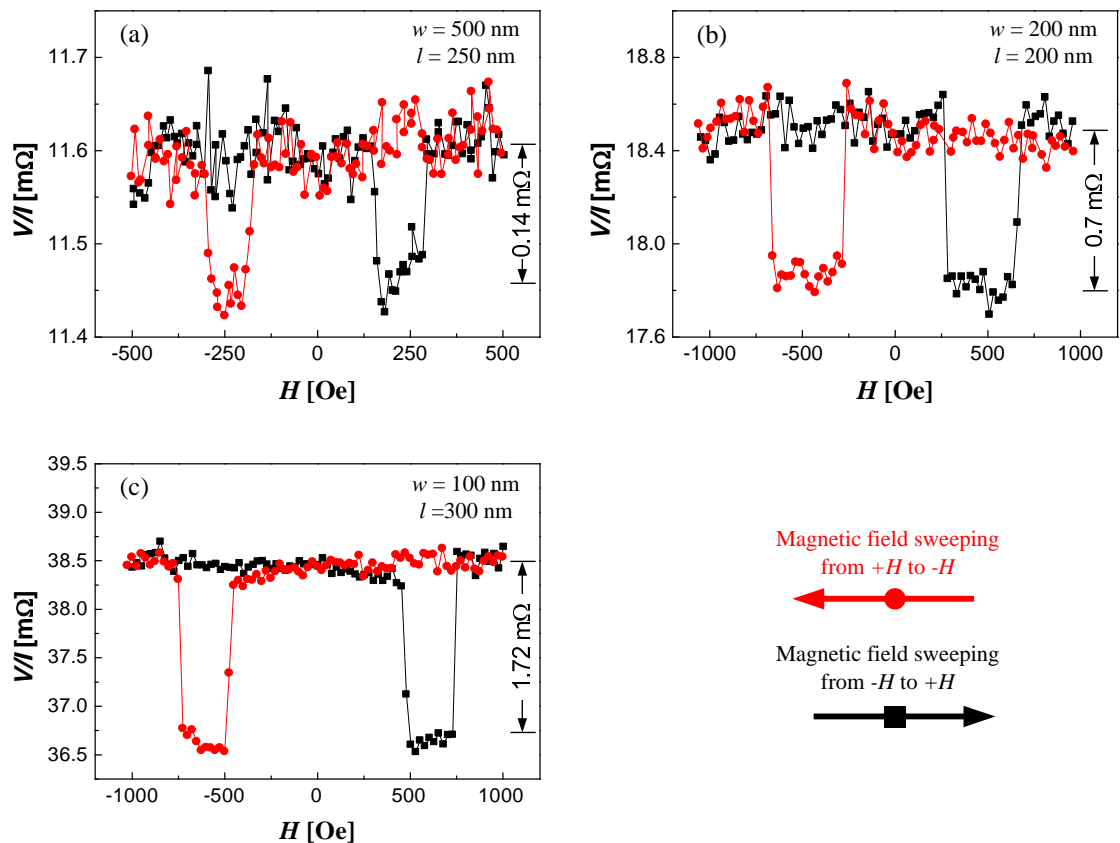


Figure 6.9: NLSV signals measured for the three devices; (a) Sample-500, (b) Sample-200 and (c) Sample-100.

In the LSV devices, it has also been well known that $\Delta V/I$ can be increased significantly by reducing the sample dimensions [66, 151, 152]. The first experimental trial of detecting a pure spin-signal was carried out by Johnson and Silsbee using the non-local geometry [63]. However the obtained signal in their measurements was very small (~ 60 pV) [65, 153]. This was due to the fact that they used microscale devices which had a dimension much larger than the critical length scale of spin transport in a metal, *i.e.*, the spin diffusion length [151]. In the following years, many researchers focused on the development of nanofabrication techniques in order to reduce the scale of their samples. In 2001, Jedema *et al.* successfully demonstrated to obtain enhanced spin signals (150 to 1500 nV, corresponding to 0.02 to 0.4 m Ω) at RT by reducing the device dimension [16]. In this study, a similar order of signals was also measured (see Fig. 6.9). In the Sample-500, $\Delta V/I$ was obtained to be 0.14 m Ω as shown in Fig. 6.9(a). The signal amplitude increased up to 0.7 m Ω and 1.72 m Ω for the Sample-200 and the Sample-100 by reducing the width of the wires and resulting Py/Cu junction areas [see Figs. 6.9(b) and (c), respectively].

6.3.2.2 Spin diffusion length

Despite the large number of reports in the recent years on the spin transport properties in the LSV structures, the reported data are not highly consistent and comparable. Table 6.1 shows a summary of the spin-transport properties, such as spin diffusion length (λ_s) and the spin injection efficiency (η), reported in different references employing FM/NM/FM LSV structures. For example, λ_s measured in the Py/Cu/Py LSVs varies almost 150% and η for the Py/Au/Py LSVs varies over 750%. One common explanation for such distributions is the irreproducibility in the fabrication and experimental environment in the nanoscale systems [154–157]. It is well known that in the presence of magnetic impurity in a non-magnetic channel, the spin-flip scattering can be significantly induced [154, 158]. In this work, this was minimised using two separated steps of

e-beam lithography and lift-off in contrary to the one-step shadow-mask evaporation method [158]. The low magnitude of the resistivity calculated in the previous section is a proof of such improvement.

Table 6.1: Comparison of spin diffusion lengths and injected spin efficiency for the FM/NM/FM lateral spin-valves previously studied.

Structure	Temperature [K]	λ_s [nm]	η [%]	References
Py/Cu/Py	293	350 ± 50	2	[16]
	300	~ 500	2–3	[81]
	293	435 ± 155	~ 1	This work
	4.2	1000 ± 200	2	[16]
Co/Cu/Co	10	200 ± 20	7	[96]
Py/Al/Py	293	600 ± 50	3	[56]
	4.2	1200 ± 200	3	[56]
Py/Ag/Py	298	132–152	12	[95]
	79	162–195	21–24	[95]
	40	564	21	[155]
Py/Au/Py	15	168	26	[94]
	10	63 ± 15	3	[96]

Nevertheless, the use of multiple-step lithography technique could lead to an increased complexity and contamination. This was also resolved by using an optimised oxygen ashing process to all the samples in order to form clean interfaces. This process was optimised by investigating the separation dependence of the non-local signals using the LSV samples with $A_J = 100 \times 100 \text{ nm}^2$ at RT. Devices with different Py separations (l) were fabricated ranging from 100 nm to 600 nm and their non-local signals were measured for each separations. The plot of $\Delta V/I$ as a function of l , revealed that the signal amplitude decays exponentially with increasing l (see Fig. 6.10) as expected [65,66].

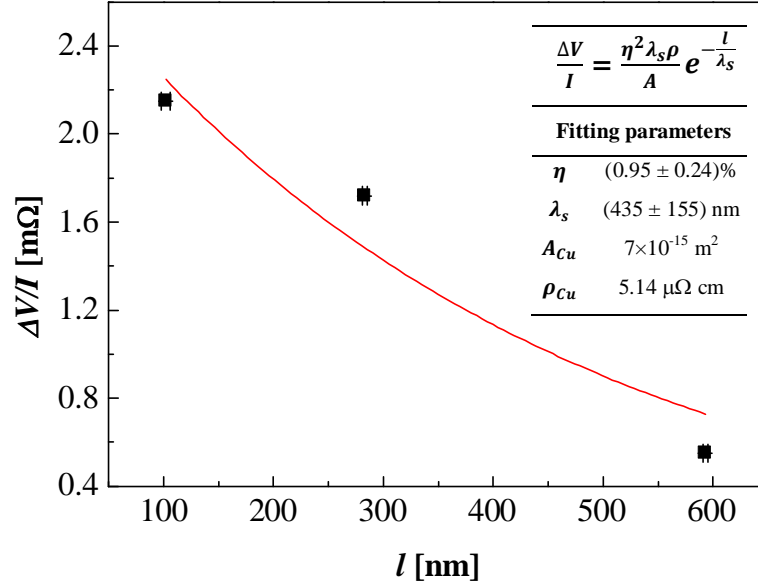


Figure 6.10: $\Delta V/I$ signals dependent on l measured using the non-local geometry for the Py/Cu/Py LSVs with junction area (A_J) of $100 \times 100 \text{ nm}^2$ at RT. The solid curve represents the best fit with Eq. 2.4.1 using the parameters shown.

By fitting these data to Eq. 2.4.1 using Origin Pro 8 software [159], the spin diffusion length (λ_s) and spin injection/detection efficiency (η) were obtained. From the best fit, λ_s and η were found to be $(435 \pm 155) \text{ nm}$ and $(0.95 \pm 0.24)\%$, respectively. However, the fitted curve contained large deviation ($\pm 155 \text{ nm}$), which was due to the small number of the data points. Initially, most of the devices were destroyed by a surge current generated in the setup during the polarity switching for the power supply of the electromagnet. This was resolved by replacing with a new bipolar power supply, which eliminated any damages to the devices during the measurements. The large deviation in the fitted curve could also be due to the lower value of the third device with $l = 600 \text{ nm}$. In this sample, the resistivity of the Cu channel was slightly higher, $(5.99 \pm 0.007) \text{ } \mu\Omega \text{ cm}$, than the others, $(4.72 \pm 1.04) \text{ } \mu\Omega \text{ cm}$. This could induce extra spin relaxation and reduce the signals at the detection electrode [142]. Nevertheless, It should still be noted that the calculated spin diffusion length for Cu ($\lambda_{Cu} \sim 435 \text{ nm}$) is comparable to that observed by Ji *et al.* [96] and Jedema *et al.* [16] as listed in Table 6.1.

Chapter 7

Non-local Spin-Current Amplification

Based on the calculations and device optimisation as described in Chapters 3, 4 and 6, LSVs with right-angle triangular shapes were fabricated for the investigation of the effect of the NM nanowire geometries upon pure spin-current signals. The geometrical effect was studied by varying the height of the triangles with the same base and measuring non-local resistance at RT. The implemented triangles were found to induce a geometrical ratchet effect (GRE) upon the pure spin current in the NM channel. The results clearly confirm that the spin-current signals were amplified significantly, by a factor of 7 as compared with the conventional LSV with the straight NM geometry. The non-local measurement configuration was also reversed to confirm the presence of the GRE. New calculations with measured sample dimensions were then performed to interpret these results, which could qualitatively explain the experimental results. The NLSV measurements were also carried out using a DC setup to investigate the origin of the GRE.

7.1 Samples and dimensions

In order to evidence the spin-current amplification by the geometrical ratchet effect (GRE), lateral spin-valve (LSV) devices were fabricated by the conventional electron-beam lithography and lift-off processes as described in details in Chapter 4. SEM images were taken on the fabricated LSV devices with a pair of right-angle triangles as shown in Fig. 7.1. The device consisted of two FM Ni₈₁Fe₁₉ (Py) nanowires bridged by a NM Cu nanowire. Both Py wires were 30 nm thick and 200 nm wide with different shapes at their ends to achieve different switching fields (see Section 6.3.2.1). These two nanowires were patterned by e-beam lithography (JEOL, JBX-6300FS) with approximately 140 nm thick resist (Zeon, ZEP520A) on a thermally oxidised Si substrate. The two Py nanowires were then deposited by e-beam evaporation at a base pressure of 5×10^{-5} Pa, followed by lift-off with cyclopentanone. The Cu nanowire was then fabricated using the same process. The thickness and width of the Cu nanowire was 70 nm and 100 nm, respectively. In Fig. 7.1, the width of the Py and Cu nanowires were measured to be (197 ± 4.5) nm and (100 ± 6.7) nm, respectively, which agreed with the above design within an error of 6.7%. Triangular wings were attached to the Cu nanowires with fixed base length of 100 nm and height (h) between 0 and 60 nm (see Table 4.1).

As shown in Chapter 6, the non-local spin signals had an inverse relationship with the FM separation and the FM/NM junction area of the LSV devices. In this chapter, the influence of the sample dimensions upon the spin signals was excluded by fixing these dimensions except the height of the triangular wings implemented at the centre of the NM nanowires. In order to confirm this exclusion, the distributions of the Py/Cu junction area (A_J) across all the devices were measured by analysing their SEM images using the same image processing tools as mentioned in Section 4.2. The dimensions were calculated by counting the pixels for 20 data points for each dimension. These values were averaged and used for the spin-current amplification analysis as listed in Table

7.1. By using these values, the junction areas were calculated by multiplying the width of the Py wire with the width of the Cu wire, confirming that all the junctions have the same area of $20.5 \times 10^{-3} \mu\text{m}^2$ with the distributions less than 7.8%. Similarly, the FM edge-to-edge distances (l) were also found to be the same as 198 nm for all the samples with the distributions less than 2.5%. These facts indicated that the influence of the sample size distributions upon the spin-current signal amplification could be negligible and the size-associated effect could be ignored. Therefore, the signal amplification measurement was expected to be only sensitive to the geometries of the triangular wings.

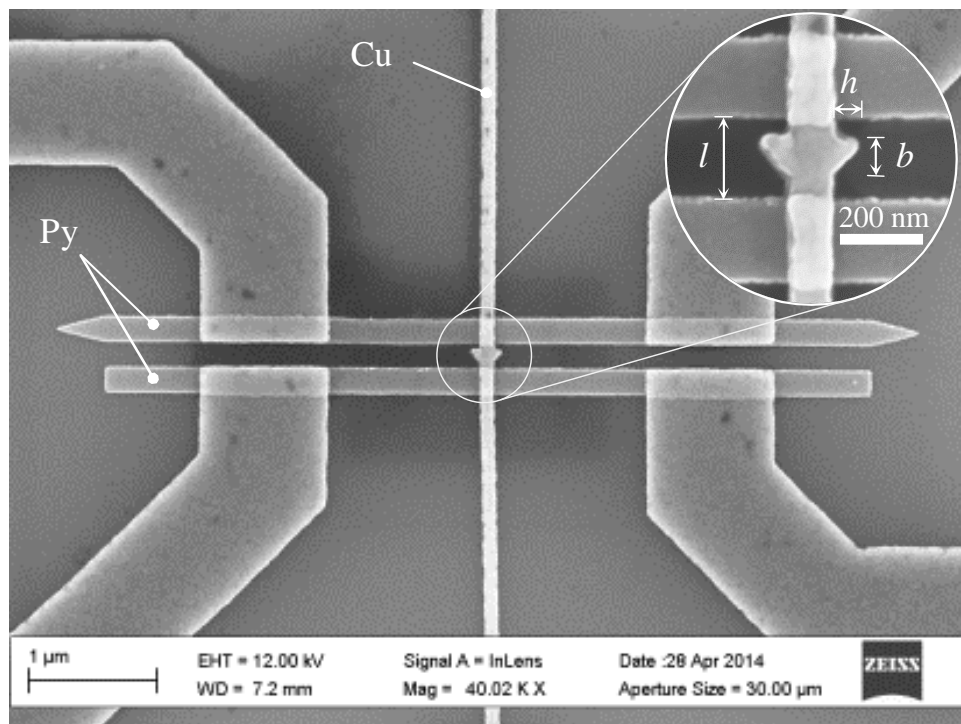


Figure 7.1: SEM image of a LSV with a pair of triangular ratchets [$h = (60 \pm 4)$ nm]. Inset shows a magnified image of the ratchet. (Courtesy of Dr. A. J. Vick).

Note all the samples used in the study of spin-current amplification, except one used in Section 7.5, were fabricated on the same wafer under the same deposition conditions to avoid any possible size and shape fluctuations from sample to sample induced by the nanofabrication processes. Hence the only difference among the LSV devices was the height (h) of the triangular wings, which was varied from 0 to 60 nm.

Table 7.1: Average values of l , w_{Py} , w_{Cu} and A_J for all the measured samples. These values were calculated by averaging 20 data points.

h [nm]	l [nm]	w_{Py} [nm]	w_{Cu} [nm]	A_J [$10^{-3} \mu\text{m}^2$]
0	(200 ± 2.8)	(200 ± 3.7)	(99 ± 6.3)	(20 ± 1.3)
20	(197 ± 4.8)	(197 ± 6.6)	(104 ± 6.7)	(21 ± 1.4)
37	(197 ± 3.1)	(202 ± 6.7)	(103 ± 7.5)	(21 ± 1.6)
60	(198 ± 3.5)	(197 ± 4.5)	(100 ± 6.7)	(20 ± 1.2)

7.2 Measurement geometries

Two different NLSV probe configurations as shown in Fig. 7.2 were used to study the spin-current amplification in the LSV devices with the right-angle triangles. One was the configuration, where an electric current (I) was injected from the Py1 into the left-hand (L) side of the Cu wire and the non-local voltage between Py2 and right-hand (R) side of the Cu wire, $V_{\text{nl}}^{\text{LtoR}}$, was measured as shown in Fig. 7.2(a). This “LtoR” configuration was the same as the NLSV measurements used for the conventional LSV devices as discussed in Section 6.3.2.1. In the second configuration, on the other hand, the positions for the spin injection and detection were reversed. The current was injected from the Py2 to the right-hand side of the Cu wire and the signal $V_{\text{nl}}^{\text{RtoL}}$ was measured between the Py1 and the left-hand side of the Cu wire as shown in Fig. 7.2(b), which was called the “RtoL” configuration. In the both geometries, the non-local configurations were maintained to introduce the pure spin current into the NM wire as described in Section 2.4. The electric current with magnitude of $45 \mu\text{A}$ was introduced to the injector using the “DC reversal” technique. The external magnetic field (H) was swept up to ± 1.0 kOe along the Py nanowires. In order to investigate the effects of the orientation of the triangular ratchets on the spin-current amplification, a direct current (DC) measurement was also carried using the same setup as presented in Section 7.5.

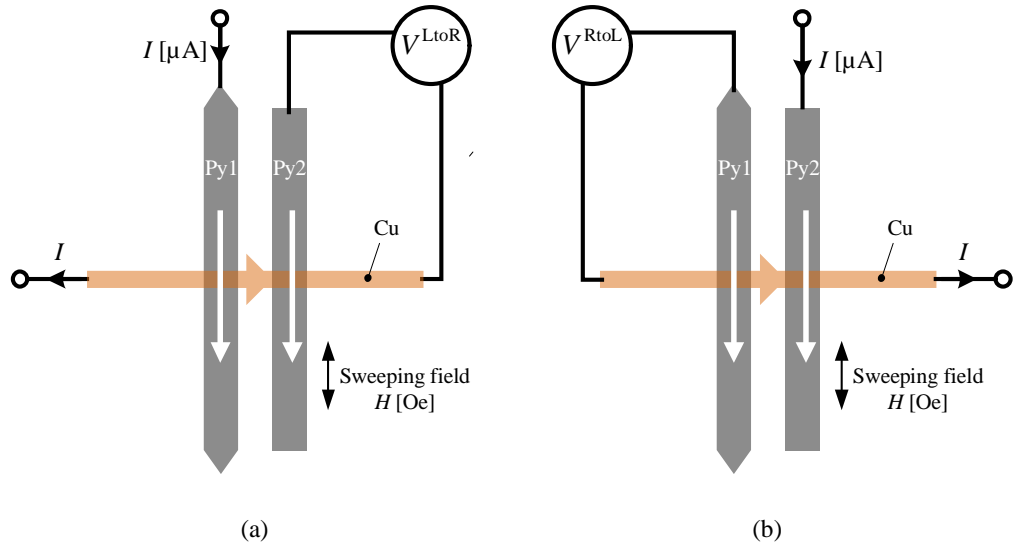


Figure 7.2: (a) “LtoR” and (b) “RtoL” probe configurations used for the non-local measurements of the LSV with ratchets. The white arrows indicate the magnetisation directions of the Py nanowires.

7.3 Spin-current amplification measurements

In this section, the above measurements have been performed on the samples listed in Table 7.1. Firstly, the NLSV measurements have been carried out with the “LtoR” probe configuration. Figure 7.3 shows the corresponding NLSV curves obtained at RT. The raw data of the NLSV signals for the LSV devices with $h = 0, 20, 37$ and 60 nm are presented in Figs. 7.3(a)-(d), respectively. Normalised non-local resistance ($R_s^{\text{LtoR}} = V^{\text{LtoR}}/I$) are plotted as a function of the sweeping magnetic field H . A clear switching behaviour of R^{LtoR} is observed for the conventional LSV with $h = 0$ as well as for the LSV with geometrical ratchets of $h = 20, 37$ and 60 nm, when the relative magnetic configurations of the Py nanowires changes from parallel (P) to antiparallel (AP) and *vice versa*. Here, the switching between the P and AP configurations have been found to occur around ± 240 and ± 680 Oe. These values are also approximately the same with the switching fields (± 250 and ± 685 Oe) of the conventional LSV device with $w_{\text{Py}} = 200$ nm (Sample-200) as discussed in Section 6.3.2.1. This confirms

that the magnetic behaviour are consistent throughout the devices.

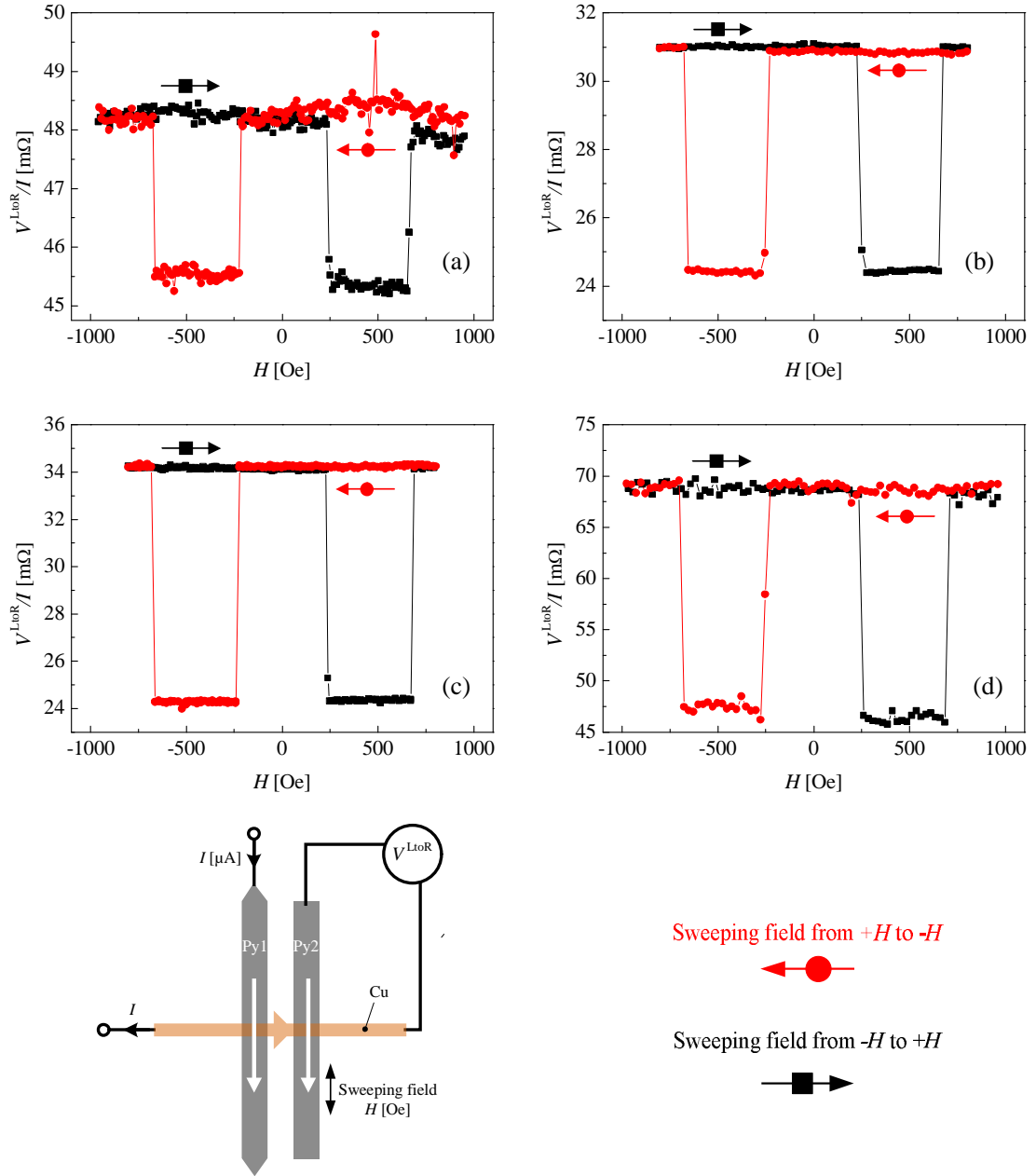


Figure 7.3: Non-local signals for the LSV with triangular ratchets of $h =$ (a) 0, (b) 20, (c) 37 and (d) 60 nm. All the measurements were carried out using the “LtoR” geometry as schematically shown.

The differences in the non-local signals, *i.e.*, $(V_P^{LtoR} - V_{AP}^{LtoR})/I = \Delta V^{LtoR}/I = \Delta R^{LtoR}$, for the P and AP configurations have been measured to be 2.81, 6.50, 9.96 and 21.5 mΩ for $h = 0, 20, 37$ and 60 nm, respectively. As it is expected

from the phenomenological explanation in Chapter 3, $\Delta V^{\text{LtoR}}/I$, which relates to the spin accumulation underneath of the Py2 detector [65,66], has been found to be amplified by a factor of 7 for the LSV with the geometrical ratchet with $h = 60$ nm in comparison with the conventional LSV with $h = 0$. This is the first experimental proof of the spin-current amplification induced by GRE [160].

The measurements have also been repeated for the same LSVs with the “RtoL” probe configuration to investigate the effects of the ratchet geometries upon the injected spin-polarised electrons in the opposite flow direction. Figure 7.4 shows the NLSV signals obtained for the LSV with $h = 20, 37$ and 60 nm with the “RtoL” configuration. Here, the signals exhibit clear spin signals with similar switching features.

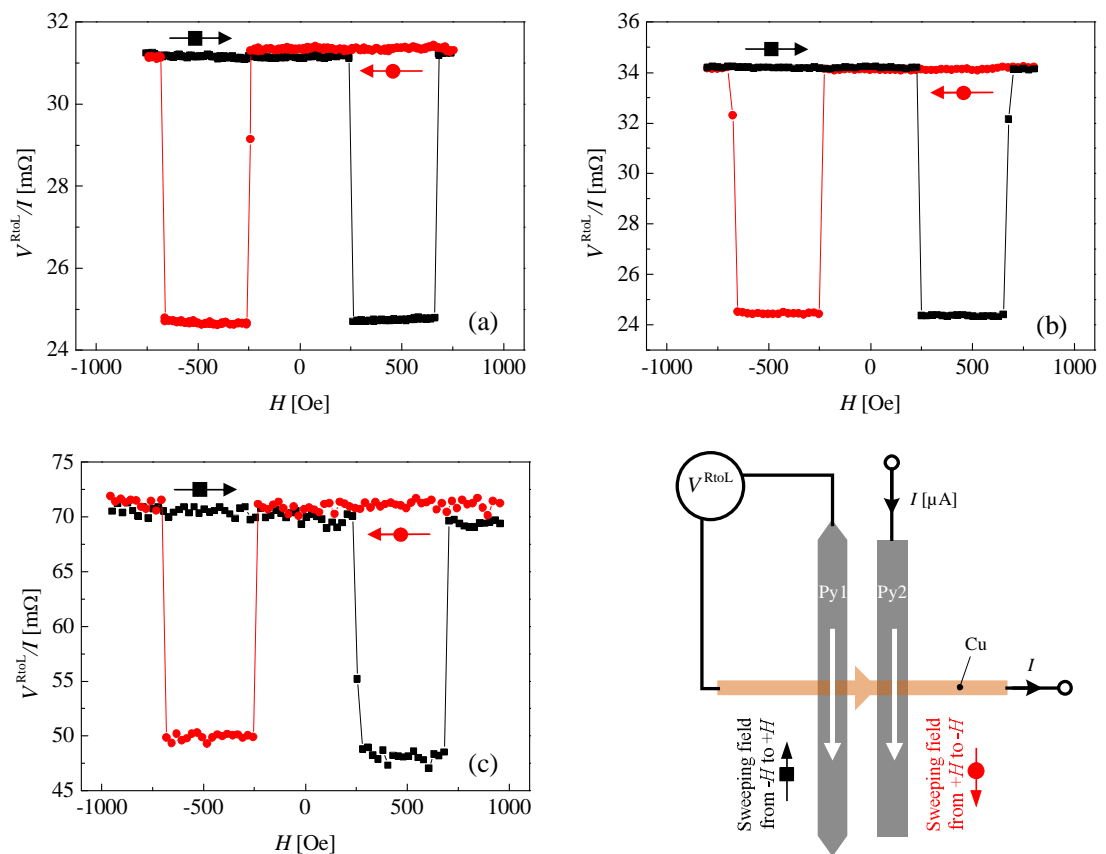


Figure 7.4: Non-local signals obtained in the “RtoL” configuration for the LSV with triangular ratchets of $h =$ (a) 20, (b) 37 and (c) 60 nm. The schematic diagram shows the measurement setup.

The corresponding $\Delta V^{\text{RtoL}}/I$ values are found to be 6.58, 9.80 and 21.7 m Ω , which are approximately the same to their $\Delta V^{\text{LtoR}}/I$ values obtained with the “LtoR” configuration measurements. This can be explained by considering the junction spin polarisation. In the numerical calculations, the processes of majority (up-spin) and minority (down-spin) diffusion, which are introduced from the opposite side of the NM nanowire, have been defined by two separated processes. For the both processes, a packet of 100% spin-polarised electrons have been introduced as a pulse. However, in the real devices, these two processes are taken place in parallel via two independent up- and down-spin channels. For example, when the majority electrons are injected from the Py1/Cu junction into the NM channel, *i.e.*, “LtoR” probe configuration, the same number of minority electrons from the right-hand side of the NM channel must be diffused back to the Py1/Cu junction to maintain the charge neutrality. However, due to the presence of the ratchet shapes, the different rate of these spin-diffusion processes form different spin-polarised currents as phenomenologically expected in Chapter 3. The GRE effect accordingly induces the spin-current amplification at Py2/Cu junction. This can be detected by the Py2.

Based on the spin-diffusion length estimation in Section 6.3.2.2, the devices studied here typically have the Py/Cu junction spin polarisation of $\sim 1\%$. This means that the spin imbalance induced at the junction is very small, *i.e.*, 50.5% up- and 49.5% down-spins. Hence, both up- and down-spin currents are introduced in parallel. This leads to the spin-current signal amplification for 50.5% up- and 49.5% down-spins with the “LtoR” configuration. Similar spin-current flows are generated for the “RtoL” configuration. Therefore, the both configurations induce a similar GRE and the resulting ΔR .

7.4 Comparison between measured and calculated values

To explain the experimental results, simple electrical transport simulations were performed using the measured device dimensions. Since the measurements were carried out with a DC current, the steady-state spin-diffusion equation (Eq. 3.7.1) in Section 3.7 was employed for the calculations. From the voltage profiles obtained from these calculations, the difference in the electron flow from left to right and *vice versa* ($\Delta V_{\text{calc}}^{\text{LtoR}}$) were calculated for each geometrical shape. These values were then compared with the non-local voltage differences measured ($\Delta V_{\text{measured}}^{\text{LtoR}}$) between the parallel and antiparallel configurations.

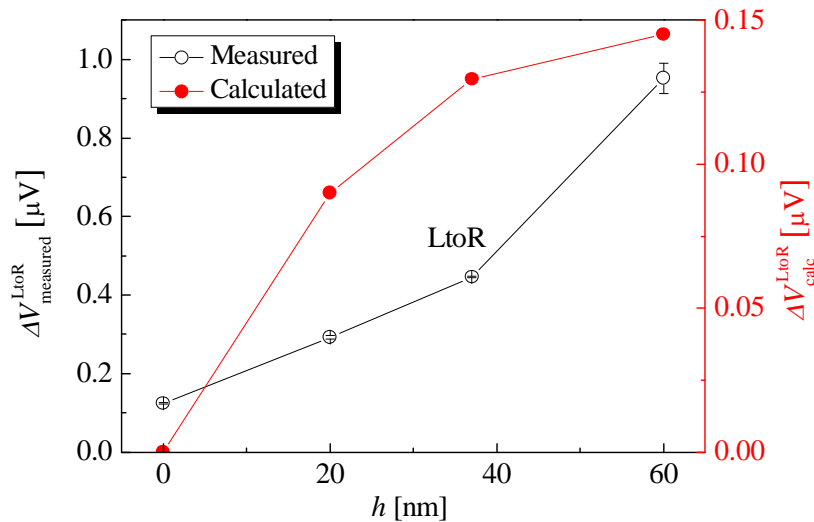


Figure 7.5: Triangular height (h) dependence of the non-local signals, both $\Delta V_{\text{measured}}^{\text{LtoR}}$ (open circles) and $\Delta V_{\text{calc}}^{\text{LtoR}}$ (closed circles).

Figure 7.5 shows the h dependence of these two voltage differences, $\Delta V_{\text{calc}}^{\text{LtoR}}$ and $\Delta V_{\text{measured}}^{\text{LtoR}}$. It is apparent that the trend of $\Delta V_{\text{measured}}^{\text{LtoR}}$ shows a good qualitative agreement with $\Delta V_{\text{calc}}^{\text{LtoR}}$. Here, the reduction of the spin polarisation by the Py electrodes and the scattering at the Py/Cu interfaces is taken into account. By implementing the Py/Cu junction spin polarisation of $\sim 1\%$ as discussed in the previous section, $\Delta V_{\text{calc}}^{\text{LtoR}}$ is calculated to be $0.15 \mu\text{V}$ at $h = 60 \text{ nm}$, which is

less than $\Delta V_{\text{measured}}^{\text{LtoR}}$ of $0.95 \mu\text{V}$ at $h = 60 \text{ nm}$ by a factor of more than 5. This discrepancy can be caused either (i) by the use of low spin injection efficiency η , which is estimated from the Sample-100, or (ii) the two-dimensional (2D) limitations in the model as mentioned in Section 3.4. Further improvement in the calculations is necessary for quantitative comparison but this proves the validity of the model to evaluate the GRE on spin-polarised electron transport.

7.5 Spin-current amplification in a conventional DC measurement

Finally, in order to study the behaviour and performance of the ratchet devices in a conventional direct current (DC) measurement, NLSV measurements with the “LtoR” and “RtoL” configurations were carried out by applying DC currents. The electric current was set to be $45 \mu\text{A}$. Another set of the LSV devices was fabricated with the same dimensions as the previous ratchet devices. It should be noted that the fabrication process was slightly different from those listed in Table 7.1. In the previous samples, prior to the Cu deposition (see Section 4.3.1.6) the surface of the Py wires were cleaned by oxygen ashing to create Ohmic and transparent Py/Cu contacts. Here, the new set of devices was fabricated without oxygen ashing.

The SEM image of the measured device is shown in Fig. 7.6. The triangular ratchet has the base of $(115 \pm 5) \text{ nm}$ and height of $(17 \pm 4) \text{ nm}$. The separation between the Py wires are measured to be $(197 \pm 2.7) \text{ nm}$. As seen in Fig. 7.6, the triangular shapes are well-defined as compared to the previous set of devices due to the improved nanofabrication processes. However, it should be noted that the base length is approximately 15 nm wider than the designed length to be 100 nm .

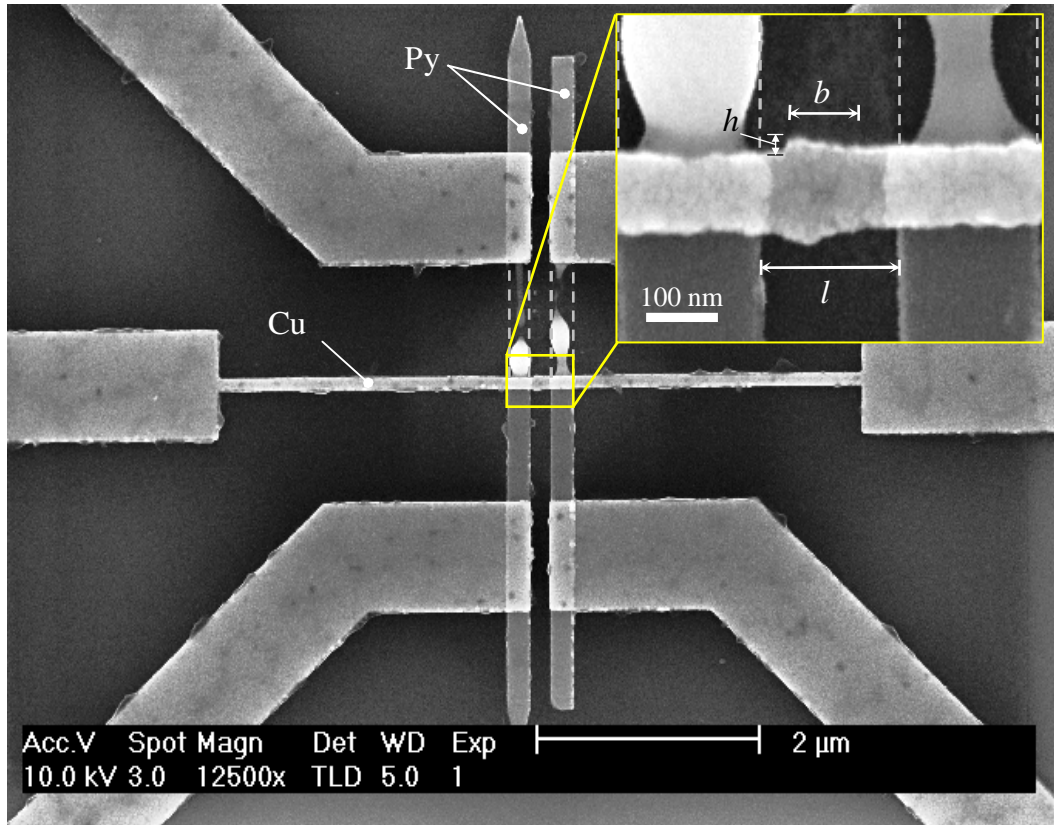


Figure 7.6: SEM image of the measured LSV with a pair of triangular ratchets [$h = (17 \pm 4)$ nm].

Using the “LtoR” and “RtoL” configurations, the NLSV measurements were repeated using the “DC reversal” technique as shown in Fig. 7.7. Here, the NLSV signals have the magnitude of $\Delta R^{\text{LtoR}} = (38.02 \pm 0.25)$ and $\Delta R^{\text{RtoL}} = (38.13 \pm 0.34)$ m Ω . These values are approximately 7 times larger than those obtained in the previous sections. This may be caused by their different spin injection efficiency η [161] at the Py/Cu junctions by removing the oxygen ashing step. In addition, the amplification factor may also be different from the previous one, owing to the fact that the implemented triangular wings have wider base length of (115 ± 5) nm (see Fig. 7.6).

Figure 7.8 shows typical results for the LSVs with $h = 20$ nm measured with the “LtoR” and “RtoL” probe configurations using the DC setup. Clear NLSV signals are observed for the both configurations. Large spin signals of $\Delta R^{\text{LtoR}} = (38.18 \pm 1.61)$ and $\Delta R^{\text{RtoL}} = (38.01 \pm 0.75)$ m Ω are obtained. These

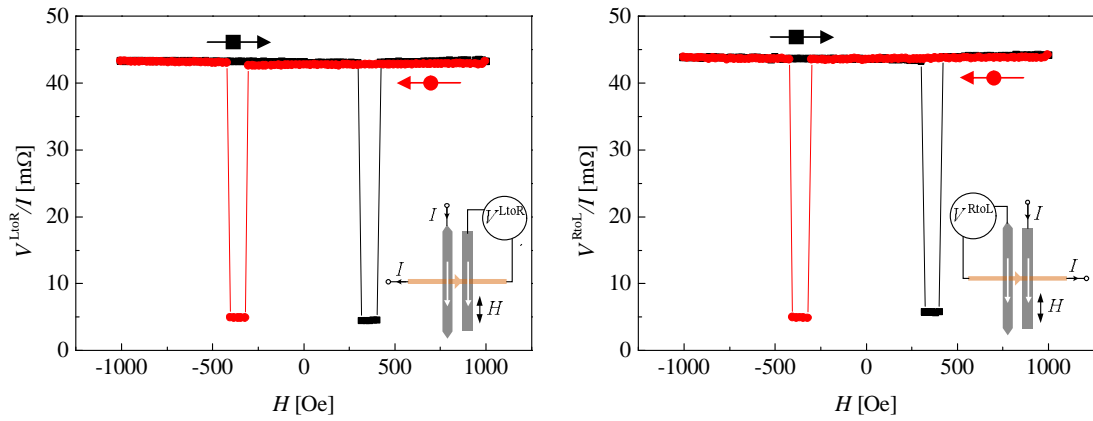


Figure 7.7: NLSV signals measured with the (a) “LtoR” and (b) “RtoL” configurations using the “DC reversal” technique. The insets show the corresponding schematic diagrams of the measurement setups.

values are almost the same with those measured by the “DC reversal” technique. This means that the spin-current amplification can also be achieved in the steady states as expected. This proves the GRE induced spin-current amplification is not associated with the current reversal by the “DC reversal” technique, which potentially induces bidirectional signals. The amplification depends on the junction spin polarisation as discussed in Section 7.3. Such steady-state spin-current amplification is very useful for future device applications.

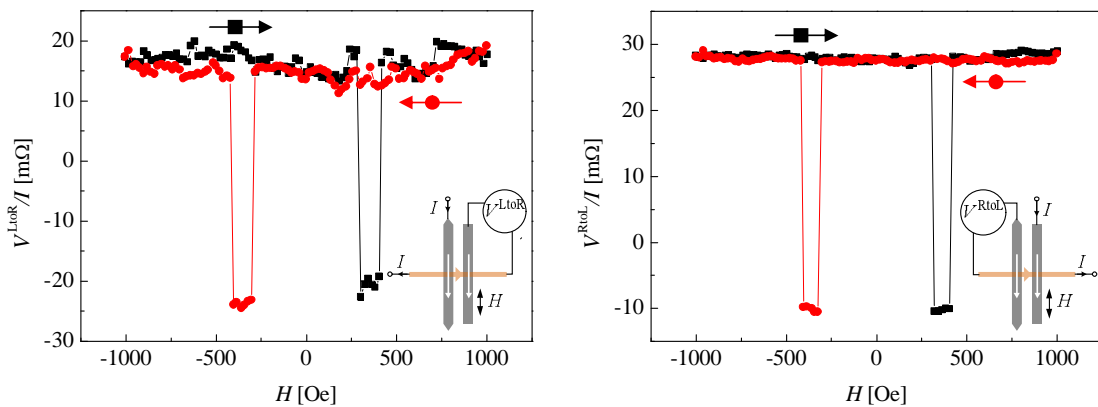


Figure 7.8: NLSV signals measured with the (a) “LtoR” and (b) “RtoL” configurations using the DC setup. The insets show the corresponding schematic diagrams of the measurement setups.

Chapter 8

Summary, Conclusions and Future Work

8.1 Summary and conclusions

Firstly, a simplified model was developed to study the realistic diffusion transport of a pure spin current in the non-local geometry as discussed in Chapter 3. Two-dimensional time-dependent simulations were carried out on a series of Cu nanowires with different shapes in order to identify geometrical effects upon spin-current diffusion and associated amplification. The middle part of the Cu channel was modified from a straight nanowire to geometries with symmetric shapes, such as squares and equilateral triangles, and asymmetric shapes, such as obtuse- and right-angle triangles. From the symmetric shapes, the majority (*e.g.*, up-spin) and minority (*e.g.*, down-spin) diffusion currents were found to have identical electrical potentials across the detection points, which led to zero amplification as expected. However, the asymmetric shapes at the middle of the NM channel induced crucial difference in the diffusive rates for the up- and down-spin electrons along the nanowire. This was induced by the scattering of the electrons at the edges of the triangular wings during their transport in the channel. This suggested that the conventional non-local geometry might

be locally broken by inducing a local spin-polarised current, which leads to the spin-current amplification. Their geometries were then optimised by changing the base length (b) and height (h) of the triangular wings in the calculations. The spin amplification was found to take its maximum for the single-pair right- and obtuse-angle triangles with $(b, h) = (300, 75)$ and $(250, 80)$ nm, respectively. The influence of the number of pairs of the triangular wings was also investigated and found to exhibit 30 – 40% decrease in the amplification in comparison to that for the single-pair triangular wings with the same h and b . Such reduction was attributed to the fact that the additional pairs of the wings increased the effective current paths for the electrons and consequently reduced the resulting spin-current signals in the NM channel. Finally, a steady-state spin-diffusion process was calculated and compared with the time-dependent cases, revealing the spin-current amplification even at a steady state.

Before experimentally validating the spin-current amplification in such geometrically modulated lateral spin-valve (LSV) devices, it was important to optimise fabrication processes as shown in Chapter 6. Two sets of preliminary devices were fabricated and their electron and spin-polarised electron transport properties were characterised. Ladder devices were first designed and characterised electrically by measuring the resistivities of the Py and Cu nanowires. The results obtained in these measurements showed that the quality of the fabricated wires was uniform and consistent with their bulk properties. Accordingly, conventional Py/Cu/Py LSV devices with straight Cu nanowires were fabricated to characterise their local and non-local transport behaviour. By sweeping a magnetic field along the Py wires, the non-local spin signals were clearly obtained at room temperature (RT). The enhancement of the spin signals due to the reduction of the device dimensions was also studied, achieving a similar order of the non-local signals with those previously reported. Finally, the spin-diffusion length was estimated for the Cu nanowire by fitting the non-local signals for a series of the LSV devices with different Py separations. The spin-diffusion length was estimated to be (435 ± 155) nm at RT, which was again comparable with those previously reported. These findings confirmed that the

fabrication procedures were optimised and could be used for the fabrication of the LSVs with the triangles.

Based on the above calculations and optimisation, the LSVs with the right-angle triangular shapes were fabricated to investigate the geometrical effects of the NM nanowire upon the pure spin-current signals. The spin-current amplification was studied at RT by changing the height of the triangles ($0 \leq h \leq 60$ nm) with maintaining the base to be 100 nm. The non-local resistance was measured in the conventional non-local geometry using the “*DC reversal*” technique. The electric current was injected from the Py1 into the left-hand side of the Cu wire, while the non-local voltage between the Py2 and the right-hand side of the Cu wire was measured. The implemented right-angle triangular wings were found to induce a geometrical ratchet effect (GRE) upon the pure spin-current in the Cu channel. The non-local resistance was measured to be significantly amplified by a factor of 7 for the LSV with the triangular pair with $h = 60$ nm as compared with the conventional LSV with $h = 0$. Similar spin-current amplification was also found for the LSVs with $h = 20$ and 37 nm but with smaller magnitude, revealing GRE was dependent upon the dimension of the Cu wire as calculated. To explain these results qualitatively, the simple electrical transport model was again employed on the devices with the measured dimensions by solving the steady-state spin-diffusion equation (Eq. 3.7.1). It was found that the trend of the calculated GRE upon the non-local signals for $0 \leq h \leq 60$ nm was in good qualitative agreement with the measured non-local signals. The non-local measurements using the both “*DC reversal*” and DC techniques were also carried out for the other set of the LSVs with the same ratchet dimensions. Large spin signals of approximately 38 m Ω were obtained for a device with $h = 20$ nm and $b = 100$ nm with both configurations introducing the electrical current on the left-hand and right-hand Py/Cu junctions. By considering the junction spin polarisation to be estimated as $\sim 1\%$, this bidirectional spin-current amplification was attributed to the parallel spin-polarised electron flow in both directions with a similar amplitude. Such GRE-induced amplification was observed for the first time in this study.

8.2 Future work

The work presented in this thesis can be further developed in the future. Based on the above results, there are several directions that subsequent researchers can build upon as detailed below:

1. Further spin-current amplification can be achieved with the other asymmetric ratchet geometries, such as obtuse-angle triangles. Additional improvement can be achieved by controlling a wider range of parameters including the base length (b), the NM wire width (w_{Cu}), the FM wire width (w_{Py}) and the number of the shape pairs (n). The amplification can also be further improved by increasing the junction spin polarisation (*e.g.*, with a half-metallic ferromagnet). These studies are expected to provide better understanding on the spin-current amplification. It is important to note that the patterning of the obtuse-angle triangles is more challenging than that of right-angle triangles to maintain the well-defined edges by controlling the correct e-beam dose during the e-beam process as mentioned in Section 4.3.1.6. It is also difficult to utilise a half-metallic ferromagnet in a LSV as the interfacial atomic disorder reduces the spin polarisation significantly [63, 162].
2. The spin-current amplification may be greater in the case of GHz-rate electrical current pulses. All the NLSV measurements in this thesis have been performed with a DC current. As compared with such steady-state measurements, high-frequency pulse measurements can detect time-dependent behaviour of spin-current distributions within an evolving time scale (~ 55 ps at RT for Cu according to the calculations in Chapter 3). Therefore, a GHz current pulse can inject a spin packet and allow to measure its time-dependent non-local signals. This may reveal insights of GRE and the associated spin-current amplification.

3. The other interesting research direction can be to investigate the effects of the other spintronic parameters, such as spin diffusion length of the NM channel and the spin injection/detection efficiency, on the spin-current amplification. The former can be examined by using a wide range of the NM materials with different spin diffusion lengths. For example, by dispersing a spin-selective scatterer (*e.g.*, Ru), the difference in the spin-polarised electron transport can be enhanced in addition to GRE as reported here. The latter can be controlled by inserting a tunnel barrier between the FM and NM layers only for the spin injector as theoretically predicted by Takahashi and Maekawa [163].

Appendix

A FreeFem++ simulation code

In this section, an example of the FreeFem++ simulation codes is shown, which was used in Chapter 3. This particular example is intended to provide an insight of the modelling processes. The example demonstrates the time-dependent spin diffusion process for the electrons flowing from left to right with right-angle triangular wings. The source code contains detailed comments within each step to explain how the simulator and model work.

Defining the variables

```
real h = 100e-9;           # The height of the triangles in meter.
real Edgeheight = h*(1e9); # The height of the triangles in nanometer.
real div = Edgeheight/100; # A geometrical ratio, which is used in the
                           # right-angle computational domain.

real T = 50e-12;          # Complete time period in second.
real dt = 0.25e-12;       # Evolution time step in second.
real W = 99e-9;           # Straight rectangular wire width in meter.
real dl = 1e-9;           # Unit length step in meter.
real uo = 0.0045;         # Introduced electron packet potential in
                           # volt.

real tsf = 11e-12;        # Spin-flip relaxation time in Cu in second.
real D = 0.012136;        # Diffusion coefficient of electrons in Cu at
                           # RT, in m2 s-1.
```

Mesh generation

```
int [int] labs = # Define the label of the computational geometry.
[11,12,13,14];
mesh Rec = square # Build the 2500 nm long straight NM channel with uniform mesh size of 1 nm.
(2500,100,[(2500e-9)*x,
-100e-9+(100e-9)*y] ,flags
= 2, label = labs);
mesh LRT0 = square # Build a square domain with uniform
(100,Edgeheight,[(100e-9)*x, mesh, which will be used in the upper
(h)*y] ,flags=2); right-angle triangle wing domain.
mesh LRB0 = square # Build a square domain with uniform
(100,Edgeheight,[(100e-9)*x, mesh, which will be used in the lower
-(100e-9+h)+(h)*y] ,flags=0); right-angle triangle wing domain.
LRT0 = trunc # Apply trunc operator on the domain
(LRT0, (x+(100*y)/Edgeheight) mesh (LRT0) to be converted to a right-
<100e-9); angle triangle shape.
LRB0= trunc # Apply trunc operator on the domain
(LRB0, (div*x-y)<(100e-9+h)); mesh (LRB0) to be converted to a right-
angle triangle wing.
mesh LRT1 = movemesh # Move the generated mesh (LRT0) by
(LRT0, [x+50e-9,y]); 50 nm away from the left edge of the NM
nanowire.
mesh LRB1 = movemesh # Move the generated mesh (LRB0) by
(LRB0, [x+50e-9,y]); 50 nm away from the left edge of the NM
nanowire.
mesh Th = Rec+LRT1+LRB1; # Glue all the geometries together.
plot(Th); # Plot the geometry with the generated
meshes.
```

Defining the finite element space

```
fespace Vh(Th,P1); # Define the finite element space (Vh) on
                    # the generated mesh (Th) with linear (P1)
                    # Lagrangian element.

Vh u=0,v,uold; # Define all parameters u, v and uold in the
               # Vh.
```

Definition of the problem in variational formulation

```
problem diffusion (u,v) # Declare the partial differential equation
= int2d(Th)(u*v/dt+ # (PDE) and the boundaries.
D*(dx(u)*dx(v)
+dy(u)*dy(v))
-int2d(Th)(uold*v/dt)
+int2d(Th)((u*v)/tsf)
+on(14,u=uo);
```

Solution and Visualisation

```
ofstream # Generating a data.csv file for extracted
ff("Data.csv",append); # data points.
for(real t = 0; t<T;t+=dt){ # For loops to evolve the solution with time
                             # step (dt).
uold=u; # Update the former solution with the new
        # solution.
diffusion; # Solve the diffusion equation by calling the
           # name of the above defined equation.
for (real l = 1e-9; l<W; # For loops to extract the solutions.
l+=dl){
ff<<u(200e-9,-l)<<" "; # Append the solutions.
ff<<endl; # An enter command.
plot(u,nbiso=200);} # Plot the solution.
```

B LabVIEW code for the “DC reversal” technique

In this work, the LabVIEW software is used for all of the data acquisition. The code for the “DC reversal” measurement shown below as an example. The code can be considered as the heart of the measurements carried out in this work. Here, the Keithley units are programmed using the standard commands for programmable instruments (SCPI) programming language via the general purpose interface bus (GPIB). The SCPI commands are given in a customised form for measuring a voltage within the range of 10 mV, where s (...) and r (...) indicate sending and receiving a code to and from the Keithley units, respectively. Next to each command, a brief description is provided to explain the corresponding function.

First the nanovoltmeter (Keithley, Model 2182A) needs to be configured as follows:

```
s(:syst:pres)           # System preset defaults.
s(:trac:cle)           # Clear readings from buffer.
s(:sens:volt:chan1:lpas # Disable the analog filter.
off;)
s(:sens:volt:chan1:dfil:stat # Enable the digital filter.
on;)
s(:sens:volt:chan1:dfil:wind # Set the digital filter window to 0.01% of
0.01;)                  the sensing voltage range.
s(:sens:volt:chan1:dfil:coun # Set the digital filter count to 15 times.
15;)
s(:sens:volt:chan1:dfil:tcon # Selecting the moving filter type.
mov;)
```

```

s(:syst:azer off;)           # Disables the autozero function to dou-
                             # ble the speed of the DC reversal measure-
                             # ments.

s(:sens:volt:rang 0.01;)    # Select the voltage range to be 10 mV.
s(:sens:volt:delt on;)     # Enable the Delta mode.
s(:sens:volt:NPLC 5;)      # Set the integration rate in line cycles
                             # (PLC) to 5, where 1 NPLC = 20 ms.

s(:sens:trig:del 0.01;)    # Trigger delay in seconds.
s(:sens:trig:sour ext;)    # Select the external TriggerLink connec-
                             # tion as input for trigger signals.

s(:trac:poin 50;)          # Set buffer size to 50 readings.
s(:trac:feed sens;)        # Store raw input readings.
s(:trac:feed:cont next;)   # Start storing readings.
s(:stat:meas:enab 512;)    # Enable buffer full (512 Decimal).
s(:*SRE 1)                 # Enable measurement summary bit MSB
                             # (Bit 0).

```

Afterward the GPIB is left to be idle for 1.5s to settle the nanovoltmeter. The source meter (Keithley, Model 2400) can then be configured as listed below.

```

s(*rst)                     # Restore GPIB defaults.
s(:trig:sourc tlin;)        # Select TriggerLink as a source of trigger
                             # input.
s(:trig:dir sour;)         # Enable bypass of the detected trigger
                             # layer event.
s(:trig:outp sour;)        # Output trigger after source operation.
s(:trig:del 0;)            # 0s trigger layer delay.
s(:syst:azer:stat off;)    # Disable the autozero function to double
                             # the speed.
s(:trig:coun 100;)         # Set the number of trigger counts to 100,
                             # which should be twice of trace points (i.e.,
                             #  $100 = 50 \times 2$ ).

```

```

s(:syst:rsen off;)           # Disable 4-wire remote sense.
s(:sour:func curr;)         # Select the current source.
s(:sour:curr:mode list;)    # Select the list mode to determine the cur-
                             # rent values.
s(:sour:list:curr          # The electric current in ampere (A).
45e-6,-45e-6;)
s(:sens:func:conc off;)     # Turn off concurrent functions.
s(:sens:func 'volt';)       # Sense a voltage which is necessary for
                             # compliance.
s(:sens:volt:nplc 0.01;)    # Measuring speed = 0.01 PLC.
s(:sens:volt:prot 0.02;)    # Select 20 mV voltage compliance, which
                             # must be equal to the sensing range. (next
                             # command)
s(:sens:volt:rang 0.02;)    # Select 20 mV voltage range.

```

Initialisation of the Source meter.

```

s(:outp on;)                # Turn on output before the measurement.
s(:init;)                   # Initialise the measurement loop.

```

The nanovoltmeter needs to be informed by a request for service (RQS) command to let the GPIB-RQS wait enough to be buffered fully and then read out the Nanovoltmeter.

```

s(:trac:data?)              # Send request for data.
R(binary data acquire)      # Receive binary data which contains calcu-
                             # lated "DC reversal" voltage values.

```

Once the measurement is completed, it can be stopped by sending the following command to the source meter.

```

s(:abort;)                  # Stop the pulse output process.
s(:outp off;)              # Turn off output.

```

Finally the nanovoltmeter can be re-initialise for a next measurement loop.

```
s(:stat:pres;)           # Return registers to default conditions.  
s(:*RST;)               # Clear registers.  
s(:Trac:clear;)        # Clear readings from the buffer.  
s(:*cls)                # Clear all event registers and error queue.
```

List of Symbols

$\uparrow (\downarrow)$	Up-(down-)spin
$\uparrow\uparrow (\uparrow\downarrow)$	Parallel (antiparallel)
A	Cross-sectional area of the non-magnetic channel
A_J	Junction area
α_{FM}	Bulk spin polarisation of the ferromagnet
b	Triangle base length
d	Thickness of the nanowire
D	Diffusion constant
$\partial\Omega$	Computational domain boundary
ΔR	Change in resistance between parallel and antiparallel states
ΔV	Change in voltage between parallel and antiparallel states
Δf	Frequency bandwidth
e	Electron charge
E_{F}	Fermi energy
f	Frequency
G	Conductance
h	Triangle height
H	Applied magnetic field
H_{c}	Coercive field
\hbar	Plank constant divided by 2π
η	Spin injection/detection efficiency
I	Electrical current
I_{noise}	Shot noise current
J	Charge current density

J_s	Pure spin current density
$J_{\uparrow(\downarrow)}$	Current density for up-(down-)spin electrons
k	Wavevector
k_B	Boltzmann constant
l	Edge-to-edge distance between the injector and detector electrodes
λ_s	Spin diffusion length
M	Net magnetic moment per unit volume
μ	Electrochemical potential
μ_B	Bohr magneton
μ_s	Non-equilibrium accumulated spins
$\mu_{\uparrow(\downarrow)}$	Electrochemical potential for up-(down-)spin electrons
n	Number of the triangular wings
$N_{\uparrow(\downarrow)}$	Density of state of the up-(down-)spin electrons
P	Spin polarisation
Q_{AB}	Seebeck coefficient of a material A with respect to B
R	Resistance
R_{AP}	Resistance for the antiparallel orientation of electrons in a spin-valve
R_{DUT}	Resistance of the device under the test
R_P	Resistance for the parallel orientation of electrons in a spin-valve
ρ	Resistivity
$S(f)$	Spectral power density
S_z	Z-component of spin angular momentum
σ	Conductivity
σ_{sd}	Standard deviation
$\sigma_{\uparrow(\downarrow)}$	Spin-dependent conductivity for up-(down-)spin electrons
t	Time
t_c	Complete time period in the time-dependent calculations
t_{th}	Wire thickness
T	Temperature
τ	Spin relaxation time
V	Electrical voltage

V_{AB}	Thermoelectric voltage induced between materials A and B
V_{AP}	Voltage for the antiparallel orientation of electrons in a spin-valve
V_{DUT}	Voltage drop in the device under the test
V_{EMF}	Thermoelectric voltage offset
V_g	Gate voltage
V_J	Johnson noise level in voltage
V_{lead}	Voltage drop in the lead wire
V_M	Voltage reading measured by the nanovoltmeter
V_{nl}	Non-local spin voltage
V_P	Voltage for the parallel orientation of electrons in a spin-valve
w	Wire strip width

List of Abbreviations

2D	Two-dimensional
AC	Alternating-current
AF	Antiferromagnet
AMR	Anisotropic magnetoresistance
AP	Antiparallel
CIP	Current in the plane
CMRR	Common mode rejection ratio
CPP	Current perpendicular to the plane
DAQ	Data acquisition
DC	Direct-current
DOS	Density of states
DRAM	Dynamic random access memory
DUT	Device under the test
EB	Electron beam
EBL	Electron-beam lithography
EMF	Electromotive force
ESD	Electrostatic discharge
fcc	Face-centred cubic
FEM	Finite element method
FE-space	Finite element space
FM	Ferromagnet
FM/I/S	Ferromagnet/insulator/superconductor structure
FM/NM	Ferromagnet/non-magnet interface
FWHM	Full width half maximum

GMR	Giant magnetoresistance
GPIO	General purpose interface bus
GRE	Geometrical ratchet effect
HDD	Hard disk drive
IC	Integrated circuit
ICT	Information communication technology
IPA	Isopropanol
I-V	Current-voltage
LSV	Lateral spin-valve
MOSFET	Metal oxide semiconductor field effect transistor
MRAM	Magnetic random access memory
MTJ	Magnetic tunnel junction
MUD	Measurement unit device
NLSV	Non-local spin-valve geometry
NM	Non-magnetic
NPGS	Nanometer pattern generation system software
NPLC	Number power line cycles
NVM	Non-volatile memory
P	Parallel
PC	Personal computer
PDE	Partial differential equation
PMMA	Polymethyl methacrylate
RAM	Random access memory
rms	Root mean square
RT	Room temperature
S/N ratio	Signal to noise ratio
SCPI	Standard commands for programmable instruments
SEM	Scanning electron microscope
SHE	Spin Hall effect
Spin FET	Spin-polarised field effect transistor
SRAM	Static random access memory

SSE	Spin Seebeck effect
STT	Spin transfer torque
TMR	Tunnelling magnetoresistance
UV	Ultraviolet

References

- [1] M. Lundstrom, *Science* **299**(5604), 210 (2003).
- [2] S. A. Wolf, D. D. Awschalom, R. A. Buhrman, J. M. Daughton, S. von Molnr, M. L. Roukes, A. Y. Chtchelkanova, and D. M. Treger, *Science* **294**, 5546 (2001).
- [3] I. Zutic, J. Fabian, and S. D. Sarma, *Rev. Mod. Phys.* **76**, 323 (2004).
- [4] I. Zutic and Evgeny Y Tsymbal, Eds., *Handbook of Spin Transport and Magnetism*, Chapman and Hall/CRC (2011).
- [5] M.I. Dyakonov and V. Perel, *Sov. Phys. JETP Lett.* **13**, 467 (1971).
- [6] J. E. Hirsch, *Phys. Rev. Lett.* **83**, 1834 (1999).
- [7] Y. A. Bychkov and E. I. Rashba, *J. Exp. Theor. Phys. Lett.* **39**, 78 (1984).
- [8] T. Kimura, Y. Otani, T. Sato, S. Takahashi, and S. Maekawa, *Phys. Rev. Lett.* **98**, 156601 (2007).
- [9] S. O. Valenzuela and M. Tinkham, *Nature* **442**(7099), 176 (2006).
- [10] T. Seki, Y. Hasegawa, S. Mitani, S. Takahashi, H. Imamura, S. Maekawa, J. Nitta, and K. Takanashi, *Nat. Mater.* **7**, 125 (2008).
- [11] E. Saitoh, M. Ueda, H. Miyajima, and G. Tatara, *Appl. Phys. Lett.* **88**(18), 182509 (2006).
- [12] O. Mosendz, J. E. Pearson, F. Y. Fradin, G. E. W. Bauer, S. D. Bader, and A. Hoffmann, *Phys. Rev. Lett.* **104**, 046601 (2010).

- [13] S. Mizukami, Y. Ando, and T. Miyazaki, *Phys. Rev. B* **66**, 104413 (2002).
- [14] H. S. S. Y. Jean-Christophe Le Breton, Sandeep Sharma and J. Ron, *Nature* **475**, 82 (2011).
- [15] K. Uchida, H. Adachi, T. An, T. Ota, M. Toda, B. Hillebrands, S. Maekawa, and E. Saitoh, *Nat. Mater.* **10**, 737 (2011).
- [16] F. J. Jedema, A. T. Filip, and B. J. van Wees, *Nature* **410**, 345 (2001).
- [17] Y. Otani and T. Kimura, *Philos. Trans. R. Soc. London Ser. A* **369**(1948), 3136 (2011).
- [18] M. Johnson and R. H. Silsbee, *Phys. Rev. Lett.* **55**, 1790 (1985).
- [19] T. Kimura, J. Hamrle, Y. Otani, K. Tsukagoshi, and Y. Aoyagi, *Appl. Phys. Lett.* **85**(16), 3501 (2004).
- [20] A. Hoffmann, J. E. Pearson, S. D. Bader, and Y. Ji, *Appl. Phys. Lett.* **88**(5), 1 (2006).
- [21] M. V. Costache, M. Zaffalon, and B. J. van Wees, *Phys. Rev. B* **74**, 012412 (2006).
- [22] S. Garzon, I. Zutic, and R. A. Webb, *Phys. Rev. Lett.* **94**, 176601 (2005).
- [23] G. Binasch, P. Grünberg, F. Saurenbach, and W. Zinn, *Phys. Rev. B* **39**, 4828 (1989).
- [24] T. Miyazaki and N. Tezuka, *J. Magn. Magn. Mater.* **139**(3), L231 (1995).
- [25] M. Karplus and R. N. Porter, *Atoms and Molecules*, The Benjamin / Cummings Publishing Company (1970).
- [26] Y. B. B. Avishai, Ed., *Quantum Mechanics with Applications to Nanotechnology and Information Science*, Academic Press, Amsterdam (2013).
- [27] N. F. Mott, *Proc. R. Soc.* **153**, 699 (1936).
- [28] A. Fert and I. Campbell, *Phys. Rev. Lett.* **21**(1190) (1968).

- [29] A. Fert and I. A. Campbell, *J. Phys. F: Met. Phys.* **6**(849) (1976).
- [30] C. Kittel, *Introduction to Solid State Physics*, Wiley; 8 edition (2005).
- [31] S. Gasiorowicz, *Quantum physics*, John Wiley & Sons, Inc. (1974).
- [32] R. A. de Groot, F. M. Mueller, P. G. van Engen, and K. H. J. Buschow, *Phys. Rev. Lett.* **50**, 2024 (1983).
- [33] P. M. Tedrow and R. Meservey, *Phys. Rep.* **283**(173) (1994).
- [34] R. J. Soulen Jr., J. M. Byers, M. S. Osofsky, B. Nadgorny, T. Ambrose, S. F. Cheng, P. R. Broussard, C. T. Tanaka, J. Nowak, J. S. Moodera, A. Barry, and J. M. D. Coey, *Science* **282**(85) (1998).
- [35] Y. Ji, G. J. Strijkers, F. Y. Yang, C. L. Chien, J. M. Byers, A. Anguelouch, G. Xiao, and A. Gupta, *Phys. Rev. Lett.* **86**, 5585 (2001).
- [36] Y. Ji, G. J. Strijkers, R. Y. Yang, and C. L. Chien, *Phys. Rev. B* **64**, 224425 (2001).
- [37] J. S. Parker, S. M. Watts, P. G. Ivanov, and P. Xiong, *Phys. Rev. Lett.* **88**, 196601 (2002).
- [38] A. W. aus Tett nang, *Magnetoresistance and magnetization dynamics in hybrid structures*. PhD thesis, Hamburg (2008).
- [39] P. M. Tedrow and R. Meservey, *Phys. Rev. Lett.* **26**(192) (1971).
- [40] P. M. Tedrow and R. Meservey, *Phys. Rev. Lett.* **27**(919) (1971).
- [41] P. M. Tedrow and R. Meservey, *Phys. Rev. B* **7**(318) (1973).
- [42] M. Julliere, *Phys. Lett. A* **54**, 225 (1975).
- [43] M. N. Baibich, J. M. Broto, A. Fert, F. N. Van Dau, F. Petroff, P. Etienne, G. Creuzet, A. Friederich, and Chazelas, J., *Phys. Rev. Lett.* **61**, 2472 (1988).
- [44] B. Dieny, V.S. Speriosu, S.S.P. Parkin, B.A. Gurney, D. R. Wilhoit, and D. Mauri, *Phys. Rev. B* **43**(1), 1297 (1991).

- [45] B. Whyte, "A brief history of areal density," *IBM DeveloperWorks*. Retrieved July 25, 2014. (2009).
- [46] C. Walter, , "Kryder's law," *Sci. Am.* (2005).
- [47] J. Bass and W. P. Pratt, *J. Magn. Magn. Mater.* **200**(1-3), 274 (1999).
- [48] A. Fert, *Rev. Mod. Phys.* **80**, 1517 (2008).
- [49] K. Likhareu in *Nanoelectronics and Photonics*, A. Korokin and F. Rosei, Eds., *Nanostructure Science and Technology*, Springer New York (2008).
- [50] P. Holody, W. C. Chiang, R. Loloee, J. Bass, W. P. Pratt, and P. A. Schroeder, *Phys. Rev. B* **58**, 12230 (1998).
- [51] M. A. M. Gijs, S. K. J. Lenczowski, and J. B. Giesbers, *Phys. Rev. Lett.* **70**, 3343 (1993).
- [52] P. C. Van Son, H. Van Kempen, and P. Wyder, *Phys. Rev. Lett.* **58**, 2271 (1987).
- [53] T. Valet and A. Fert, *Phys. Rev. B* **48**, 7099 (1993).
- [54] S. Dubois, L. Piraux, J. George, K. Ounadjela, J. Duvail, and A. Fert, *Phys. Rev. B* **60**, 477 (1999).
- [55] S. D. Steenwyk, S. Y. Hsu, R. Loloee, J. Bass, and W. P. Pratt Jr., *J. Mag. Magn. Mater.* **170**(L1) (1997).
- [56] F. J. Jedema, M. S. Nijboer, A. T. Filip, and B. J. van Wees, *Phys. Rev. B* **67** (2003).
- [57] S. Datta, *Electronic Transport in Mesoscopic Systems*, Cambridge University Press, new ed edition ed. (1997).
- [58] J. Fabian, A. Matos-Abiague, C. Ertler, P. Stano, and I. Zutic, *Acta Phys. Slov.* **57**, 565 (2007).
- [59] F. J. Jedema, *Electrical Spin Injection in metallic Mesoscopic Spin Valves*. PhD thesis, Rijksuniversiteit Groningen (2002).

- [60] R. H. Silsbee, *Bull. Magn. Reson.* **2**, 284 (1980).
- [61] G. Schmidt, D. Ferrand, L. W. Molenkamp, A. T. Filip, and B. J. van Wees, *Phys. Rev. B* **62**, R4790 (2000).
- [62] T. R. McGuire and R. I. Potter, *IEEE Trans. Magn.* **11**(4), 1018 (1975).
- [63] A. Hirohata and K. Takanashi, *J. Phys. D: Appl. Phys.* **47**(19), 193001 (2014).
- [64] V. Korenivski, N. Poli, D. B. Haviland, and M. Urech, *Nano Lett.* **6**(4), 871 (2006).
- [65] M. Johnson, *Phys. Rev. Lett.* **70**(14), 2142 (1993).
- [66] F. J. Jedema, H. B. Heersche, A. T. Filip, J. J. A. Baselmans, and B. J. van Wees, *Nature* **416**, 713 (2002).
- [67] S. Bandyopadhyay, *Introduction to spintronics*, CRC Press, 1st ed. (2008).
- [68] P. T. Wenk, *Itinerant Spin Dynamics in Structures of Reduced Dimensionality*. PhD thesis, Jacobs University Bremen (2011).
- [69] N. W. Ashcroft and N. D. Mermin, *Solid State Physics*, Cengage Learning Services (1976).
- [70] T. Micklitz, A. Altland, T. A. Costi, and A. Rosch, *Phys. Rev. Lett.* **96**(22), 226601 (2006).
- [71] E. Muller-Hartmann and J. Zittartz, *Phys. Rev. Lett.* **26**(8), 428 (1971).
- [72] J.-G. J. Zhu and C. Park, *Mater. Today* **9**, 36 (2006).
- [73] K. Inomata, "Magnetoresistive random access memories (mrams)," <http://www.nims.go.jp/mmu/tutorials/MRAM.html> (2015).
- [74] Y. Iba, A. Takahashi, A. Hatada, M. Nakabayashi, C. Yoshida, Y. Yamazaki, K. Tsunoda, and T. Sugii, "A highly scalable stt-mram fabricated by a novel technique for shrinking a magnetic tunnel junction with reducing processing damage," in *VLSI Technology (VLSI-Technology): Digest of Technical Papers, 2014 Symposium on*, 1–2, IEEE, (Honolulu, HI) (2014).

- [75] S. Datta and B. Das, *Appl. Phys. Lett.* **56**(7), 665 (1990).
- [76] B. Wang, J. Wang, and H. Guo, *Phys. Rev. B* **67** (2003).
- [77] Z. Guo and L. Tan, *Fundamentals and Applications of Nanomaterials*, Artech House, 1st ed. (2009).
- [78] S. Maekawa, E. Saitoh, S. O. Valenzuela and T. Kimura, Eds., *Spin current (Series on Semiconductor Science and Technology)*, Oxford University Press (2012).
- [79] M. Johnson, *Science* **260**(320) (1993).
- [80] A. Brataas, Y. Tserkovnyak, G. Bauer, and B. Halperin, *Phys. Rev. B* **66**, 060404 (2002).
- [81] T. Kimura, J. Hamrle, and Y. Otani, *Phys. Rev. B* **72**, 014461 (2005).
- [82] Y. K. Takahashi, S. Kasai, S. Hirayama, S. Mitani, and K. Hono, *Appl. Phys. Lett.* **100**, 5 (2012).
- [83] M. Johnson, *IEEE Trans Electron Devs* **54**, 1024 (2007).
- [84] F. Hecht, *J. Numer. Math.* **20**, 251 (2012).
- [85] Y.-T. C. Jichun Li, *Computational Partial Differential Equations Using MATLAB*, Chapman and Hall/CRC (2008).
- [86] P. George, *Automatic triangulation*, Wiley (1996).
- [87] S. Rao, *The Finite Element Method in Engineering*, Butterworth-Heinemann, 4th ed. (2005).
- [88] Z.-F. L. Yu-Qiu Long, Song Cen, *Advanced Finite Element Method in Structural Engineering*, Springer (2009).
- [89] G. Liu and S. Quek, *Finite Element Method*, Butterworth-Heinemann (2003).

- [90] O. Zienkiewicz, R. Taylor, and J. Zhu, *The Finite Element Method: its Basis and Fundamentals*, Butterworth-Heinemann, 7th ed. (2013).
- [91] Y.-H. Zhu, B. Hillebrands, and H. Schneider, *Phys. Rev. B* **78**, 054429 (2008).
- [92] S. Kaltenborn, Y.-H. Zhu, and H. C. Schneider, *Phys. Rev. B* **85**, 235101 (2012).
- [93] JEOL, “Jbx-6300fs electron beam lithography manual, <http://www.jeol.co.jp/en/>,”
- [94] J.-H. Ku, J. Chang, H. Kim, and J. Eom, *Appl. Phys. Lett.* **88**, 172510 (2006).
- [95] R. Godfrey and M. Johnson, *Phys. Rev. Lett.* **96**, 136601 (2006).
- [96] Y. Ji, A. Hoffmann, J. S. Jiang, J. E. Pearson, and S. D. Bader, *J. Phys. D: Appl. Phys.* **40**(5), 1280 (2007).
- [97] G. Mihajlovic, J. E. Pearson, S. D. Bader, and A. Hoffmann, *Phys. Rev. Lett.* **104**, 237202 (2010).
- [98] E. I. Rashba, *Phys. Rev. B* **62**, R16267 (2000).
- [99] *EVG 610 Semi-automated Mask Aligner manual*, <http://www.evgroup.com>.
- [100] D. M. Kim and Y.-H. Jeong, Eds., *Nanowire Field Effect Transistors: Principles and Applications*, Springer New York (2013).
- [101] Microsoft office Visio 2007, <http://office.microsoft.com/en-gb/visio/>
- [102] G. S. May and S. M. Sze, *Fundamentals of Semiconductor Fabrication*, John Wiley and Sons Ltd (2004).
- [103] S. C. Andrea Gusman and D. Yaghmaie, “Zep520a - new resist for electron beam lithography,” tech. rep., Available at: <http://research.engineering.ucdavis.edu/cnm2/wp-content/uploads/sites/11/2013/05/ZEP520A-Process.pdf> (2011).

- [104] J. D. Plummer, M. D. Deal, and P. B. Griffin, *Silicon Vlsi Technology Fundamentals Practice and Modeling*, no. 238, Prentice Hall (2000).
- [105] JBX-6300FS, University of Leeds, "<http://www.engineering.leeds.ac.uk/>,"
- [106] T. Schrefl, J. Fidler, K. J. Kirk, and J. N. Chapman, *J. Magn. Magn. Mater.* **175**, 193 (1997).
- [107] T. Kimura and Y. Otani, *Phys. Rev. Lett.* **99**, 196604 (2007).
- [108] S. M. S. C.Y. Chang, *ULSI Technology*, no. pp305-307, McGraw-Hill Education (Ise Editions) (1996).
- [109] I. Tanner Research, "L-edit, <http://www.tanner.com/>," (2014).
- [110] G. Harman and J. Albers, *IEEE Trans. Parts Hyb. Pac.* (1977).
- [111] M. R. Haskard, *Electronic Circuit Cards and Surface Mount Technology: A Guide to Their Design, Assembly, and Application*, Prentice Hall- Gale, 1st ed. (1992).
- [112] D. A. Doane and P. Franzone, *Multichip Module Technologies and Alternatives: The basics*, New York : Van Nostrand Reinhold (1993).
- [113] National Instruments, <http://www.ni.com/labview/>
- [114] *Low Level Measurements Handbook: Precision DC Current, Voltage, and Resistance Measurements.*, KEITHLEY Instruments, 6th edition ed. (2004).
- [115] *Nanotechnology Measurement Handbook: A Guide to Electrical Measurements for Nanoscience Applications.*, KEITHLEY Instruments, 1st edition ed. (2007).
- [116] J. B. Johnson, *Nature* **119**, 50 (1927).
- [117] J. B. Johnson, *Phys. Rev.* **32**, 97 (1928).
- [118] H. Nyquist, *Phys. Rev.* **32**, 110 (1928).

- [119] J. Makupson, "Achieving accurate and reliable low level electrical measurements," in *Instrumentation and Measurement Technology Conference, 2006. IMTC 2006. Proceedings of the IEEE, IX-IX* (2006).
- [120] R. Jenkins, "All the noise in resistors," *Hartman Technica Retrieved*, <http://www.hartmantech.com> (2014).
- [121] K.-L. Du and M. N. S. Swamy, *Wireless Communication Systems: From RF Subsystems to 4G Enabling Technologies*, Cambridge University Press (2010).
- [122] P. Horowitz and W. Hill, *The Art of Electronics*, Cambridge University Press, 2nd ed. (1989).
- [123] Y. Blanter and M. Buttiker, *Phys. Rep.* **336**, 1 (2000).
- [124] R. L. Dragomirova, L. P. Zarbo, and B. K. Nikolic, *Europhys. Lett.* **84**(3), 37004 (2008).
- [125] R. D. Barnard, *Thermoelectricity in Metals and Alloys*, Taylor and Francis Ltd (1972).
- [126] D. Cigoy, "Accurate low-resistance measurements start with identifying sources of error," *Keithley Instruments, Inc.* (2010).
- [127] *For the connections and the pin-layouts refer to the manual of 2182/2182A nanovoltmeter provided by Keithley Instruments, Inc.*
- [128] Keithley, *Model 2182/2182A Nanovoltmeter User's Manual*, Keithley Instruments, Inc. (2004).
- [129] A. Daire, "Low-voltage measurement techniques," *Keithley Instruments, Inc.* (2005).
- [130] J. Schweitzer, PURDUE UNIVERSITY, <http://www.purdue.edu/ehps/rem/rs/sem.htm> (2014).
- [131] NCMN Electron Microscopy, "Specimen Interaction, <http://ncmn.unl.edu/cfem/microscopy/interact.shtml>," (2015).

- [132] J. G. Charles E. Lyman, Dale E. Newbury, *Scanning Electron Microscopy, X-Ray Microanalysis, and Analytical Electron Microscopy: A Laboratory Workbook* ., Springer (1990).
- [133] D. L. Smith, *Thin-Film Deposition: Principles and Practice*, McGraw-Hill Professional (1995).
- [134] R. C. Dynes and J. P. Garno, *Phys. Rev. Lett.* **46**, 137 (1981).
- [135] J. Bass and William P Pratt Jr, *J. Phys. Condens. Matter* **19**(18), 183201 (2007).
- [136] D. Giancoli, "25. Electric Currents and Resistance". In Jocelyn Phillips. *Physics for Scientists and Engineers with Modern Physics.*, no. p. 658., Upper Saddle River, New Jersey: Prentice Hall., 4 ed. (2009 [1984]).
- [137] A. Bid, A. Bora, and A. K. Raychaudhuri, *Phys. Rev. B* **74**, 035426 (2006).
- [138] S. Maitrejean, R. Gers, T. Mourier, A. Toffoli, and G. Passemard, *Microelectron. Eng.* **83**, 2396 (2006).
- [139] W. Steinhogel, G. Schindler, G. Steinlesberger, and M. Engelhardt, *Phys. Rev. B* (2002).
- [140] G. Schindler, G. Steinlesberger, M. Engelhardt, and W. Steinhogel, *Solid-State Electron.* **47**, 1233 (2003).
- [141] W. Steinhogel, G. Schindler, G. Steinlesberger, M. Traving and M. Engelhardt, "Scaling laws for the resistivity increase of sub 100 nm interconnects," in *Simulation of Semiconductor Processes and Devices, 27–30, SISPAD 2003 International Conference* (2003).
- [142] E. Villamor, M. Isasa, L. Hueso, and F. Casanova, *Phys. Rev. B* **87**, 094417 (2013).
- [143] T. Kimura and Y. Otani, *J. Phys. Condens. Matter* **19**(16), 165216 (2007).
- [144] Y. Niimi, D. Wei, H. Idzuchi, T. Wakamura, T. Kato, and Y. Otani, *Phys. Rev. Lett.* **110**, 016805 (2013).

- [145] T. Kimura, T. Sato, and Y. Otani, *Phys. Rev. Lett.* **100**, 066602 (2008).
- [146] T. Kimura, J. Hamrle, and Y. Otani, *IEEE Trans. Magn.* **41**(2600) (2005).
- [147] D. Ilgaz, J. Nievendick, L. Heyne, D. Backes, J. Rhensius, T. Moore, M. Niño, A. Locatelli, T. Mentese, A. v. Schmidfeld, A. v. Bieren, S. Krzyk, L. Heyderman, and M. Kläui, *Phys. Rev. Lett.* **105**, 076601 (2010).
- [148] E. Villamor, M. Isasa, L. Hueso, and F. Casanova, *Phys. Rev. B* **88**, 184411 (2013).
- [149] J. Nitta, T. Schpers, H. B. Heersche, T. Koga, Y. Sato, and H. Takayanagi, *Jap. J. Appl. Phys.* **41**(2497) (2002).
- [150] A. O. Adeyeye, J. A. C. Bland, C. Daboo, Jaeyong Lee, U. Ebels, and H. Ahmed, *J. Appl. Phys.* **79**, 6120 (1996).
- [151] T. Kimura, Y. Otani, and J. Hamrle, *Phys. Rev. B* **73**, 132405 (2006).
- [152] M. Zaffalon and B. van Wees, *Phys. Rev. Lett.* **91**, 186601 (2003).
- [153] M. Johnson, *J. Appl. Phys.* **75**(10), 6714 (1994).
- [154] M. Erekhinsky, A. Sharoni, F. Casanova, and I. K. Schuller, *Appl. Phys. Lett.* **96**(2) (2010).
- [155] G. Mihajlovic, J. E. Pearson, S. D. Bader, and A. Hoffmann, *Phys. Rev. Lett.* **104**, 237202 (2010).
- [156] Piotrlaczkowski, L. Vila, S. Ferry, A. Marty, J.-M. George, H. Jaffres, A. Fert, T. Kimura, T. Yang, Y. Otani, and J.-P. Attane, *Appl. Phys. Express* **4**(6), 063007 (2011).
- [157] H. Zou, X. J. Wang, and Y. Ji, *J. Vac. Sci. Technol. B* **28**(1314) (2010).
- [158] H. Zou and Y. Ji, *Appl. Phys. Lett.* **101**, 8 (2012).
- [159] Origin, "Origin pro 8," *OriginLab Corporation* (2007).

- [160] R. M. Abdullah, A. J. Vick, B. A. Murphy, and A. Hirohata, *J. Phys. D: Appl. Phys.* **47**(48), 482001 (2014).
- [161] G. Bridoux, M. V. Costache, J. Van de Vondel, I. Neumann, and S. O. Valenzuela, *Appl. Phys. Lett.* **99**(10), – (2011).
- [162] K. Hamaya, N. Hashimoto, S. Oki, S. Yamada, M. Miyao, and K. Kimura, *Phys. Rev. B* **85**, 100404 (2012).
- [163] S. Takahashi and S. Maekawa, *Phys. Rev. B* **67**, 052409 (2003).